5-2015

Electrokinetic Flow in a Nanochannel with an Overlapped Electrical Double Layer

Zhuorui Song
Utah State University

1-1-2015

Electrokinetic flow in a Nanochannel with an Overlapped Electrical Double Layer

Zhuorui Song

ELECTROKINETIC FLOW IN A NANOCHANNEL

WITH AN OVERLAPPED ELECTRICAL DOUBLE LAYER

by

Zhuorui Song

A dissertation submitted in partial fulfillment
of the requirements for the degree

of

DOCTOR OF PHILOSOPHY

in

Mechanical Engineering

Approved:

Dr. Heng Ban Major Professor	Dr. Steve L. Folkman Committee Member
Dr. Barton Smith Committee Member	Dr. David W. Britt Committee Member
Dr. Robert E. Spall Committee Member	Dr. Mark R. McLellan Vice President for Research and Dean of the School of Graduate Studies

UTAH STATE UNIVERSITY
Logan, Utah

2015

ABSTRACT

Electrokinetic Flow in a Nanochannel

with an Overlapped Electrical Double Layer

by

Zhuorui Song, Doctor of Philosophy

Utah State University, 2015

Major Professor: Dr. Heng Ban
Department: Mechanical and Aerospace Engineering

Electrokinetic flows within an overlapped Electrical Double Layer (EDL), which are not well-understood, were theoretically investigated in this study with the particular attention on the consideration of hydronium ions in the EDL. Theoretical models for fully-developed steady pressure-driven flow for salt-free water or a binary salt solution in a slit-like nanochannel connecting to two reservoirs were developed. The transient flow in such a domain was also simulated from static state to the final steady state. In these models, the Poisson equation and the Nernst-Planck equation were solved either by analytic methods or by the finite element method. Surface adsorption-desorption equilibrium and water equilibrium were considered to account for the proton exchange at the surface and in the fluid. These models were the first to include those comprehensive processes that are uniquely important for overlapped EDL scenarios.

This study improves the understanding of electrokinetic flows within an overlapped EDL by demonstrating the profound impact of hydronium ions on the EDL structure. In the

steady flow of potassium chloride solutions, hydronium ions are more enriched than potassium ions by up to 2~3 orders of magnitude, making the electrokinetic effects greatly depressed. The unequal enrichment effects of counterions were omitted in the traditional theory partially because the transient is extremely slow. The simulation results show that a concentration hump of hydronium ions initially forming at the channel entrance gradually expands over the whole channel in a way similar to the concentration plug flow moving downstream. The time required for the flow to reach the steady state could be as long as thousands of times the hydraulic retention time, dependent on the degree of the EDL overlap. This study improves the fundamental understanding for nanofluidic flows.

(163 pages)

PUBLIC ABSTRACT

Electrokinetic Flow in a Nanochannel

with an Overlapped Electrical Double Layer

by

Zhuorui Song, Doctor of Philosophy

Utah State University, 2015

Major Professor: Dr. Heng Ban
Department: Mechanical and Aerospace Engineering

This research is a theoretical study aiming to improve the understanding of nanofluidic flows. Nanofluidic flows have a wide range of potential application in many fields, such as DNA analysis, drug delivery, analyte separation, power generation, and so on. The most common material used in nanofluidic flows is silica whose surfaces are charged mainly due to proton exchange with the fluids. Charges on the surfaces as well as near the surfaces in the fluid side cause a significantly different response of the fluids to the applied electric field or pressure difference compared to those at normal scale. In the previous studies, surface charges were usually assumed to be constant without further proton exchange, or the fluids were motionless. This study theoretically investigated the flow through a nanochannel with the consideration of dynamic proton exchange. The results show that dynamic proton exchange has significant but slow influence on nanofluidics flows. This study improves the fundamental understanding for nanofluidic flows.

Zhuorui Song

DEDICATION

I dedicate this dissertation to my parents, my wife and my extended families, who have given me the foundation and provided the strength that I have needed to accomplish this work.

ACKNOWLEDGMENTS

I would like to express sincere appreciation to my major professor, Dr. Heng Ban, for his guidance, kindness and great patience during the course of this study. I would also like to thank my other committee members, Dr. Barton Smith, Dr. Robert E. Spall, Dr. Steve L. Folkmann, Dr. David W. Britt and Dr. Byard Wood, for their assistance and advice to fulfill this dissertation.

CONTENTS

Page

LIST OF TABLES

LIST OF FIGURES

LIST OF SYMBOLS

English symbols

c	concentration (M)
e	elementary charge (=1.602×10^{-19} C)
j	flux density (mol s^{-1})
n	argument in Jacobian elliptic function, normal direction
m	parameter of Jacobian elliptic function
p	pressure (Pa)
pH	pH value
pH_z	pH value at the point of zero charge
pK	logarithmic equilibrium constants
t	time (s)
t_s	time required for reaching steady state (s)
u	bulk velocity along the channel surface (m s^{-1})
u_p, u_e, u_m	bulk velocity components (m s^{-1})
u	bulk flow velocity (m s^{-1})
x,y	x,y axes in a Cartesian coordinate system
z	ion valence
A_v	Avogadro's number (=6.022×10^{23} mol^{-1})
C	phenomenological capacity (F m^{-2})
D	diffusion coefficient (m^2 s^{-1})
Ex	streaming potential intensity (V m^{-1})

F	Faraday's number (=96485.34 C mol^{-1}l)
G	generation rate per unit volume (mol m^{-3} s^{-1})
G_{str}	streaming conductance (A Pa^{-1})
G_{elec}	electrical conductance (S)
H	channel's half width (m)
HRT	hydraulic retention time (s)
I	ionic current density (A m^{-2})
J	ionic flux through a channel (mol s^{-1})
K	dissociation equilibrium constant
L	total channel's length (m)
M	ionic flux through a reservoir (mol s^{-1})
N	outward flux density (mol m^{-2} s^{-1})
P_x	pressure gradient (Pa m^{-1})
P_{x0}	pressure gradient without EDL (Pa m^{-1})
Q	volumetric flow rate (m^3/s)
R	universal gas constant (8.314 J mol^{-1} K^{-1})
Re	Reynolds number
Sc	Schmidt number
T	temperature (K)
U	Average velocity across the channel or characteristic velocity (m s^{-1})
W	total channel's width (m)
$\langle \ \rangle$	average quantity in the cross section
$\bar{}$	dimensionless quantities

Greek symbols

$\alpha, \beta, \gamma, \delta$	dimensionless factors
ε	relative permittivity
ε_0	permittivity of free space (= 8.85×10^{-12} C/Vm)
ζ	Zeta potential or the electrical potential at the shear plane (V)
κ	Debye parameter (m^{-1})
κ_{eff}	effective Debye parameter (m^{-1})
μ	dynamic viscosity (Pa·s)
ξ	the ratio of half height to length
ρ	density (Kg/m^3)
ρ_e	spatial charge density (C/m^3)
σ	charge density (C/m^2)
φ	electrical potential perpendicular to surfaces (V)
φ_{chm}	equivalent electrical potential (V)
ϕ	electrical potential parallel to surfaces (V)
ψ	electrical potential (V)
Γ	molar density of chargeable sites (mol m^{-2})
Δ	difference
Λ	density of chargeable sites (m^{-2})

Subscript

c	at the midplane of a channel

d	at the shear plane or at the OHP
i	*i*th
plug	plug-like propagation
+	counterion or hydronium
-	coion or hydroxide
0	at surface
∞	at infinite length, or in original bulk solution

Superscript

*	dimensionless quantities

CHAPTER 1

INTRODUCTION

1.1 Problem Statement and Motivation

Nanofluidic flow is generally referred to transport of fluids that are confined to the structures with at least one characteristic dimension below 100 nm [1]. Transport phenomena in these structures present unique features that are not observed at microfluidic size scales or above because the interactions of fluid with solid surfaces become prominent due to the drastically large surface-to-volume ratio. The primary physical mechanisms of nanofluidic transport include van der Waals forces and electrostatic forces, accounting for short and long-range interactions between related chemical components in liquid and surfaces, respectively.

Electrostatic forces, resulting from surface charges, cause an organized charge distribution near the solid surface known as the electrical double layer (the EDL). Electrostatics in the EDL and the resulting electrokinetic effects are the most important physical phenomenon in nanofluidic transport. When fluid is confined in a structure at nanoscale, such as in a nanochannel, the EDLs from opposite walls may have strong interactions. The phenomenon is called the EDL overlap, which results in significant changes in the composition of the fluid, the related electric field, and the fluid dynamic properties. Electrokinetic flows under the EDL overlap condition may have important applications in DNA analysis, drug delivery, analyte separation, power generation, and flow control [1-4]. For example, the efficiency of electric power generation by means of pressure driven nanofluidic flow was found to have its maximum at a certain level of EDL overlap [5, 6].

With the development of these applications, there is increasing need to better understand electrokinetic effects, particularly with the presence of the EDL overlap.

In this research, we examine electrokinetic effects for systems that are not less than 10 nm, in which van der Waals forces are insignificant comparing to electrostatic forces. A benefit from this restriction is that it is appropriate to apply continuum equations in modeling [4]. For smaller systems of less than ~10 nm where dynamic behavior of individual molecules becomes dominant, the continuum approach is not applicable in principle, but the understanding based on the continuum modeling are still beneficial as a quantitive reference.

In addition, we focus on electrokinetic effects caused by charged surfaces made of silica, mainly because silica are among the most popular materials in microfluidics and nanofluidics [7]. The electrochemical charges on silica surfaces are primarily caused by the proton exchange between surface chemical groups and the contacting salt solutions. The proton exchange has effects not only on surface charges, but also on the bulk pH. However, the variation of bulk pH due to this interaction has not drawn sufficient attention in existing studies on electrokinetic flows. Thus, there is a need to quantify the bulk pH and to further investigate its influence on electrokinetic flows.

1.2 Research Goals and Objectives

The research aims to quantify the pH change in electrokinetic flows under conditions of EDL overlap, which readily occurs for dilute electrolyte solution confined in a space with at least one dimension at nanoscale, and to examine the influence of the pH

change on electrokinetic effects. We focus on the pressure-driven flow in a slit-like nanochannel made of silica with various level of EDL overlap in this study.

The overall goals of this study are listed as below:

1) Quantify the pH change in the pressure-driven flow confined between silica walls under conditions of EDL overlap.
2) Indentify the influence of EDL overlap on the EDL structure, and transport phenomena of the pressure-driven flow.
3) Clarify the applicability of the Boltzmann distribution in an overlapped EDL in electrokinetic flows.

To achieve the goals, the specific objectives of this work are listed as below:

1) Establish analytic models for the fully-developed, steady-state, and pressure-driven flow of salt-free water and binary salt solutions, respectively, through a nanochannel connecting to a reservoir at each end.
2) Identify the structure of an overlapped EDL based on the new developed models and evaluate the influence of EDL on bulk pH, surface charge, and flow dynamics.
3) Numerically simulate the unsteady flow of binary salt solutions in a 2D nanochannel within an overlapped EDL. Simulation results are used to validate the analytic models, and to capture the transient phenomena of ion transports starting from electrostatic equilibrium to final stationary equilibrium.
4) Perform dimensionless analysis for the transient pressure driven flow.

The analysis intends to reveal the importance of taking hydronium and hydroxide ions into account to electrokinetic flows within overlapped EDL limits, leading to new knowledge of EDL overlap. The study can improve the fundamental understanding of the

EDL overlap and provide advances on the applications of taking use of EDL overlap in nanofluidic devices.

1.3 Overview of the Dissertation

In this dissertation, we first present the background knowledge related to electrokinetic flows in Chapter 2. The mathematic descriptions for electrokinetic transport phenomena and for chemical equilibrium on silica surfaces are summarized in Chapter 3. The next two chapters are presented in the form similar to papers, which includes conclusions. Chapter 4 investigates the structure of an overlapped EDL in salt-free water, and the relevant electrokinetic effects. Chapter 5 focuses on the electrokinetic flow of binary salt solutions. The fully-developed steady pressure-driven flow within an overlapped EDL is modeled. The modeled EDL structure is compared with that at electrostatic equilibrium to reveal the influence of the flow. The transient behavior of the pressure driven flow in a nanochannel is further simulated and discussed in Chapter 6. Main conclusions and contributions from the dissertation study are presented in Chapter 7.

CHAPTER 2

LITERATURE REVIEW AND BACKGROUND

Electrokinetic effects is one of the biggest concerns in the microfluidics and nanofluidics flow. Because it is resulted from the unbalanced charge distribution in the electric double layer (EDL), some concepts and principles relating to the EDL are first introduced in this chapter. Next, we present a review on theoretical treatments of modeling ion distribution in the EDL, and briefly introduce the mechanism of charge generation on silica surfaces. Finally, the coupling effects between surface chemical groups and the bulk pH is discussed for electrokinetic flows with EDL overlap.

2.1 Electrical Double Layer

When liquid phase comes in contact with solid phase, charged species such as ions, electrons, and dipolar constituents change their positions in the neighborhood of the interface to minimize their total free energy. As a result, net charges accumulate on solid surfaces, generating an electric potential difference between the surface and any location in the liquid. Because of the electrostatic interaction, a number of counterions, referred to the ions of opposite surface charge, are attracted to the surface, while coions are repelled away. The unbalance charge distribution is then formed, and usually restricted to a thin layer of the liquid close to the surface. The layer is called the electrical double layer (EDL). The resulting composition of liquid in the EDL is significantly different from the original bulk fluid where the electroneutrality condition exists. The redistribution of ions tends to weaken the electric field originally created by surface charges, and they interact to retrieve

new electrostatic equilibrium.

The thickness of the EDL is commonly characterized by the Debye length κ^{-1}. κ is the Debye-Hückel parameter. The Debye length is strongly dependent on the type and concentration of ions. In a binary salt solution of 0.01 mM and 100 mM, for instance, κ^{-1} is equal to $100\ \mathrm{nm}$ and 1 nm, respectively. The EDL effects is of great importance to the flow in the structure with at least one dimension falling to the level of the Debye length.

Gouy-Chapman-Stern model (GCS) is the classic model widely used to describe the behavior of a solid-liquid interface. According the GCS model, there are two layers, the Stern layer and the Gouy or diffuse layer, in the neighborhood of the interface (Fig. 2.1). The Stern layer is the one next to the interface, while the diffuse layer is right out of the Stern layer. In the Stern layer, all ions are assumed to be immobile due to the strong electric force. Specifically adsorbed ions are bound tightly to the surface, locating at a plane called the inner Helmholtz plane(IHP), while nonspecifically adsorbed ions are assumed to be trapped at the outer Helmholtz plane OHP(OHP). The thickness of the Stern layer is commonly of the order of a little beyond one hydrated ion radius(~0.5 nm), or even one bare ion radius(~0.1 nm). Beyond the OHP is the diffuse layer, in which ions are mobile. Their distribution is assumed to obey the Boltzmann statistics physics, or the Boltzmann distribution.

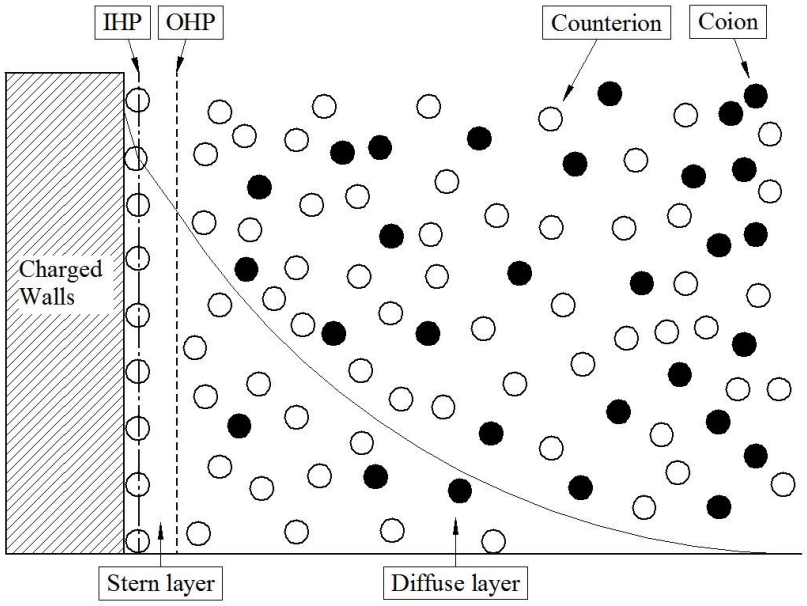

Fig. 2.1. Schematic diagram of electrical double layer

An electric potential field is formed in the EDL, and ions are redistributed due to the electrostatic interaction of surface charges and ions. The GCS model assumes that all ions adsorbed in the Stern layer are merely located either at the IHP or at the OHP, while the separate spaces between these planes and the solid surface are free of any charge. The dielectric permittivity is assumed to be identical inside the Stern layer, but different from the original bulk solution. Thus, the Stern layer behaves as parallel plate capacitors, in which the potential drops off linearly along the direction away from the surface. The potential drop continues throughout the diffuse layer until the charges restore neutral at the edge of the EDL double layer. In the diffuse layer, the permittivity of the solution is commonly assumed to be unaffected by the electric field. Thus, the potential exponentially decays, while ions obey the Boltzmann distribution.

In correspondence with the EDL structure, fluid dynamics is quite different inside the EDL. Stern proposed that there is an imaginary plane at a distance from the surface

below which the fluid is stationary along with those immobile ions. The imaginary plane is called the shear plane, which is usually defined as the meeting place of the Stern layer and the diffuse layer, i.e. the OHP in the GCS model. Therefore, fluid viscosity is regarded as an infinite number below the shear plane. In the remaining space of the EDL, fluid viscosity is commonly assumed to be constant. The electric potential on the shear plane is referred to the ζ potential, which has played an important role to electrokinetic flows.

2.2 Modeling for Ion Distributions in Electrokinetic Flows

As mentioned above, net surface charge attracts counterions and repel away coions in the diffuse layer. These mobile ions account for the primary reason for electrokinetic effects. In this section, we present a review of modeling ion distribution in a thin EDL, and in an overlapped EDL, respectively, for electrokinetic flows.

2.2.1 In a thin EDL

A thin EDL is referred to the one whose thickness is significantly less than the flow characteristic length. In the classic treatment of a thin EDL, ion distributions are related to local electric field with the assumption of Boltzmann equilibrium. This assumption is absolutely valid when the following conditions are satisfied: a) the finite size of ions can be neglected so that the ions are regarded as infinitesimal point charges, b) ions are considered as continuous distribution, and c) all interactions except electrostatic forces and Brownian motion can be disregarded. These conditions are quite loose for practical electrokinetic flows in a relative large system(>10 nm). Salt solutions used in electrokinetic flows are commonly not too dense with ion concentration less than 1 M. If there is no external forces

applied to the fluid, ions are controlled by diffusion and electromigration, which are related to Brownian motion and electrostatic forces, respectively. Thus, the Boltzmann equilibrium is assured. Even in the flow along the direction parallel to the surfaces, the Boltzmann distribution is still valid in a thin EML layer as examined in [8] and further discussed in Chapter 3.

Therefore, the Boltzmann equation coupled with the Poisson equation(the PB equation) is usually solved for the electric field, which is then used to determine ion distribution. The PB equation is a nonlinear second order differential equation, and its analytic solution has been well investigated in past studies. In the extreme case that the electric potential energy of electrolytes induced by surface charges is sufficiently lower than their thermal energy, the Debye-Hückel approximation can be used to linearize the PB equation and make it possible to find an analytical solution [9-12]. For symmetric salt solutions confined between two charged flat plates, analytical solutions have been proposed in terms of a first-kind elliptic integral with reference to the Zeta potential [13], or Jacobi elliptic functions [14-16]. In cases that the EDLs are not overlapped, the Gouy-Chapman solution is suitable for symmetric electrolytes [9, 17] or asymmetric 2:1 and 1:2 electrolytes [18].

2.2.2 In an Overlapped EDL

An overlapped EDL is formed as the EDLs from opposite surfaces tend to have a strong interaction. For a specific system, the existence and the degree of the EDL overlap is characterized by the comparison of the distance between opposite surfaces with the Debye length. The overlap of the EDLs readily occurs in dilute electrolyte solution confined in structures at nanoscale. For instance, in a channel with a half height H of 33 nm, the

monovalent electrolyte solution needs to be below 0.1 mM to form a strongly overlapped EDL with $\kappa H < 1$.

The EDL overlap brings some unique features of ion distribution and electric potential field. First, no electroneutrality exists in the fluid. The enrichment of counterions and the depletion of coions are spanned in the whole space including the region away from the solid surfaces. Second, there is no uniform electric potential field in the fluid. In the absence of EDL overlap, the electric potential rapidly decays to its bulk value and then maintains the value in the region out of an EDL. Such uniform electric potential distribution cannot be achieved in an overlapped EDL due to the loss of charge neutrality. The potential significantly decays from the surface to the midplane between the interacting surfaces.

The Boltzmann distribution was widely assumed in most studies dealing with an overlapped EDL. Stein and his colleague studied the pressure-driven flow in a nanochannel between two reservoirs[5, 6, 19-21]. They proposed a model with the assumption of the Boltzmann distribution for all species in the channel. The enrichment and depletion effects at the channel midplane due to the ELD overlap was particularly concerned by setting a nonzero electric potential. Baldessari and Santiago [22] suggested the same treatment, while Wang et al. [23, 24] used an enrichment coefficient denoted by the comparison of ion concentrations after and before the ELD overlap. Boltzmann equilibrium is established as salt solutions are relaxed for a sufficiently long time [25].

However, it is questionable to assume the Boltzmann distribution in an overlapped EDL. It was argued that the Boltzmann distribution is valid only for an infinite space where the electrolyte solution far away surfaces is neutral [7, 26-28]. Generally speaking, the

Nernst-Planck(NP) equation is a better description for ion distributions under this situation. The application of the NP equation requires additional constraints to complete modeling. The ion distribution obtained from the NP equation is usually referred to concentrations at the channel center. Their values are unknown under conditions of the EDL overlap, since they are not simply equal to those in the original bulk with the absence of the EDL overlap. Additional constraints must be added to determine the reference concentrations. Tessier and Slater put forward with a model for static salt solutions in a closed channel using the NP equation [29]. They assumed the conservation of each chemical species in the channel, including in the solution and on the surfaces. Li and his colleagues [7, 26-28] assumed the species conservation along the cross section including surfaces in their model. Water dissociation was particularly involved in their model to account for the enrichment of hydronium ions. With the assumption of species conservation, the modeled ion distributions theoretically exist only in a closed channel.

As far as we know, the current theoretical models are not appropriate for electrokinetic flows. In electrokinetic flows under conditions of the EDL overlap, ion transport along the flow direction is often dominated mainly by electromigration and convection, instead of diffusion. Apparently, the Boltzmann equilibrium is not appropriate, which concerns about the mechanism of electromigration and diffusion. The species conversation condition is not valid either as the EDLs are related to an open system in electrokinetic flows. Therefore, it is needed to put forward with new models to better understand electrokinetic flows.

2.3 Mechanisms of Proton Exchange on Silica Surfaces

The electric field in an EDL results from net charges accumulated at the solid-fluid interface. Typical physical mechanisms by which the charges are generated include a) the dissociation and association of surface chemical groups, b) ion adsorption from electrolyte solution, and c) crystal lattice defects. Charges on silica surfaces are mainly caused by the first two mechanisms that we briefly discuss below.

Typical chemical reactions relating to silanol groups at silica surfaces are written as [30]

$$SiOH \rightleftharpoons SiO^- + H^+, \tag{2-1}$$

$$SiOH_2^+ \rightleftharpoons SiOH + H^+. \tag{2-2}$$

Further protonation of siloxane groups($SiOH_2^+$) is disregarded as it is extremely low except under very acidic solutions(pH < 3) [31, 32]. Similarly, the protonation of other surface chemical groups such as Si_2O is considered inert [16, 31]. The dissolution of silica into silicate ions($HSiO_3^-$) is also ignored, which is considerable only in a very basic solution(pH > 9) [32]. The Stern layer model assumes that the charged components are located at the IHP.

According to the above chemical reactions, silica surfaces can be positively charged, negatively charged, or neutralized, dependent on the surface pH or the surface proton activity, denoted by pH_0. The surface pH at which negative and positive charges have the same number, is called the pH at the point of zero charge, denoted by pH_z. The surface is negatively charged for $pH_0 > pH_z$ as the dominant chemical reaction is the one described by Eq. (2-1), while positive charged for $pH_0 < pH_z$ due to the domination of the

reaction described by Eq. (2-2).

Once charged groups such as SiO^- and $SiOH_2^+$ are generated due to proton exchange, they attempt to adsorb other types of ions from the solution. This kind of adsorption is called nonspecific adsorption. If KCl solution is considered, for example, the following nonspecific adsorptions occur at the interface,

$$SiO^- + K^+ \rightleftharpoons SiOK, \quad (2\text{-}3)$$

$$SiOH_2^+ + Cl^- \rightleftharpoons SiOH_2Cl. \quad (2\text{-}4)$$

According to the Stern model, nonspecifically ions are located at the OHP.

With the increase of salt concentration, more ions are nonspecifically adsorbed. Nonspecifically adsorbed ions has significant effects on surface charge density only for salt solution with at high concentration(1 mM to 1 M) [32]. Because the EDL overlap readily occurs in dilute salt solution(<1 mM), we ignore the nonspecific adsorption throughout the dissertation research. In this study, the dissociation of silanol groups accounts for the generation of all charges in the Stern layer.

2.4 Coupling Effects of Surface Charges and the Bulk pH

Surface charges have a strong interaction with the bulk pH as they both are associated with the surface pH. At the surfaces, there is an adsorption-desorption equilibrium between protons and silanol groups as mentioned above. On the other hand, there is Boltzmann distribution inside the EDL the surface proton is related to the pH in the solutions, referring to as the bulk pH, because of the electrostatic effects and Brownian motion. Thus, it can be anticipated that surface charge has an interaction with the bulk pH in two

aspects.

First, an appropriate bulk pH adjustment changes the surface pH, and then forces the establishment of a new equilibrium to change the composition of surface chemical groups. It has been well realized in past studies that the amount or even the sign of surface charge is controllable by simply presetting the bulk pH with a buffer solution. The electrostatic balances are dramatically sensitive to the bulk pH.

Second, the bulk pH seems to be affected by the proton transfer as well. In recent experiments, a notable pH variation was observed inside a silica oxide nanochannel of ~50 nm high in the process of filling water, 0.073-0.5 M HCl or KCl solution [33]. The reason was clearly concluded as the addition of surface-released protons into the bulk flow. The variation of bulk pH may also exist in electrokinetic flows in spite of lack of strong evidence. Van der Heyden et al. [6] reported an interesting and unexplained transient behavior of the streaming conductance of 0.01 mM KCl solution in a silica nanochannel of 75 nm high, 50 μm wide and 4.5 mm long. The measured streaming conductance, which is a quantity strongly dependent on charge density in the EDL, was often very low in hours upon initially filling before creeping to stable values. This phenomena can be qualitatively explained by the pH shifting during relaxation as discussed in Chapter 5.

However, the possible variation of the bulk pH has not drawn sufficient attention in the traditional theory for electrokinetic flows. The main reason for such an omission is that electrokinetic flows are typically investigated within non-overlapped EDLs out of which surface-dissociated hydronium ions are mostly diffused into the bulk flow [27, 28]. The other reason is that the pH variation seems to be depressed with the addition of buffer solutions, which is often the case in experimental studies [5, 6, 19, 20, 34]. When electro-

kinetic flows are considered within an overlapped EDL, protons are confined in a narrow space and may be enriched so strongly as to surpass the buffer capacity, leading to an erroneous estimate of the solution pH if made depending on the buffer capacity. Finally, it is probably because the EDLs commonly exist in open systems where surface-dissociated hydronium ions are eventually diffused out of the EDLs into somewhere else, such as a reservoir. Thus, the consideration of the effects of surface chemical equilibrium on the bulk pH is particularly noteworthy under conditions of EDL overlap. The coupling effects between the bulk pH and surface charges must be taken into account in modeling electrokinetic flow within an overlapped EDL.

2.4 Dissociation Equilibrium of Water

In order to model the variation of the bulk pH, it is necessary to consider the pH-determined chemical equilibrium in the solution, which were ignored in most previous models dealing with the effects of EDL overlap [19, 22, 35-38]. In the absence of the pH related buffer electrolyte in the solution, protons(hydronium ions) are in balance with hydroxide ions and water molecules. The dissociation equilibrium of water plays a critical role in buffering the variation of protons in the solution. Meanwhile, the transport of hydronium and hydroxide ions needs to be taken into account though their numbers might be orders of magnitude less than those of other electrolyte in the bulk solution. Thus, it is needed to develop the overall model including water dissociation equilibrium, surface equilibrium and the contribution of hydronium and hydroxide ions for better understanding electrokinetic flows under conditions of EDL overlap.

CHAPTER 3

MATHEMATIC DESCRIPTIONS OF ELECTROKINETIC FLOWS

In this chapter we present the mathematic description of electrokinetic flows of interest. The governing equations of electrokinetic transport phenomena in the diffuse layer are presented for continuous, incompressible and Newtonian flows in the first section. In the next section, we introduce a theory that combines the zeroth-order Stern model with the site dissociation model to describe the electric field in the Stern layer including on the surface. The mathematic framework presented in this chapter has been well established for over at least decades, and will be applied for specific modeling throughout the dissertation.

3.1 Electrokinetic Transport in the Diffuse Layer

Transport phenomena we discuss here are restricted to the diffuse electrical layer, where both fluid and chemical species are assumed to be mobile according to the Stern layer model.

3.1.1 Fluid Transport

The continuum approach can be used to describe fluid transport in nanofluidic systems of interest(> 10 nm). A straightforward analysis on the applicability of continuum theory via Knudsen number suggests that the continuum theory breaks down for water transport in systems with a characteristic length as small as ~3 nm, provided that Knudsen number of 1 is defined as the transition point between continuum and discrete flow [4]. It is also concluded by the comparison between molecular dynamics and continuum simula-

tions that the continuum theory is applicable in channels with a height down to 2.22 nm [39]. Thus, electrokinetic flows are described by the Navier-Stokes equations.

The continuity equation is given by,

$$\nabla \cdot u = 0 \tag{3-1}$$

where u is the bulk flow velocity, and fluid is treated as incompressible because the pressure increase is usually restricted to a few bars in most applications of electrokinetic flows.

Electrokinetic flows are characterized by the presence of an electric body force which arises from the existence of charged species in an electric field. The electric field associated with electrokinetic flows is commonly generated by one or a few sources including net surface charges, an applied electric potential gradient, and/or a streaming potential gradient which is induced by the accumulation of counterions downstream in the pressure-driven flow. Therefore, the momentum equation with an electrical body force term is given by

$$\rho \frac{\partial u}{\partial t} + \rho(u \cdot \nabla)u = \mu \nabla^2 u - \nabla p - \rho_e \nabla \psi \tag{3-2}$$

where p is the pressure, ρ the fluid density, t the time, μ the fluid viscosity, F the Faraday constant, ψ the electric potential, ρ_e local charge density which is defined by $\rho_e = F\Sigma z_i c_i$. F is Faraday's number, z the valence, c the molar concentration, and subscript i denotes ith ion. The nonlinear advection term on the LHS is retained for completeness, although it is usually negligible because of low Re number in most of the electrokinetic flows. In accordance with the Stern model, μ is assumed to be constant everywhere in the diffusive layer as well as in the region out of the EDL. A recent review on nanofluidics also shows

that this assumption is unlikely to be broken unless the channel is extremely narrow(height < 5nm) [4]. The third term on the RHS accounts for the electrical body force, which is insignificant out of the diffuse layer due to the electroneutrality. The advective term on the LHS can be neglected in most cases of electrokinetic phenomena as the Reynolds number usually falls between 10^{-6} ~ 1.

3.1.2 Chemical Species Transport

The motion of chemical species in electrokinetic flows are generally attributed to the diffusion due to the Brownian motion, the convection accompanying with fluid transport, and the electromigration caused by the electrostatic forces. Aside from physical mechanisms, some species are in chemical equilibriums so that they may transport in various chemical groups. We first describe the species transport in strong electrolyte solutions where the electrolyte is fully dissociated to free ions, and then discuss the transport in weak electrolyte solutions.

3.1.2.1 Strong Electrolyte

A strong electrolyte such as KCl is completely dissociated into free ions, which have no chemical binding with each other. According to the mass conservation law, the transport of these ions in the absence of chemical reactions is governed by the NP equation,

$$\frac{\partial c_i}{\partial t} + \nabla \cdot j_i = 0 \tag{3-3}$$

$$j_i = -D_i \nabla c_i + c_i u + \frac{z_i F D_i}{RT} c_i \nabla \psi \tag{3-4}$$

where j is the flux density, D the diffusivity, R the universal gas constant, and T the temperature. The electrolyte mobility is related to the diffusivity as D_i/RT using the

Nernst-Einstein relation. The first term of Eq. (3-3) represents the rate of change of ion concentration in a unit volume while the second term is the rate at which ions enter the volume. The terms on the RHS of Eq. (3-4) represent the effects of diffusion, convection and electromigration, respectively. The NP equation is also applicable for neutral components whose transport is governed by diffusion and convection. Under some special conditions, such as at electrostatic equilibrium, the NP equation can be simplified to give an explicit expression of ion concentrations in terms of the electric potential.

At electrostatic equilibrium, the NP equation leads to the Boltzmann distribution. The diffusion and electromigration must be in balance with each other since the convection term and the time-dependent term in Eq. (3-3) are zero. For an infinite large plane surface, in a Cartesian coordinate system whose *y* direction is normal to the plane, Eq. (3-3) is re-written as

$$-\frac{\partial^2 c_i}{\partial y^2}+\frac{F}{RT}\frac{\partial}{\partial y}\left(c_i\frac{\partial \psi}{\partial y}\right)=0 \tag{3-5}$$

The potential and ion concentration vary only along *y* direction in an EDL. Provide that the electrolyte solution is confined in a half-infinite space, an electroneutrality condition is achieved at an infinite distance away from the surface($y = \infty$), such that $\frac{\partial c_i(y=\infty)}{\partial y} = \frac{\partial \psi(y=\infty)}{\partial y} = 0$ and $c_i(y = \infty) = c_{i,\infty}$. Integrating Eq. (3-5) twice with respect to *y* and applying the boundary conditions at $y = \infty$, yields the Boltzmann distribution,

$$c_i = c_{i,\infty}\exp\left(-\frac{z_i F\psi}{RT}\right) \tag{3-6}$$

where $c_{i,\infty}$ is the original ion concentration, and $\psi(y = \infty)$ is referred as zero. Though Eq. (3-6) is derived from the 1D variation of ion concentration and electric field, it holds in

three dimensional space as long as the electrolyte solution is at equilibrium and the electroneutrality exits somewhere in liquid.

Under conditions of electrokinetic flows, the derivation of the Boltzmann distribution from the NP equation is pretty strict, requiring a few assumptions: a) ion distribution is stationary to remove the time derivative term, b) Significant variation of concentration and electric potential occurs only normal to the surfaces, c) the EDLs are not overlapped so that the original bulk concentration remains far away from the charged surface. The streaming potential field is commonly much smaller than the internal field caused by surface charges. Therefore, when the flow is fully developed and at steady state, the assumptions of a) and b) are acceptable. The applicability of the Boltzmann distribution depends on whether the EDLs are overlapped or not. For the fully-developed steady flow, Eq. (3-3) is simplified to

$$-\frac{\partial^2 c_i}{\partial y^2}+\frac{F}{RT}\frac{\partial}{\partial y}\left(c_i\frac{\partial \varphi}{\partial y}\right)=0 \tag{3-7}$$

where φ is the potential field caused by surface charges and normal to the wall. In the absence of EDL overlap, the original ion concentration remains in the channel, i.e. $c_i(y=\infty) = c_{i,\infty}$. The solution to Eq. (3-7) can be obtained in a way similar to the derivation of Eq. (3-6) and gives rise to

$$c_i = c_{i,\infty}\exp\left(-\frac{z_i F\varphi}{RT}\right) \tag{3-8}$$

The identity of Eqs. (3-6) and (3-8) demonstrates the existence of the Boltzmann distribution in a thin EDL under the current flow conditions. However, the presence of EDL overlap breaks down the Boltzmann distribution as the last assumption mentioned above is not satisfied. Nevertheless, Eq. (3-7) can be similarly solved, yielding [8],

$$c_i = c_{i,c}\exp\left(-\frac{z_i F\varphi}{RT}\right) \tag{3-9}$$

where subscript *c* represents quantities at the position where the opposite EDLs meets, and φ_c is imposed as zero. In a nanochannel, for example, this position is regarded as the channel midplane. $c_{i,c}$ are unknowns and need to be solved by applying some other constraints.

3.1.2.2 Weak Electrolyte

As a weak electrolyte is dissolved in water, its individual components do not completely dissociate, and their transport may be significantly affected by the interaction between them. Buffer solutions, containing at least a weak electrolyte, have been widely used in experimental studies in attempt to control the pH in an EDL. However, the transport of buffer solution was barely considered in modeling electrokinetic flows in past studies, as the buffer components are generally a few orders of magnitude less than other electrolytes of interest. Because the EDL overlap readily occurs in dilute ionic solutions with relative concentrate buffer, the influence of buffer solutions becomes considerable on the structure of the EDL. Thus, it is of importance to understand the transport of weak electrolytes, particularly for electrokinetic flows within an overlapped EDL.

For simplicity we consider binary electrolyte the following dissociation reaction,

$$\mathrm{A^+ + B^- \leftrightharpoons AB} \tag{3-10}$$

The relation between the components is related to the dissociation equilibrium constant K_{AB}, which is defined as

$$K_{\mathrm{AB}} = c_{\mathrm{A^+}} c_{\mathrm{B^-}} / c_{\mathrm{AB}} \tag{3-11}$$

We further assume that the chemical equilibrium is established much faster than other physical processes. Therefore, K_{AB} can be assumed to identical in electrokinetic flows.

To account for the relevant chemical changes, a source term is added to the conservation equation of A^+, B^-, and AB as below

$$\frac{\partial c_i}{\partial t} + \nabla \cdot j_i + G_i = 0 \tag{3-12}$$

where G is the generation rate per unit volume. If there is no chemical reactions but the one in Eq. (3-10), the generation of A^+ and B^- must be at the same amount as the elimination of AB. The relation between the generation rates of A^+, B^-, and AB is given by

$$G_{A^+} = G_{B^+} = -G_{AB} \tag{3-13}$$

The coupling transport of all the components in electrokinetic flows is the most important feature of weak electrolyte solution.

A very special case of the weak electrolyte is water, which itself is at the dissociation equilibrium between H^+, OH^- and neutral water molecules. Without considering any other pH related buffer, the transport of H^+ and OH^- in water can be obtained by rewriting Eqs. (3-11)-(3-13) as

$$\frac{\partial c_{H^+}}{\partial t} + \nabla \cdot j_{H^+} + G_{H^+} = 0 \tag{3-14}$$

$$\frac{\partial c_{OH^-}}{\partial t} + \nabla \cdot j_{OH^-} + G_{OH^-} = 0 \tag{3-15}$$

$$G_{H^+} = G_{OH^-} \tag{3-16}$$

$$c_{H^+} c_{OH^-} = K_{H_2O} \tag{3-17}$$

Applying Eqs. (3-4) and (3-15)-(3-17) to eliminate the source term in Eq. (3-14), the NP equation of H^+ is given by

$$\left(1+\frac{K_{H_2O}}{c_{H^+}^2}\right)\left(\frac{\partial c_{H^+}}{\partial t}+u\cdot\nabla c_{H^+}\right)=D_{H^+}\nabla\cdot\left[\left(1+\frac{D_{OH^-}K_{H_2O}}{D_{H^+}c_{H^+}^2}\right)\left(\nabla c_{H^+}+\frac{Fc_{H^+}}{RT}\nabla\psi\right)\right] \quad (3\text{-}18)$$

Eq. (3-18) can be successfully reduced to either Eq. (3-5) or (3-7) if transport of H^+ is assumed under the corresponding flow conditions. Therefore, the distribution of H^+ in the EDL is described by Eq. (3-6), (3-8) or (3-9)**.** We use those analytical solutions for modeling the distribution of H^+ in this study.

3.1.3 Electric Field

The electrical potential and ion concentration are related by the Poisson equation

$$\nabla\cdot\nabla\psi=-\frac{\rho_e}{\varepsilon\varepsilon_0} \quad (3\text{-}19)$$

where ε is the dielectric constant of the electrolyte solution and is assumed to be constant everywhere in the bulk solution starting from the shear plane. ε_0 is the dielectric permittivity of vacuum.

The potential in electrostatic equilibrium situation can be determined by combining the Poisson equation of Eq. (3-19) and the Boltzmann equation of Eq. (3-6)

$$\nabla\cdot\nabla\psi=-\frac{F\sum c_{i,\infty}z_i}{\varepsilon\varepsilon_0}\exp\left(-\frac{z_iF\psi}{RT}\right) \quad (3\text{-}20)$$

Eq. (3-20) is so called the Poisson-Boltzmann equation (the PB equation) which is one of the most important equations for fundamental understanding of colloids, electrochemistry and electrokinetic phenomena. The PB equation is usually expressed in a dimensionless form, such as

$$\nabla^*\cdot\nabla\psi^*=(\kappa H)^2\sinh(\psi^*) \quad (3\text{-}21)$$

where $\psi^*=-z_iF\psi/RT$, $\nabla^*=H\nabla$, and H is the characteristic length. $\kappa=(F^2\Sigma c_{i,\infty}z_i^2/\varepsilon\varepsilon_0RT)^{1/2}$, is the Debye-Hückel parameter. Superscript * represents dimensionless quantities.

3.2 Electric Field and Surface Charge in the Stern Layer

In this section we introduce the classic theory of modeling the electrical field in the Stern layer and the charge density at silica surfaces.

3.2.1 Zeroth-Order Stern Model

The simplest one of Stern models, called zeroth-order Stern model [30] or the basic Stern model [15, 40] assumes that only specifically adsorbed ions are attractive at the IHP in the Stern layer. There is free of ions between the IHP and the OHP, and nonspecifically adsorbed ions at the OHP. According to Gauss's law, net charge in the EDL including on the surface must be in neutrality, yielding

$$\sigma_d + \sigma_0 = 0 \tag{3-22}$$

where σ_d is the total charge density of mobile ions in the diffusive layer, and σ_0 is the charge density at the IHP, namely surface charge density.

Since no charges are contained between the surface and the OHP, this region acts as a parallel plate capacitor whose effective capacity is characterized by

$$C = \frac{\sigma_0}{\psi_0 - \psi_d} \tag{3-23}$$

where ψ_0 is surface potential, the potential at the IHP, and ψ_d is the potential at the OHP.

If we further regard the OHP as the shear plane beyond which fluid may start to move, the effective capacity can be rewritten as

$$C = \frac{\sigma_0}{\psi_0 - \zeta} \tag{3-24}$$

where ζ is the potential at the shear plane.

The zeroth-order Stern model is an appropriate depiction for dilute electrolyte so-

lution in contact with silica surfaces. In the case of high salt concentration, we need use more sophisticated models such as electrical triple-layer model to concern the influence of nonspecifically adsorbed ions [32, 41].

3.2.2 Dynamic Single Site Model

We now present a straightforward model to determine surface charge density assuming that charges are all generated due to the deprotonation of silanol groups. Thus, the surface adsorption is associated with the chemical reaction represented by Eq. (2-1), rewritten as

$$\mathrm{SiOH} \rightleftharpoons \mathrm{SiO^-} + \mathrm{H^+} \tag{2-1}$$

The presented model is restricted to weak acidic or basic solution in which the protonation of silanol groups (Eq. (2-2)) is insignificant comparing to the deprotonation (Eq. (2-1)) [16, 30] and can be ignored. Without the consideration of the protonation effects, the surface is always negatively charged no matter what the bulk pH is. It is in apparent contradiction with the fact that positively charges dominate silica surfaces in a strong acidic solution.

If surface silica components do not diffuse inside the surface material or dissolve into the bulk solution, the total concentration of chargeable sits is assumed to be unchanged during the transient process of electrokinetic flows, yielding

$$\Gamma_{\mathrm{total}} = \Gamma_{\mathrm{SiOH}} + \Gamma_{\mathrm{SiO^-}} \tag{3-25}$$

where Γ_{total}, Γ_{SiOH} and $\Gamma_{\mathrm{SiO^-}}$ are the molar density of total chargeable sites, SiOH groups and $\mathrm{SiO^-}$ groups on the surface. $\Gamma_{\mathrm{total}} = \Lambda/\mathrm{Av}$, where Λ is the site number density and Av is the Avogadro's number.

The governing equation for dynamic association-dissociation process of silanol

groups is given by

$$\frac{\partial \Gamma_{\mathrm{SiO^-}}}{\partial t} = K_2 \Gamma_{\mathrm{SiOH}} - c_{\mathrm{H^+},0} K_1 \Gamma_{\mathrm{SiO^-}} \tag{3-26}$$

Here, $c_{\mathrm{H^+},0}$ is the surface activity of protons, which is assumed to equal its local molar concentration. K_1 is the reverse equilibrium reaction rate constant with which the concentration of SiO^- and H^+ determines the binding rate of H^+ on surfaces. K_2 is the forward equilibrium reaction rate constant used to characterize the dissociation rate of SiOH, or the generation rate of H^+ due to the dissociation. K_1 and K_2 are correlated using the logarithmic dissociation constant, pK, that is

$$\frac{K_2}{K_1} = 10^{-\mathrm{pK}}[\mathrm{mol/l}] \tag{3-27}$$

Combing Eqs. (3-25) and (3-26), $\Gamma_{\mathrm{SiO^-}}$ is related to $c_{\mathrm{H^+},0}$ in terms of surface properties

$$\frac{\partial \Gamma_{\mathrm{SiO^-}}}{\partial t} = K_2(\Gamma_{\mathrm{total}} - \Gamma_{\mathrm{SiO^-}}) - c_{\mathrm{H^+},0} K_1 \Gamma_{\mathrm{SiO^-}} \tag{3-28}$$

Surface charge density σ_0 is attributed to the dissociation of silanol groups, giving rise to

$$\sigma_0 = -F\Gamma_{\mathrm{SiO^-}} \tag{3-29}$$

When the equilibrium state is achieved, the density of SiO^- groups does not change with respect to time,

$$\frac{\partial \Gamma_{\mathrm{SiO^-}}}{\partial t} = 0 \tag{3-30}$$

Combining Eqs. (3-27)-(3-30), the surface charge density at equilibrium is given by

$$\sigma_0 = -\frac{F\Gamma_{\mathrm{total}}}{c_{\mathrm{H^+},0} 10^{\mathrm{pK}} + 1} \tag{3-31}$$

3.2.3 Two Sites Model

When the surface pH is close to pH_z in a acidic solution, the magnitude of surface charge results from the balance between SiO^- and $SiOH_2^+$ groups. It is better to model the surface charge density on silica surfaces using the two sites model which assumes the following chemical reactions

$$SiOH \rightleftharpoons SiO^- + H^+ \quad (2\text{-}1)$$

$$SiOH_2^+ \rightleftharpoons SiOH + H^+ \quad (2\text{-}2)$$

with the dissociation constants K_a and K_b

$$K_a = 10^{-pK_a} = \frac{\Gamma_{SiO^-} \cdot c_{H^+,0}}{\Gamma_{SiOH}} \quad (3\text{-}32)$$

$$K_b = 10^{-pK_b} = \frac{\Gamma_{SiOH} c_{H^+,0}}{\Gamma_{SiOH_2^+}} \quad (3\text{-}33)$$

Again, we assume that the number of chargeable sites is not varied during the proton transfer process, that is

$$\Gamma_{total} = \Gamma_{SiOH} + \Gamma_{SiO^-} + \Gamma_{SiOH_2^+} \quad (3\text{-}34)$$

Surface charge density is related to charged sites on the surface by

$$\sigma_0 = F\left(\Gamma_{SiOH_2^+} - \Gamma_{SiO^-}\right) \quad (3\text{-}35)$$

Combining Eqs. (3-32) and (3-33) and applying $\Gamma_{SiOH_2^+} = \Gamma_{SiO^-}$, we can obtain the pH of a point of zero charge

$$pH_z = \frac{pK_a + pK_b}{2} \quad (3\text{-}36)$$

It is usually to define the difference of the logarithmic equilibrium constants ΔpK for convenience

$$\Delta pK = pK_a - pK_b \quad (3\text{-}37)$$

ΔpK and pH_z along with Γ_{total} are the most important parameters in this approach to model the related chemical reactions. All of them are properties of the surface material.

From Eqs. (3-32)-(3-37), we may establish the relation between the charge density and the proton activity on the surface as

$$\sigma_0 = \frac{F\Gamma_{total}\delta \sinh[2.3(pH_z - pH_0)]}{1+\delta \cosh[2.3(pH_z - pH_0)]} \tag{3-38}$$

where $\delta = 2 \times 10^{-\Delta pK/2}$, and pH_0 is the surface pH given by $c_{H^+,0} = 10^{-pH_0}$.

In the traditional theory of dealing with a thin EDL, the surface activity of protons is related to the bulk activity by Eq. (3-6) due to the Boltzmann distribution. Thus, Eq. (3-38) is rewritten as

$$\sigma_0 = \frac{F\Gamma_{total}\delta \sinh\left[2.3(pH_z - pH_\infty) - \frac{F\psi_0}{RT}\right]}{1+\delta \cosh\left[2.3(pH_z - pH_\infty) - \frac{F\psi_0}{RT}\right]} \tag{3-39}$$

where pH_∞ is the original bulk pH given by $c_{H^+,\infty} = 10^{-pH_\infty}$. Eq. (3-39) was first derived by Healy and White [30].

For the steady state flow in an infinite long nanochannel, the distribution of protons is governed by Eq. (3-9). And we use the zeroth-order Stern layer model to describe the electric field in the Stern layer. The substitution of Eqs. (3-9) and (3-24) into Eq. (3-38) gives

$$\sigma_0 = \frac{F\Gamma_{total}\delta \sinh\left[2.3(pH_z - pH_c) - \frac{F}{RT}\left(\frac{\sigma_0}{C} + \zeta\right)\right]}{1+\delta \cosh\left[2.3(pH_z - pH_c) - \frac{F}{RT}\left(\frac{\sigma_0}{C} + \zeta\right)\right]} \tag{3-40}$$

where pH_c is the pH at the channel center, given by $c_{H^+,c} = 10^{-pH_c}$. Eq. (3-40) defines σ_0 as a function of ζ and pH_c in the presence of EDL overlap.

CHAPTER 4

SALT FREE WATER IN A NANOCHANNEL

4.1 Introduction

Salt-free water in a slit-like nanochannel is investigated in this chapter as first step for studying the impact of surface association-dissociation equilibriums on the bulk pH under conditions of the EDL overlap. We started the research with salt-free water mainly because of the simplicity that no salt ions but hydronium and hydroxide ions are taken into account. Through this study on salt-free water, however, a solution methodology can be established for further analysis on dilute salt solution in a nanochannel. In the meanwhile, the results we obtained from salt-free water could be used for reference in modeling dilute salt solutions, which approach salt-free under the condition of extremely low salt concentration.

In this chapter, we aim to quantify the effects of surface-solution equilibrium interactions on the bulk pH for salt-free water in an overlapped EDL, and to provide an applicability range of an approximate model. The electric potential field and ion distribution across the channel are modeled by the Poisson equation and the NP equation, with the consideration of water dissolution equilibrium and surface adsorption-desorption equilibrium. Exact and approximate analytical solutions of the Poisson-Nernst-Planck (PNP) equation are derived for water, but they can be applied for other binary salt solutions as well. The exact solution, which is expressed in terms of Jacobian elliptic functions, is accurate but a little complicated for applications. On the contrary, the approximate solution is easy to use but restricted to circumstances of strong EDL overlap. Based on analytical

solutions of ion distribution and electric field, the dynamic behaviors of the pressure driven flow are next analyzed. The established solution methodology for salt-free water is applied to salt solutions in Chapter 5.

4.2 Electric Potential Field and Ion Distribution

Salt-free water is investigated in a slit-like silica channel with the EDL whose thickness is similar to or less than the channel height. Hydronium and hydroxide ions are the only charged species considered in water. The studied channel is bounded between two plane walls with a height of $2H$, and is sufficiently long and wide so that the entrance effects and sidewall effects are negligible. A Cartesian coordinate system is used where the x-axis is in the streamwise direction and the y-axis in the transverse direction. The walls are located at $y = \pm H$, while the channel midplane at $y = 0$.

4.2.1 Mathematic Model

The electric field in an EDL can be regarded as the superposition of two independent electric field components: one is along the streamwise direction caused by an induced or applied external electric field, and the other is along the transverse direction created by the surface charge. In electrokinetic flows, the streamwise potential gradient is generally much smaller than the transverse one in an EDL. Thus, the transverse electric field that can be related to ion distribution by the Poisson equation [9], and Eq. (3-20) is rewritten as

$$\frac{\mathrm{d}^2\varphi}{\mathrm{d}y^2} = -\frac{F(c_+ - c_-)}{\varepsilon\varepsilon_0} \tag{4-1}$$

where φ is the transverse electric potential in the channel, $c_{\pm}$ are molar concentrations of counterions and coions. Silica surfaces are commonly negatively charged. Thus, H^+ is the counterion enriched in the EDL while OH^- is the coion to be concerned.

The influence of the transverse electric field on ion distribution is described by the one dimensional NP equation. Distributions of H^+ and OH^- are given by Eq. (3-9), re-written as

$$c_{\pm} = c_{\pm c}\exp\left[\mp\frac{F}{RT}(\varphi - \varphi_c)\right] \tag{4-2}$$

where φ_c is the potential at the channel midplane, against which the transverse electric potential is evaluated. Its value is not set as zero as we did in derivation of Eq. (3-9) in order to clarify its physical meaning in later discussion. Because the opposite EDLs are overlapped, counterion is in higher concentration at the channel center than what it was in the original liquid, while coion is in lower concentration. Hence $c_{\pm c}$ are unknown priories whose determination is critical to quantify ion distributions across the channel.

By combining Eq. (4-2) with Eq. (4-1), and normalizing relevant parameters, the dimensionless PNP equation is expressed as following

$$\frac{d^2\varphi^*}{dy^{*2}} = \frac{(\kappa H)^2}{2}\left[c^*_{+c}\exp(\varphi^* - \varphi^*_c) - c^*_{-c}\exp(\varphi^*_c - \varphi^*)\right] \tag{4-3}$$

where $\varphi^* = -F\varphi/RT$, $y^* = y/H$, $c^*_{\pm} = c_{\pm}/c_{\infty}$, and $\kappa^2 = 2c_{\infty}F^2/\varepsilon\varepsilon_0 RT$. c_{∞} is the original molar concentration of H^+ or OH^- in water, and superscript * represents dimensionless parameters. Eq. (4-3) can be rewritten in terms of hyperbolic function as [29]

$$\frac{d^2\varphi^*}{dy^{*2}} = \left(\kappa_{eff}H\right)^2 \sinh(\varphi^* + \varphi^*_{chm} - \varphi^*_c) \quad (4\text{-}4)$$

where $\kappa_{eff} = \kappa(c^*_{+c}\ c^*_{-c})^{1/4}$ is an effective Debye parameter, and $\varphi^*_{chm} = \ln(c^*_{+c}/c^*_{-c})/2$ is associated with the enrichment and depletion effects at the channel midplane. It is equivalent to an additional electric potential being combined with the real electric field. Eq. (4-4) approaches the PB equation (Eq. (3-21)) as $\kappa_{eff} \cong \kappa$ and $\varphi^*_{chm} \cong 0$ in the absence of EDL overlap.

Eq. (4-4) is subjected to the following boundary conditions at the channel center

$$\frac{d\varphi^*(y^*=0)}{dy^*} = 0, \varphi^*(y^* = 0) = \varphi^*_c \quad (4\text{-}5)$$

The first boundary condition is symmetric condition, and the second one results from the definition of the potential reference. It should be noted that Eqs. (4-4) and (4-5) are not limited to salt-free water. They as well as the corresponding solutions are applicable for other symmetric salt solutions, such as KCl solution.

4.2.2 Exact Solution

The exact analytical solution of Eq. (4-4) subject to Eq. (4-5) has been derived by Behrens and Borkovec [14, 15]. In the case of $\varphi^* + \varphi^*_{chm} - \varphi^*_c > 0$, it can be written as

$$\varphi^* - \varphi^*_c = -2\ln[\mathrm{cd}(n|m)] \quad (4\text{-}6)$$

where cd is a Jacobian elliptic function of argument $n = \kappa_{eff}Hy^*\exp(-\psi^*_{chm}/2)/2$, and parameter $m = \exp(-2\varphi^*_{chm})$. Behrens and Borkovec [14] proposed a solution in the same form but with different Jacobian argument and parameter such as, $n = \kappa Hy^*\exp(\varphi^*_c/2)$ and $m = \exp(-2\varphi^*_c)$, where φ^*_c is a specific nonzero quantity accounting for the enrichment and depletion effects in an overlapped EDL. Our solution in Eq. (4-6) is fundamentally unlike

theirs by distinguishing φ^*_{chm} from φ^*_c. With the introduction of φ^*_{chm} , we improve the understanding of the electric field in an overlapped EDL. Also, our solution is different from theirs in replacement of κ by κ_{eff}. Moreover, one can tell from the format of Eq. (4-6) that the difference between φ and φ_c, instead of the absolute value of φ_c, is the one that really matters to ion distribution. Hence, φ_c will be treated as zero hereafter to compact the expressions.

Based on the resulting electric field, more parameters can be determined. First of all, according to the basic Stern model which has been introduced in Section 3.2, Zeta potential ζ is equal to the electric potential at the OHP, which can be obtained by setting y^* = 1 in Eq. (4-6)

$$\zeta = \frac{2RT}{F}\ln[\mathrm{cd}(n(y^* = 1)|m)] \tag{4-7}$$

Next, the basic Stern model also assumes that surface charge density σ_0 is equal to the total charge density in the diffusive layer in magnitude according to Eq. (3-22). Thus, σ_0 is related to the electric field by the Gauss's law

$$\sigma_0 = -\frac{RT\varepsilon\varepsilon_0}{FH}\frac{\mathrm{d}\varphi^*(y^*=1)}{\mathrm{d}y^*} \tag{4-8}$$

where the dimensionless electric potential gradient normal to the wall is obtained by taking the derivative of Eq. (4-6) with respect to y^*

$$\frac{d\varphi^*}{dy^*} = -\kappa_{eff}H\left(m^{\frac{3}{4}} - m^{-\frac{1}{4}}\right)\frac{\mathrm{sd[n(y^*)|m]}}{\mathrm{cn[n(y^*)|m]}} \tag{4-9}$$

Substituting Eq. (4-9) into Eq. (4-8), σ_0 is expressed in terms of φ^*_{chm} and κ_{eff}

$$\sigma_0 = \left(m^{3/4} - m^{-1/4}\right)\frac{RT\varepsilon\varepsilon_\infty\kappa_{eff}}{F}\frac{\mathrm{sd[n(y^*=1)|m]}}{\mathrm{cn[n(y^*=1)|m]}} \tag{4-10}$$

Finally, combining Eq. (4-6) with Eq. (4-2) and normalizing, ion distribution in the

channel is given by

$$c_{\pm}^{*} = c_{\pm c}^{*}\mathrm{cd}^{\mp 2}(n|m) \tag{4-11}$$

Ion distribution, like the transverse electric field, Zeta potential and surface charge density, is modeled in terms of two independent variables, φ_{chm}^{*} and κ_{eff}. To complete the modeling, two more constraints are needed to determine the values of φ_{chm}^{*} and κ_{eff}.

4.2.3 Approximate Solution

When the channel is sufficiently narrow to have the EDLs strongly overlapped, counterions could be in excess of coions by several orders of magnitude in the entire space including the channel center. Thus, coions have very little contribution to special charge density and can be disregarded. Mathematically, the domination of counterions over coions implies $\varphi_{chm}^{*} = \ln(c_{+c}^{*}/c_{-c}^{*})/2 >> 0$ or $\varphi^{*} + \varphi_{chm}^{*} >> 0$, leading to $\sinh(\varphi^{*} + \varphi_{chm}^{*}) \cong \exp(\varphi^{*} + \varphi_{chm}^{*})/2$. With the omission of coions, Eq. (4-4) is simplified to

$$\frac{d^2\varphi^{*}}{dy^{*2}} = \frac{(\kappa H)^2}{2} c_{+c}^{*} \exp(\varphi^{*}) \tag{4-12}$$

whose analytical solution subjected to the boundary conditions Eq. (4-5) has been proposed in earlier studies [9]. The electric field is related to the concentration of counterions as

$$\varphi^{*} = -2\ln\left[\cos\left(\frac{\kappa H y^{*}\sqrt{c_{+c}^{*}}}{2}\right)\right] \tag{4-13}$$

Using a methodology similar to the derivation for the exact solution, the following relations can be obtained from Eq. (4-13)

$$\zeta = \frac{2RT}{F}\ln\left[\cos\left(\frac{\kappa H\sqrt{c_{+c}^{*}}}{2}\right)\right] \tag{4-14}$$

$$\sigma_0 = -\frac{RT\varepsilon\varepsilon_0\kappa\sqrt{c_{+c}^{*}}}{F}\tan\left(\frac{\kappa H\sqrt{c_{+c}^{*}}}{2}\right) \tag{4-15}$$

$$c_{\pm}^{*} = c_{\pm c}^{*}\cos^{\mp 2}\left(\frac{\kappa Hy^{*}\sqrt{c_{+c}^{*}}}{2}\right) \tag{4-16}$$

Overall, the electric field, surface charge density, and concentration profile of counterion are dependent on only one independent variable c_{+c}^{*}, implying weak coupling comparing to the exaction solution. One can first determine c_{+c}^{*} using one supplemental constraint, and then c_{-}^{*} using the other supplemental constraint.

When applicable, the approximate solution has an advantage over the exact solution because it is more convenient to treat trigonometric functions in calculations than Jacobian elliptic functions. It is also easier to determine unknown priories in the approximate solution with relatively weak coupling. Furthermore, the approximate solution has different application range. When asymmetric electrolyte solution is considered, the approximate solution is acceptable as long as counterions have the same valence, while the exact solution presented above definitely fails. Thus, we still benefit from the approximate solution in spite of the existence of the exact solution.

4.2.4 Determine Unknown Priories

To determine φ_{chm}^{*} and κ_{eff} for the exact solution, or $c_{\pm c}^{*}$ for the approximate solution, two supplemental constraints are needed, including the dissociation equilibrium of water and the chemical equilibrium on surfaces.

H^{+} and OH^{-} are assumed to be in equilibrium with water molecules in the bulk. The addition of surface-dissociated H^{+} shifts the original water equilibrium. If the dissociation

constant is assumed to be the same everywhere [27, 28], the following relations are obtained

$$c_+^* \cdot c_-^* = c_{+c}^* \cdot c_{-c}^* = 1 \tag{4-17}$$

With the use of Eq. (4-17), κ_{eff} is equal to κ even under conditions of EDL overlap, which is always true for salt-free water but questionable for salt solutions. As we discuss in next chapter, the EDL overlap makes κ_{eff} different from κ for electrokinetic flows of salt solution.

The surface chemical equilibrium provides a boundary condition to specify the influence of surface material on the electric field. Three types of surface conditions have been used in the literature: (i) prescribed Zeta potential, (ii) prescribed surface charge density, and (iii) dynamic adsorption-desorption equilibrium on the surface. Zeta potential and surface charge density are not natural properties of surface material. Fundamentally, they depend on the properties of both the surface and the electrolyte solution next to it. In recent studies, the site-binding theorem has drawn more attention since it reflects the chemical nature of the interface and charging process.

In this study, we assume SiOH, SiO^- and $SiOH_2^+$ groups are at chemical equilibrium. According to the two sites model, the surface charge density is expressed as an implicit function of ζ and pH_c via Eq. (3-40), rewritten as

$$\sigma_0 = \frac{F\Gamma_{\text{total}}\delta \sinh[2.3(\text{pH}_z - \text{pH}_c) - \frac{F}{RT}(\frac{\sigma_0}{C} + \zeta)]}{1 + \delta \cosh[2.3(\text{pH}_z - \text{pH}_c) - \frac{F}{RT}(\frac{\sigma_0}{C} + \zeta)]} \tag{4-18}$$

where $pH_c = pH_\infty - \log_{10}(c_{+c}^*)$, ζ and σ_0 are given by Eqs. (4-7) and (4-10) for the exact analytic solution, or Eqs. (4-14) and (4-15) for the approximate solution. We use the two sites model instead of the single site model because the EDL overlap effects might

significantly increases the acidity of salt-free water, making the deprotonation of silanol groups as important as the protonation. Hence, it is better to use the two sites model for modeling surface charge density.

To determine the priories of φ_{chm}^{*} and κ_{eff} in the exact solution, the coupling equations of Eqs. (4-7), (4-10), (4-17) and (4-18) were solved using MATLAB R2009a software package. The priory of c_{+c}^{*} in the approximate solution was determined by solving Eqs. (4-14), (4-15) and (4-18), and then c_{-c}^{*} was obtained from Eq. (4-17). It should be noted that the ion distribution and electric field are self-consistently determined as the derivation uses no information relating to flow conditions. It means that the EDL structure in salt-free water is unchanged no matter what water is in motion or stationary.

4.3 Electrokinetic flow

After the electric potential field and ion distribution are modeled, we turn our attention to the steady-state pressure-driven flow of water in a long slit-like nanochannel. The flow creates a streaming potential field, which pushes counterions against the bulk motion. The bulk velocity under the influence of the streaming potential field is given by [9]

$$u = \frac{H^2}{2\mu} P_x (1 - y^{*2}) - \frac{\varepsilon \varepsilon_0 \zeta}{\mu} E_x \left(1 - \frac{\varphi}{\zeta}\right) \tag{4-19}$$

where P_x = -dP/dx is the pressure gradient, and E_x is the electric field strength caused by the streaming potential. The first term on the RHS represents the contribution of the pressure gradient to the bulk flow, and the second term is the velocity reduction due to the streaming potential. Substituting Eqs. (4-6) and (4-7) into Eq. (4-19) yields

$$u = \frac{H^2}{2\mu} P_x (1 - y^{*2}) + \frac{\varepsilon \varepsilon_0}{\mu} f(y^*) E_x \tag{4-20}$$

where $f(y^*)$ is a function representing the difference between local electric potential and Zeta potential

$$f(y^*) = \varphi - \zeta = -\frac{2k_b T}{e} \ln\left[\frac{\mathrm{cd}(n(y^*=1)|m)}{\mathrm{cd}(n|m)}\right]$$

The transport of ions in the channel is governed by the NP equation. Assuming the flow is fully developed, the concentration gradient along the streamwise direction is negligible. The average ion flux per cross-sectional area is obtained by integrating Eq. (3-3)

$$\langle j_{\pm,x} \rangle = \int_0^1 c_\pm u_\pm \, \mathrm{d}y^* \tag{4-21}$$

where $u_\pm$ is the velocity of H^+ and OH^-

$$u_\pm = u \pm \frac{e}{k_b T} D_\pm E_x \tag{4-22}$$

The streaming potential field exerts an electric force on charged ions, creating additional velocity component besides the bulk velocity. The ionic current density through the channel is given by

$$I = F(\langle j_{+,x} \rangle - \langle j_{-,x} \rangle) \tag{4-23}$$

At steady state, the transport of H^+ and OH^- must be in balance to give

$$I = 0 \tag{4-24}$$

Combining Eqs. (4-21)-(4-24), the streaming potential gradient is related to the pressure gradient as following

$$E_x = \frac{H^2}{2\mu} \frac{\int_0^1 (c_+^* - c_-^*)(1 - y^{*2}) \mathrm{d}y^*}{\int_0^1 [\frac{\varepsilon \varepsilon_0}{\mu}(c_+^* - c_-^*) f(y^*) - \frac{e}{k_b T}(c_+^* D_+ + c_-^* D_-)] \mathrm{d}y^*} P_x \tag{4-25}$$

The streaming potential field always causes additional flow friction, which is called the electroviscous effect. By integrating the bulk velocity distribution in Eq. (4-20) across

the channel, the volume flow rate is given by

$$Q = \frac{2H^3W}{3\mu}P_x - \frac{2HW\varepsilon\varepsilon_0}{\mu}E_x\int_0^1 f(y^*)\,\mathrm{d}y^* \tag{4-26}$$

If setting $E_x = 0$ in Eq. (4-26) to get rid of the influence of the streaming potential field, the obtained flow rate is identical to that of the classical Poiseuille flow between two flat plats. The pressure gradient required to generate the same flow rate Q in the Poiseuille flow is denoted by P_{x0}. Thus, the electroviscous effect can be characterized by the ratio of P_x to P_{x0}, yielding

$$\frac{P_x}{P_{x0}} = 1 + \frac{3\varepsilon\varepsilon_0}{H^2}\frac{E_x}{P_{x0}}\int_0^1 f(y^*)\,\mathrm{d}y^* \tag{4-27}$$

The value of P_x/P_{x0} is always larger than unity, accounting for the increase of flow friction.

4.4 Results and Discussion

Calculations were performed for the approximate and the exact solutions using some common properties. The surface properties used in the calculations are $pH_z = 3.5$, $\Delta pK = 10$, $C = 2.9$ F/ m^2, and $\Lambda = 8.0$ nm^{-2}. Water is assumed at $T = 25$ °C with $D_+ = 9.31 \times 10^{-9}$ m^2/s, $D_- = 5.28 \times 10^{-9}$ m^2/s, $\mu = 0.8904 \times 10^{-3}$ Pa s, $pH_\infty = 7$ and $\varepsilon = 78.2$. The corresponding Debye length κ^{-1} is 1.04 μm. H varies between 0.01 μm and 10 μm to achieve various levels of EDL overlap.

Fig. 4.1 plots the pH profiles, i.e. hydronium ion distribution, across the channel at κH of 0.1,1 and10, as predicted by both the exact and the approximate solutions. The predicted pH maintains at the original value of 7 in the center region of $y^* = 0$~0.4 at $\kappa H = 10$, showing the absence of the EDL overlap in this case. In contrast, the pH at the channel

center decreases to 6.2 and 4.8 at κH = 1 and 0.1, respectively. Such a significant deviation from the original bulk pH signifies the appearance of an overlapped EDL. Regardless of the existence of EDL overlap, the pH increases from near the wall toward the center since hydronium ions are attracted to the negatively charge wall. The figure also shows a good agreement between two analytical solutions for κH = 0.1 and 1, implying that the approximate solution is very accurate under conditions of strong EDL overlap.

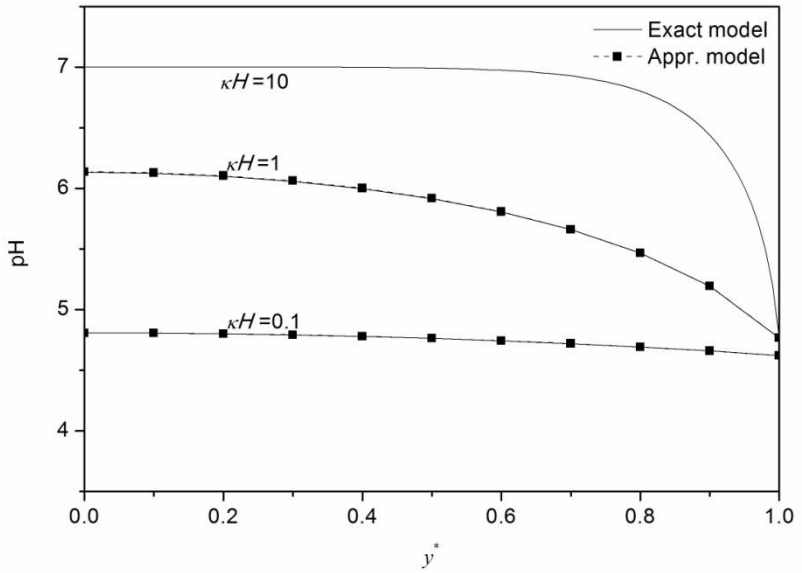

Fig. 4.1. pH profile across the channel at κH = 0.1,1 and 10.

Fig. 4.2 plots profiles of the pH at the channel center pH_c, and the one at the wall pH_0, across the channel for various κH. Both pH profiles are flat for $\kappa H > 4$, and pH_c and pH_0 are almost fixed to 7 and 4.8, respectively. The fixed pH at the channel center and at the wall implies the pH distribution near the walls is independent of channel size, as the opposite EDLs are too far to interact with each other in the corresponding channels. Due the EDL overlap effects, the bulk pH may notably decreases with the decrease of κH or

channel size. An apparent decrease of pH_c occurs at $\kappa H = 4$, indicating the start of EDL overlap. In contrast, the decrease of pH_0 seems delayed, and it appears only in much narrower channels with $\kappa H < 0.2$ as shown in the inset of Fig. 4.2. As a result of the asynchronous pH change, there is less different between pH_c and pH_0 for smaller κH. Hence, the increasing EDL overlap causes hydronium ion distribution more concentrated and more uniform inside the channel.

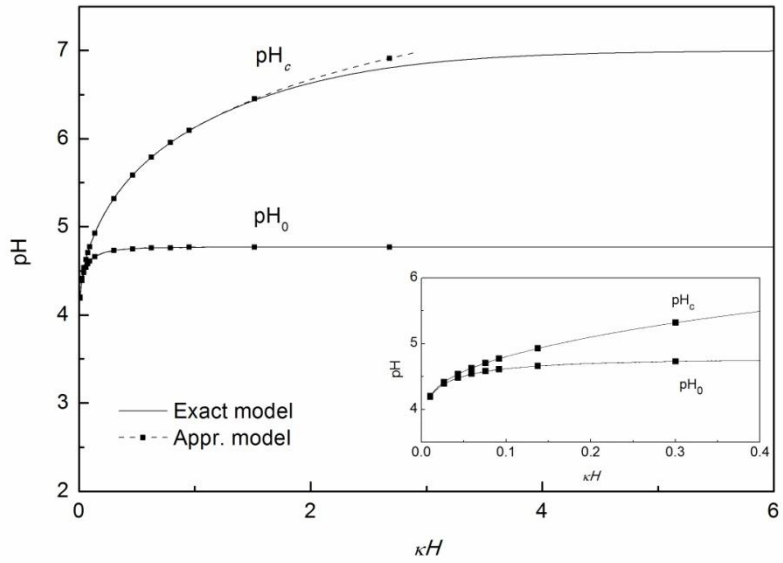

Fig. 4.2. Dependence of the pH at the midplane and at surfaces on EDL overlap

Fig. 4.3 plots the dimensionless electric potential profiles across the channel at κH of 0.1, 1 and 10. The electric potential decreases from the maximum at the wall to zero at the channel center in all three profiles. As discussed earlier, the center potential is not a contributing factor for the electric field and was treated as zero in the calculation. Therefore, the potential should be understood as the potential difference above the center. The figure shows the profile for κH of 10 is almost flat in the center region while the potential

decay is fully completed in a distance of $4\kappa^{-1}$ away from the wall. It suggests that the thickness of the EDL is about $4\kappa^{-1}$, in agreement with the results obtained from Fig. 4.2 that the EDL overlap starts at κH = 4. The profiles for κH of 0.1 and 1 are nearly flat but continuously dropping from the wall, reflecting the flat curving of the corresponding pH profiles in Fig. 4.1.

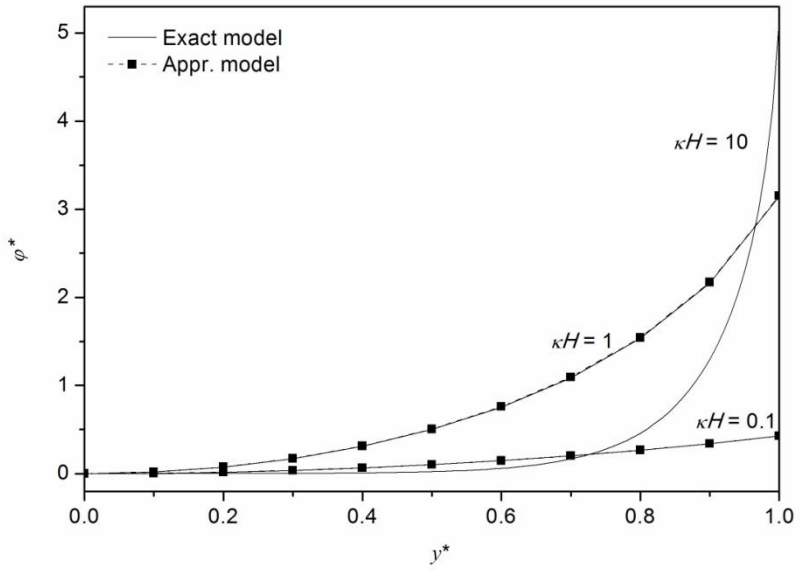

Fig. 4.3. Potential profiles across the channel at κH = 0.1, 1 and 10

Fig. 4.4 shows the influence of EDL overlap on $\varphi^*(y^* = 1)$, Zeta potential in dimensionless form, and φ^*_{chm}, the equivalent electric potential that quantifies the enrichment and depletion effects at the midplane. Fig. 4.5 plots σ_0 as a function of κH. The figures show that all three quantities are independent of κH for $\kappa H > 4$. The independence is due to the absence of EDL overlap again. With the decrease of κH in the κH range of less than 4, there is a remarkable change of the EDL structure. First, Zeta potential decreases in magnitude as shown in Fig. 4.4. Next, the profile of φ^*_{chm} monotonically increases from zero in

Fig. 4.4. φ^*_{chm} is a more accurate indicator for the EDL overlap than the Debye length κ^{-1}, which provides a convenient but rough estimation on the thickness of an EDL. The EDL overlap is regarded as starting in a channel of $H = 5.7\kappa^{-1}$, if we identify the overlap with $\varphi^*_{chm} = 0.01$, or of $H = 4.1\kappa^{-1}$ corresponding to $\varphi^*_{chm} = 0.05$. Finally, surface charge density has a slight decrease within 5% for $\kappa H > 0.5$, and a strong decrease for $\kappa H < 0.5$ as shown in Fig. 4.5.

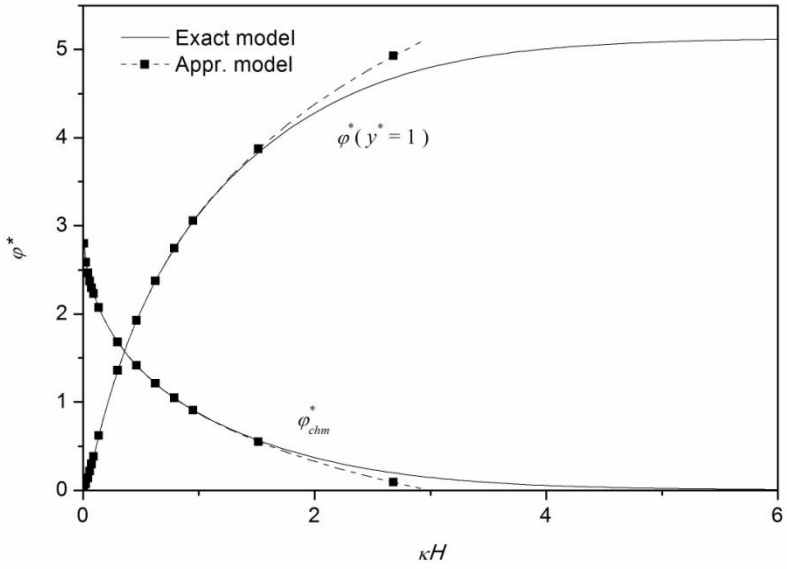

Fig. 4.4. Dependence of $\varphi^*(y^* = 1)$and φ^*_{chm} on EDL overlap

It is of interest to note that Zeta potential decreases as soon as the overlap starts at $\kappa H = 4$, while surface charge density decreases only under conditions of extremely strong EDL overlap at $\kappa H < 0.5$. This phenomenon is in consistence with the synchronous response of pH_c and pH_0 to the EDL overlap as shown in Fig. 4.2. For the κH range of 0.5 ~ 2, the EDL effects is confined in the center region, causing little variation of hydronium ion concentration near the wall. Hence, surface charge density is unchanged as the same

chemical equilibrium remains on the surface. As $\kappa H < 0.5$, hydronium ion concentration at the wall significantly increases under the influence of EDL overlap, effectively shifting the surface equilibrium and reducing surface charge to a much lower level. The results indicate that the prescribing surface charge density method, with applicability for $\kappa H = 0.5\sim2$, has a wider application range than the prescribing Zeta potential method.

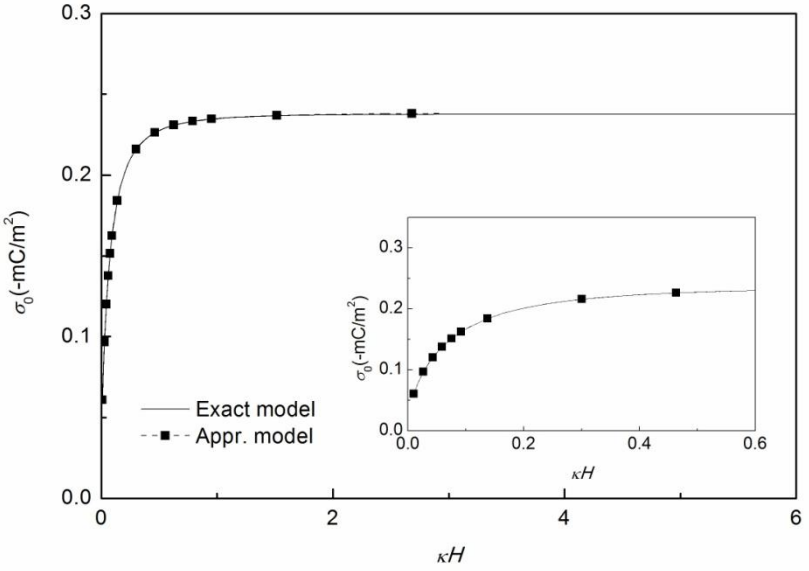

Fig. 4.5. Dependence of surface charge density on EDL overlap

The degree of EDL overlap is classified by the application range of the approximate solution and the prescribing surface charge density or Zeta potential method in Table 4.1. There is no EDL overlap as $\kappa H > 4$. It is reasonable to apply either the prescribed surface charge density or the prescribed Zeta potential in modeling electrokinetic flows. A weak EDL overlap appears for κH between 2 and 4, followed by a strong EDL overlap at $\kappa H < 2$. The comparisons between the exact and approximate model predictions in a series of figures (Fig. 4.2.- Fig. 4.5.) show they are in excellent agreement only for $\kappa H < 2$. Therefore,

the application of the approximate solution is restricted to the EDLs with strong overlap. When the EDLs are extremely overlapped with $\kappa H < 0.5$, the overlap effects extend over the entire diffusive layer, resulting to the unacceptable application of prescribing surface potential or surface charge density as a boundary condition on walls. Nevertheless, the prescribing surface charge density method is still appropriate as long as the EDL overlap is not extremely strong.

Table 4.1. Regimes of EDL overlap

κH	< 0.5	0.5 ~ 2	2 ~ 4	> 4
Approximate Solution	√	√	×	×
Prescribing σ_0	×	√	√	√
Prescribing ζ	×	×	×	√

Fig. 4.6 shows the velocity profiles for hydronium ion, hydroxide ion, and bulk solution as predicted by the exact model at $\kappa H = 1$. The bulk velocity profile of the Poiseuille flow is also plotted for reference. All velocities are normalized using the average velocity of the Poiseuille flow, $U = H^2 P_{x0}/3\mu$. From the figure we can see that there is a slightly deceleration of bulk flow, a notable acceleration of hydroxide ions and a significant deceleration of hydronium ions under the influence of the streaming potential field. At the region near the wall, hydronium ions are moving backward to the upstream with a negative velocity. Hence, not all hydronium ions flow though the channel with the bulk flow as

some of them are circulating inside the channel, similar to transport of potassium ions in electrokinetic flows [42]. In spite of the difference of profiles of hydronium ion and hydroxide ion, their overall fluxes across the channel must be equal according to Eq. (4-23). It is because that hydronium ion is enriched by a few orders of magnitude to compensate for the backward transport near the wall.

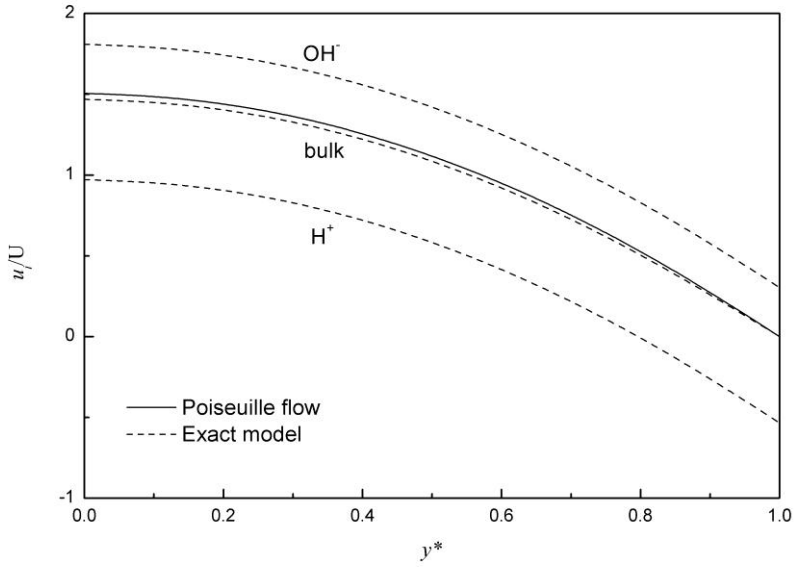

Fig. 4.6. Velocity profiles of bulk flow and ions for $\kappa H = 1$

Fig. 4.7 plots the prediction of P_x/P_{x0} by the exact model for various levels of ELD overlap. There is a peak of 6% in the curve at κH of ~1.3 as shown in the figure. For $\kappa H <$ 1.3, the increasing EDL overlap causes the decrease of the electroviscous effect because the streaming potential for a given pressure gradient is reduced as shown in Fig. 4.8, and because of the less number of hydronium ions in the channel corresponding to a lower surface charge density in Fig. 4.5. As $\kappa H >$ 1.3, the electroviscous effect gradually disappear with the increase of channel height or κH.

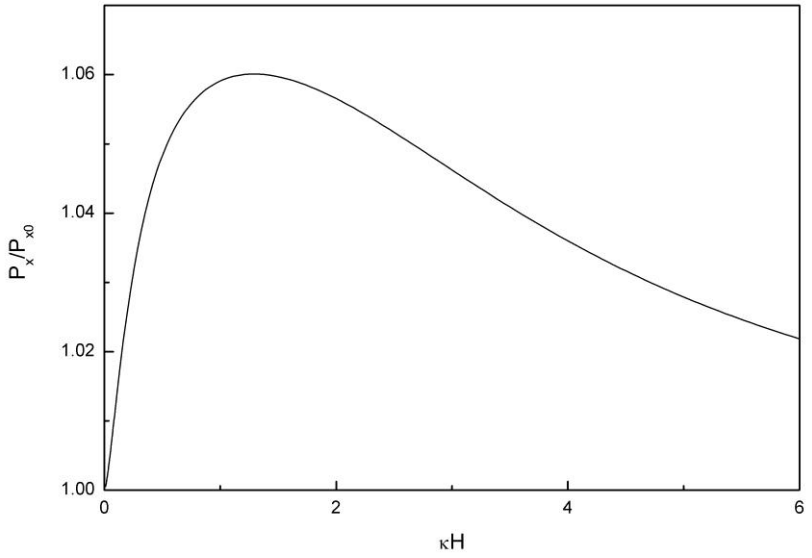

Fig. 4.7. Electroviscous effect for various levels of EDL overlap

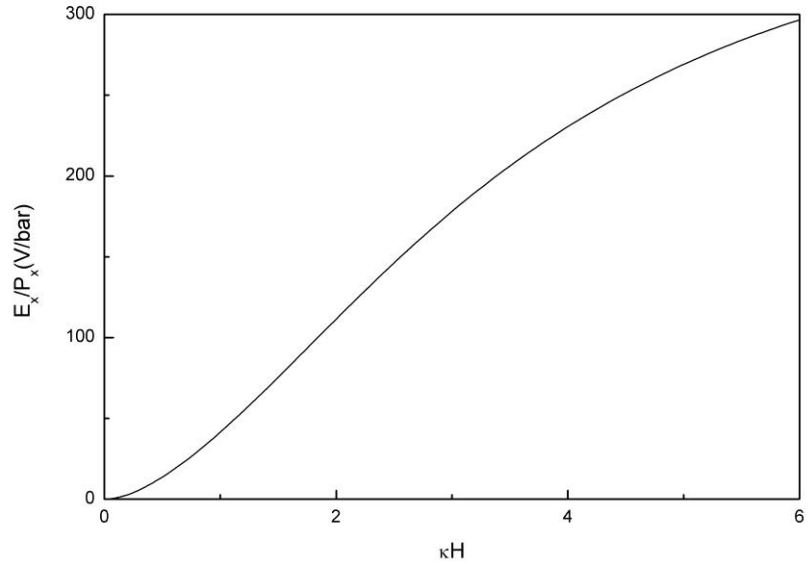

Fig. 4.8. Streaming potential for various levels of EDL overlap

4.5 Conclusion

Using salt-free water in a slit-like silica channel, the effects of the proton transfer between surfaces and the solution on an overlapped EDL were investigated. The ion distribution and electric potential field inside the channel were determined by solving the Poisson and Nernst-Planck equations and by considering chemical equilibrium in water as well as on the walls. Two analytic solutions of the PNP equation were derived not only for water but also for symmetric electrolyte solutions. One is the exact solution in terms of Jacobian elliptic functions, and the other is an approximate solution suitable for strongly overlapped EDLs. The solution methodology can be used for the analysis of dilute solutions within overlapped EDL.

The results show the EDL overlap makes a significant change to the bulk pH, electric potential, and surface charge density. There is an immediate change of the pH at the channel center and the Zeta potential once the EDLs start being overlapped at $\kappa H = 4$, while the surface charge density and the pH at the wall are affected by the EDL overlap at $\kappa H < 0.2$. It suggests that the method of prescribing surface changed density as a boundary condition is appropriate as long as $\kappa H > 0.2$, while prescribing the surface Zeta potential is only appropriate for $\kappa H > 4$. The increase of EDL overlap causes the decrease of the overall solution pH, which inhibits the further release of protons from the surfaces and causes the decrease of surface charge density. There is a good agreement between the exact model and the approximate model in predicting the solution pH at $\kappa H < 2$, which is the regime of EDL overlap to allow the use of the approximate solution for the PNP equation. In the calculations with typical parameters, the maximum electroviscous effect is about 6% as $\kappa H = 1.3$.

CHAPTER 5

FLOWS OF SALT SOLUTIONS IN A NANOCHANNEL

5.1 Introduction

This chapter is to investigate the pH change in electrokinetic flows of dilute solutions as well as its impact on flow dynamics under conditions of EDL overlap. An analytic model is proposed for the fully-developed steady pressure-driven flow of KCl solutions in an infinitely long slit-like nanochannel connected to a reservoir on each end. In this model, the PNP equation is solved for the electric field across the channel with constraints including surface adsorption-desorption equilibrium, water equilibrium, and species flux conservation through the channel. Calculations were carried out for $10^{-3} \sim 10^{2}$ mM KCl solution in nanochannels of 75 nm and 490 nm high, respectively. The results show hydronium ions are more enriched than potassium ions by up to 2~3 orders of magnitude within an overlapped EDL. Hydronium ions may be dominant over potassium ions in the steady flow of very low salt solutions. In comparison with the overlapped EDL at electrostatic equilibrium where hydronium ions and potassium ions are equally enriched, surfaces are significantly less charged, seriously decreasing the electroviscous effect.

5.2. Analytic Model

The electrokinetic flow of binary salt solution in a slit-like nanochannel is modeled in this section. The flow is assumed to be steady-state, fully developed, and driven by a pressure difference between channel ends. The assumption of the steady flow implies that

the bulk flow as well as the transport of all species with the flow is stationary. The channel is not less than 10 nm high to allow the application of the continuum assumption [4], and sufficiently long and wide to make the entrance and sidewall effects negligible. A Cartesian coordinate system is used where the *x*-axis is along the flow direction and the *y*-axis is normal to the channel walls. The height, length and width of the channel are characterized by $2H$, L, and W, respectively. The channel walls are located at $y = \pm H$ while the midplane at $y = 0$. The model is established for KCl solution, but can be applied to other binary salt solutions.

5.2.1 Electric Field and Ion Distribution

A strong transverse electric field, normal to the channel walls, is created by charged surfaces. In electrokinetic flows, the streamwise electric field strength is usually less weaker than the transverse one in the EDL. Therefore, the transverse electric field across the channel is related to ion distribution through the one dimensional Poisson equation, rewriting Eq. (3-19) as

$$\frac{\mathrm{d}}{\mathrm{d}y}\left(\frac{\mathrm{d}\varphi}{\mathrm{d}y}\right) = -\frac{F\sum z_i c_i}{\varepsilon\varepsilon_0}, \tag{5-1}$$

where φ is the electric potential along the transverse direction. Ions contributing to the generation of such an electric field described by Eq. (5-1) include K^+ and Cl^-, which are taken into account in classic analytical models, as well as H^+ and OH^-, which are particularly considered in this model in order to investigate the coupling effects between surface chemical equilibrium and the bulk pH.

In the steady and fully developed flow through a slit-like channel, ion concentrations vary only along the transverse direction. Ion distributions are related to the electric

field by the one dimensional NP equation, whose solution is given by Eq. (3-9) [8], re-written as

$$c_i = c_{i,c}\exp\left(-\frac{z_i F}{RT}\varphi\right) \tag{5-2}$$

where subscript *c* denotes the channel midplane, and the electric potential at the midplane is imposed as zero. It should be noted that surface charges have significant influence on ion distribution within the whole channel under conditions of EDL overlap. Thus, the concentrations of all ions become unknowns at the midplane where the electroneutrality condition is broken. They must be modeled by additional constraints.

Combining Eqs. (5-1) and (5-2) yields the PNP equation expressed in a dimensionless form as

$$\frac{\mathrm{d}^2\varphi^*}{\mathrm{d}y^{*2}} = \left(\kappa_{eff}H\right)^2 \sinh(\varphi^* + \varphi^*_{chm}) \tag{5-3}$$

where $y^* = \frac{y}{H}$, $\varphi^* = -\frac{F\varphi}{RT}$, $\varphi^*_{chm} = \frac{1}{2}\ln\frac{c_{\mathrm{K}^+,\infty}c^*_{\mathrm{K}^+,\mathrm{c}} + c_{\mathrm{H}^+,\infty}c^*_{\mathrm{H}^+,\mathrm{c}}}{c_{\mathrm{Cl}^-,\infty}c^*_{\mathrm{Cl}^-,\mathrm{c}} + c_{\mathrm{OH}^-,\infty}c^*_{\mathrm{OH}^-,\mathrm{c}}}$,

$\kappa^2_{eff} = \kappa^2\frac{\sqrt{\left(c_{\mathrm{K}^+,\infty}c^*_{\mathrm{K}^+,\mathrm{c}} + c_{\mathrm{H}^+,\infty}c^*_{\mathrm{H}^+,\mathrm{c}}\right)\left(c_{\mathrm{Cl}^-,\infty}c^*_{\mathrm{Cl}^-,\mathrm{c}} + c_{\mathrm{OH}^-,\infty}c^*_{\mathrm{OH}^-,\mathrm{c}}\right)}}{c_{\mathrm{K}^+,\infty} + c_{\mathrm{H}^+,\infty}}$, $c^*_{\mathrm{i}} = \frac{c_{\mathrm{i}}}{c_{i,\infty}}$, and

$\kappa^2 = \frac{(c_{\mathrm{K}^+,\infty} + c_{\mathrm{H}^+,\infty} + c_{\mathrm{Cl}^-,\infty} + c_{\mathrm{OH}^-,\infty})F^2}{\varepsilon\varepsilon_0 RT}$.

Superscript * denotes dimensionless quantities, and subscript ∞ denotes where local electroneutrality is not affected by surface charges, such as the reservoirs connected to the channel. κ^{-1}_{eff} is an effective Debye length, and φ^*_{chm} is an equivalent electric potential. They both characterize the impact of the EDL overlap on the electric field.

φ^*_{chm} acts as an additional electric potential to the real electric field. It is actually caused by the enrichment and depletion effects at the midplane. This term will vanish as the

electroneutrality condition is satisfied at the midplane if the EDLs are not overlapped. It was treated as a non-zero real electric potential in previous modeling for an overlapped EDL [5, 6, 19-21].

κ_{eff} is regarded as the change of κ due to the deviation of ion distributions from the Boltzmann distribution. Eq. (5-3) is reduced to the classic PB equation if $\kappa_{eff} = \kappa$, which can be achieved under one of the following conditions: a) No EDLs are overlapped to break the electroneutrality condition at the midplane, so that $c_{i,c} = c_{i,\infty}$; b) Salt solution is in electrostatic equilibrium in the channel and in the reservoirs, so that $c^*_{K^+,c} = c^*_{H^+,c} = 1/c^*_{Cl^-,c} = 1/c^*_{OH^-,c}$, or c) Only salt-free water is contained in the system so that $c_{K^+,\infty} = c_{Cl^-,\infty} = 0$, and $c^*_{H^+,c} = 1/c^*_{OH^-,c}$.

When the Boltzmann distribution is assumed for salt solutions with overlapped EDLs [19], it implies that the modeled EDL structure occurs only at static state with fully-established electrostatic equilibrium. In this study, the electrostatic equilibrium condition is not satisfied, so that the values of both κ_{eff} and φ^*_{chm} must be quantified.

The boundary conditions that Eq. (5-3) is subject to are given by

$$\varphi^*(y^* = 0) = \frac{d\varphi^*(y^*=0)}{dy^*} = 0, \tag{5-4}$$

The solution of Eq. (5-3) subjected to the boundary conditions in Eq. (5-4) is given by [15]

$$\varphi^* = -2\ln[\mathrm{cd}(n|m)] \tag{5-5}$$

where cd is a Jacobian function of argument $n = \kappa_{eff} H y^* \exp(\varphi^*_{chm}/2)/2$, and parameter $m = \exp(-2\varphi^*_{chm})$.

It should be noted that ion distributions and the electrical field described by Eqs.

(5-2) and (5-5) refer to all ion concentrations at the midplane. They can be determined with additional constraints based on other concurrent physical-chemical processes, including surface adsorption-desorption equilibrium, and the species flux conservation, and water dissociation equilibrium, as presented later.

5.2.2. Surface Chemical Equilibriums

The surface adsorption-desorption equilibrium is assumed as the boundary condition on walls for the electric potential field. The two sites model gives the relation of σ_0, pH_c and ζ, so that Eq. (3-40) is rewritten as

$$\sigma_0 = \frac{F\Gamma_{\text{total}}\delta\sinh[2.3(\text{pH}_z-\text{pH}_c)-\frac{F}{RT}(\frac{\sigma_0}{C}+\zeta)]}{1+\delta\cosh[2.3(\text{pH}_z-\text{pH}_c)-\frac{F}{RT}(\frac{\sigma_0}{C}+\zeta)]} \tag{5-6}$$

where $pH_c = pH_\infty - \log_{10}(c^*_{+c})$ is the pH at the midplane, σ_0 is surface charge density, and ζ is the electric potential at the shear layer. Setting $y^* = 1$ in Eq. (5-5) gives rise to

$$\zeta = 2\frac{RT}{F}\ln[\text{cd}(n(y^*=1)|m)] \tag{5-7}$$

σ_0 is given by the Gauss's law

$$\sigma_0 = -\frac{RT\varepsilon\varepsilon_0}{FH}\frac{d\varphi^*(y^*=1)}{dy^*} \tag{5-8}$$

Substituting Eq. (5-5) into Eq. (5-8) yields

$$\sigma_0 = \left(m^{3/4}-m^{-1/4}\right)\frac{RT\varepsilon\varepsilon_\infty\kappa_{eff}}{F}\frac{\text{sd}[n(y^*=1)|m]}{\text{cn}[n(y^*=1)|m]} \tag{5-9}$$

where sd and cn are Jacobian functions.

5.2.3. Water Dissociation

KCl electrolyte is assumed to completely dissolve into free ions, while water dissociation is in equilibrium throughout the salt solution. Thus, the product of hydronium and

hydroxide ion concentration is constant in the entire channel and in the reservoirs, yielding

$$c^*_{\mathrm{H}^+} \cdot c^*_{\mathrm{OH}^-} = c^*_{\mathrm{H}^+,\mathrm{c}} \cdot c^*_{\mathrm{OH}^-,\mathrm{c}} = 1 \tag{5-10}$$

5.2.4. Species Flux Conservation

The present model is established for the steady flow through a channel connecting to a reservoir at each end. When the transport of each species is at steady state, the flux of *i*th species through the channel J_i, is equal to its loss of gain in the upstream or downstream reservoir per unit time Ω_i, according to the species conservation law, yielding

$$J_i = \Omega_i \tag{5-11}$$

The transport of species is composed of chemical groups in which the species is involved. Because KCl electrolytes are completely dissolved, they exist as only free ions in salt solutions. In contrast, water is weakly dissolved based on local equilibrium, and most of H^+ and OH^- are combined as water molecules.

Regardless of the entrance effects, the species flux of K^+ and Cl^- across the channel is given by integrating the streamwise flux density over its cross section

$$J_i = 2HW \int_0^1 c_{\mathrm{i}}\left(u_p + u_e + u_{m,i}\right)\mathrm{d}y^* \quad \text{for } i = \mathrm{K}^+, \mathrm{Cl}^- \tag{5-12}$$

where u_p, u_e and $u_{m,i}$ are three velocity components given by

$$u_{\mathrm{p}} = \frac{H^2}{2\mu} P_x (1 - y^{*2}) \tag{5-13}$$

$$u_{\mathrm{e}} = -\frac{\varepsilon \varepsilon_0 \zeta}{\mu} E_x (1 - \varphi^*) \tag{5-14}$$

$$u_{m,i} = \frac{F z_i D_i}{RT} E_x \tag{5-15}$$

where P_x is the pressure gradient and E_x is the streaming potential gradient. u_p and u_e are the bulk velocities caused by the external pressure gradient and by the induced streaming

potential gradient, respectively. Their combination gives rise to the velocity of the bulk flow, or the velocity component of species accompanying with the bulk flow. $u_{m,i}$ is the electrophoretic velocity accounting for the drift velocity of charged species driven by the streaming potential.

The total flux of H^+ and OH^- is given by

$$J_i = 2HW \int_0^1 c_{\mathrm{i}}\left(u_p + u_e + u_{m,\mathrm{i}}\right) + c_{\mathrm{H_2O}}\left(u_p + u_e\right)\mathrm{d}y^* \quad \text{for } i = \mathrm{H^+}, \mathrm{OH^-} \tag{5-16}$$

where the transport of water molecules accounts for the contribution of the dynamic dissociation equilibrium of water.

The loss of these species in the upstream reservoir or the gain in the downstream reservoir can be determined by considering only the convection of ions. The ion distributions and the electrical field remain uniform in the regions far away from the channel ends. As a result, the diffusive and electrophoretic fluxes of species are negligible, and the convective flux alone is left to account for the loss or the gain of species per unit time, yielding

$$\Omega_i = c_{\mathrm{i},\infty} Q \qquad \text{for } i = \mathrm{K^+}, \mathrm{Cl^-} \tag{5-17}$$

$$\Omega_i = (c_{\mathrm{i},\infty} + c_{\mathrm{H_2O},\infty}) Q \qquad \text{for } i = \mathrm{H^+}, \mathrm{OH^-} \tag{5-18}$$

where Q is the volume rate of the flow leaving the upstream reservoir. According to the mass conservation law, it is equal to the bulk flow rate through the channel

$$Q = 2HW \int_0^1 \left(u_p + u_e\right)\mathrm{d}y^* \tag{5-19}$$

Combining Eqs. (5-11), (5-12), (5-17) and (5-19) gives rise to the species flux conservation equations as

$$\int_0^1 \left[(c_{\mathrm{i}}^* - 1)\left(u_p + u_e\right) + u_{m,\mathrm{i}}\right]\mathrm{d}y^* = 0 \qquad \text{for } i = \mathrm{K^+}, \mathrm{Cl^-} \tag{5-20}$$

The equation has been proposed in a previous model for electrokinetic flows through a uniform slit [43].

Similarly, Eqs. (5-10), (5-11), (5-16), (5-18), and (5-19) are combined to give the constraint for the transport of H^+

$$\int_0^1 \left[\left(c^*_{\mathrm{H^+}} - 1 \right) \left(1 + \frac{c_{\mathrm{OH^-},\infty}}{c_{\mathrm{H^+},\infty} c^*_{\mathrm{H^+}}} \right) \left(u_p + u_e \right) + c^*_{\mathrm{H^+}} u_{m,\mathrm{H^+}} - \frac{c_{\mathrm{OH^-},\infty}}{c_{\mathrm{H^+},\infty} c^*_{\mathrm{H^+}}} u_{m,\mathrm{OH^-}} \right] \mathrm{d}y^* = 0 \quad (5\text{-}21)$$

In most of previous studies on electrokinetic flows, ionic current through the channel is assumed to be zero, which is called the current equilibrium condition. Such a condition is in insistence with the species flux conservation. By combining Eqs. (5-11), (5-17) and (5-18), the ionic current is given by

$$F(J_{\mathrm{K^+}} + J_{\mathrm{H^+}} - J_{\mathrm{Cl^-}} - J_{\mathrm{OH^-}}) = \left(c_{\mathrm{K^+},\infty} - c_{\mathrm{Cl^-},\infty} + c_{\mathrm{H^+},\infty} - c_{\mathrm{OH^-},\infty} \right) FQ \quad (5\text{-}22)$$

Applying the electroneutrality condition in the reservoirs, i.e. $c_{\mathrm{K^+},\infty} - c_{\mathrm{Cl^-},\infty} + c_{\mathrm{H^+},\infty} - c_{\mathrm{OH^-},\infty} = 0$, Eq. (5-22) is reduced to the current equilibrium condition,

$$J_{\mathrm{K^+}} + J_{\mathrm{H^+}} - J_{\mathrm{Cl^-}} - J_{\mathrm{OH^-}} = 0 \quad (5\text{-}23)$$

As a summary of the above discussion, five constraints are imposed to determine five independent quantities of $c^*_{\mathrm{H^+},c}$, $c^*_{\mathrm{OH^-},c}$, $c^*_{\mathrm{K^+},c}$, $c^*_{\mathrm{Cl^-},c}$ and E_x, and two other dependent parameters of φ^*_{chm} and κ_{eff}. The constraints include surface chemical equilibrium described by Eqs. (5-6), (5-7) and (5-9), water dissociation equilibrium by Eq. (5-10), and the flux conservation of K^+, Cl^- and H^+ by Eqs. (5-20) and (5-21). These equations were solved through multiple iterations using MATLAB R2009a. We first solved for φ^*_{chm}. φ^*_{chm} An appropriate guess of φ^*_{chm} is initially given, and then a calculated φ^*_{chm} is obtained by the following iterative procedure:

1) Give an initial guess for $c^*_{H^+,c}$,
2) Obtain κ_{eff} by solving the coupled equations Eqs. (5-6), (5-7), and (5-9),
3) Solve for $c^*_{OH^-,c}$, $c^*_{K^+,c}$, $c^*_{Cl^-,c}$ and E_x in sequence. $c^*_{OH^-,c}$ is obtained from Eq. (5-10), $c^*_{K^+,c}$ and $c^*_{Cl^-,c}$ from the guessed φ^*_{chm} and the calculated κ_{eff}, and E_x from the flux conservation of K^+ by Eq. (5-20).
4) Obtain $c^*_{H^+,c}$ from Eq. (5-21).
5) Repeat step 1) - 4) until the calculated $c^*_{H^+,c}$ matches its initial guess
6) Obtain φ^*_{chm} from the flux conservation of Cl^- by Eq. (5-20).

The value of φ^*_{chm} is determined if the calculated one matches its initial guess, otherwise, it is set as the initial guess for next iteration. Other independent quantities are then determined by repeating step 1) - 4) with the calculated φ^*_{chm}.

An approximate solution of the PNP equation is used to replace Eq. (5-5) in the calculations for κH > ~15 because the above algorithm failed to converge in cases of high salt solutions. With κH > ~15, the enrichment and depletion effect at the midplane is almost negligible, so that φ^*_{chm} falls to below machine epsilon. Thus, the computation of Eqs. (5-7) and (5-9) leads to an enormous computation error. In this case, φ^*_{chm} can be simply imposed as zero due to the electroneutrality condition at the midplane. An approximate solution of Eq. (5-3) subjected to Eq. (5-4) is given by [9, 17]

$$\varphi^* = 4\tanh^{-1}\left[\tanh\left(\frac{\varphi^*(y^*=1)}{4}\right)\exp\left(-\kappa_{eff}H(1-y^*)\right)\right] \tag{5-24}$$

Substituting Eq. (5-24) into Eq. (5-8) yields

$$\sigma_0 = -\sqrt{2}\varepsilon\varepsilon_0\kappa_{eff}RTF^{-1}\sqrt{\cosh[\varphi^*(y^*=1)]-1} \tag{5-25}$$

Eqs. (5-10), (5-20), (5-21), (5-24) and (5-25) are solved in the similar iterative procedure as used for deriving the exact solution. The results from the exact and approximate solutions are perfectly matched for $\kappa H > 10$, which validates the present model.

5.4. Results and Discussion

The calculations use the parameters from previous experiments which investigated the pressure driven flow in a nanochannel [6]. The channel geometry is set as W of 50 μm, L of 4.5 mm, and $2H$ of 75 nm and 490 nm. The solution properties are given at T = 25 °C, including $D_{K^+} = 1.96 \times 10^{-9}$ m^2/s , $D_{Cl^-} = 2.03 \times 10^{-9}$ m^2/s, $D_{H^+} = 9.31 \times 10^{-9}$ m^2/s, $D_{OH^-} = 5.28 \times 10^{-9}$ m^2/s, $\mu = 0.8904 \times 10^{-3}$ Pa s . If no extra acid or alkaline is added to change the pH of salt solutions, $c_{H^+,\infty} = c_{OH^-,\infty} = 10^{-4}$ mM. KCl solutions vary from 10^{-3} mM to 10^{2} mM. Surface parameters are $\Lambda = 8.0$ nm^{-2}, $C = 0.3$ F/ m^2, ΔpK = 8.4, and pH$_z$ = 3.5 . They are chosen in an appropriate range for silica surfaces [16, 19, 27] to make the model predictions in good agreement with the experimental data of the 75 nm channel in high salt solutions.

To examine the impact of the proton exchange on the EDL structure at the steady flow state, the predictions of the present model are compared with the traditional model [19]. The latter model assumes the Boltzmann distribution and neglects hydronium and hydroxide ions in the calculation of spatial charge density. In fact, it can be reduced from the present model through the following simplifications: (i) $c_{H^+,\infty} = c_{OH^-,\infty} = 0$ and $\kappa_{eff} = \kappa$ in Eq. (5-3), (ii) $c_{H^+,c} = c_{H^+,\infty}\exp(\varphi^*_{chm})$ to give pH$_c$ in Eq. (3-40), (iii) remove Eq. (5-10), and

(iv) replace Eq. (5-20) and (5-21) with the current equilibrium condition of $J_{K^+} - J_{Cl^-} = 0$. It should be kept in mind that the Boltzmann distribution is valid only at electrostatic equilibrium in cases of the EDL overlap. Hence, the EDL structure predicted by the traditional model is suitable for static salt solutions, while the present model for the steady state flow.

5.4.1 EDL Structure

Fig. 5.1 plots transverse electric potential and concentration profiles along the cross section for 0.01 mM KCl solution in the 75 nm channel with the corresponding κH of 0.4. The concentration profile of OH^- is not shown as $c^*_{OH^-}$ is simply the reciprocal of $c^*_{H^+}$. The electric potential increases in magnitude from the channel midplane(at $y^* = 0$) to the wall(at $y^* = 1$), while c_{K^+} increases and c_{Cl^-} decreases. A significant variation of electric potential and ion concentrations across the whole channel is a feature of the EDL overlap.

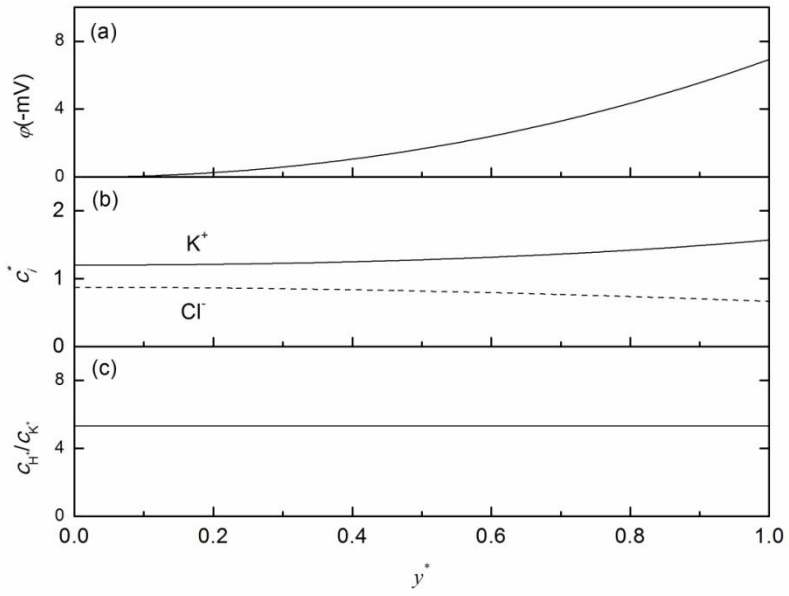

Fig. 5.1. Profiles of a)φ, b) $c^*_{K^+}$ and $c^*_{Cl^-}$, and c) c_{H^+}/c_{K^+} along the cross section for 0.01 mM KCl in the 75 nm channel

Fig. 5.1c demonstrates that the concentration of H^+ becomes a few times as much as that of K^+ across the channel, in spite of the fact that the former is only 1% of the latter in the original salt solution or in the reservoirs. It implies that the enrichment of H^+ is hundreds times stronger than that of K^+ comparing to their original concentration. The dominant enrichment of H^+ over K^+ has profound effects on the EDL structure and electrokinetic flows. It is also shown that the ratio of concentration of H^+ to K^+ is the same across the channel. The reason is that ions with equal valence must be proportionally affected by the electric field according to Eq. (5-2). Hence, the comparison of ion concentrations at the midplane reflects their difference across the whole channel.

Fig. 5.2 plots the prediction of φ^*_{chm} as a function of κH, and provides a convenient conversion between salt concentration and κH for two studied channels. φ^*_{chm} is a quantity that reflects the enrichment of all counterions as well as the depletion effects of all coions at the midplane. Like κH, φ^*_{chm} is a direct measure of the degree of the EDL overlap since the presence of the overlap is literally understood as the variation at the midplane. If 0.001 is referred to as the critical value of φ^*_{chm}, above which the EDLs are overlapped, the critical κH is 7.5 or so for both channels, corresponding to salt solutions of 3.5 mM in the 75 nm channel and of 0.1 mM in the 490 nm one as shown in Fig. 5.2. For a specific nanochannel, stronger EDL overlap exists in lower salt solutions with larger φ^*_{chm} and smaller κH.

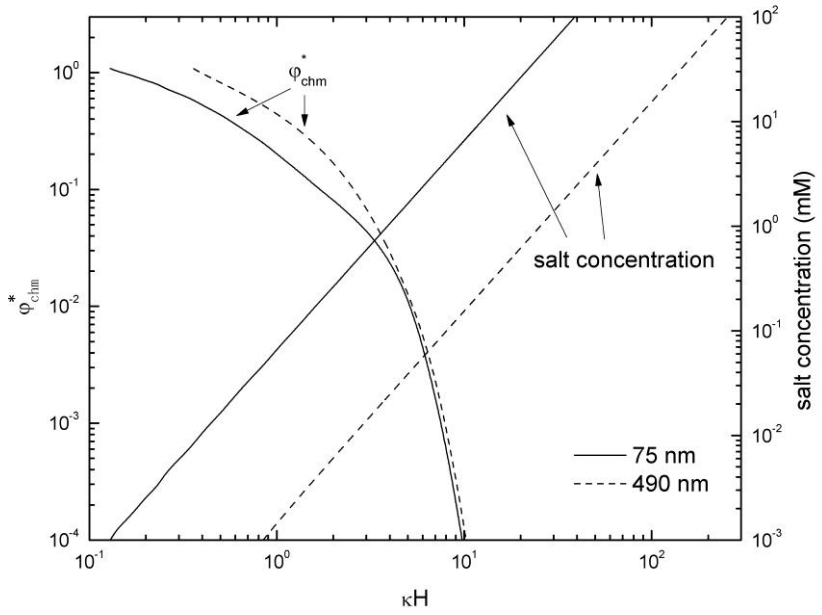

Fig. 5.2. Relation of φ^*_{chm}, κH and salt concentration.

Fig. 5.3 compares the predictions of two models in the enrichment and depletion effects at the midplane. In high salt solutions with $\kappa H > 10$ where the EDL overlap is obviously absent since φ^*_{chm} is as small as less than 0.001, both models predict all $c^*_{i,c}$ are nearly of unity. The agreement between the model predictions suggests that the Boltzmann distribution is an appropriate description for $\kappa H > 10$, and that the omission of H^+ in the calculation of spatial charge density is reasonable because H^+ is negligible in numbers comparing with K^+ across the channel. In low salt solutions with $\kappa H < 10$, strong dependence of $c^*_{i,c}$ on salt concentration or κH are predicted by both models, but the dependence is in a deferent way.

The present model predicts unequal enrichment of K^+ and H^+ in an overlapped EDL. The concentrations of K^+ and Cl^- at the midplane are almost as much as their original concentrations, while H^+ is radically enriched. It is surprising that $c^*_{K^+,c}$ is not always larger

than 1 as shown in Fig. 5.3b, implying that K^+ is even depleted at the midplane somehow despite the overall enrichment across the channel. The curves of $c^*_{H^+,c}$ dramatically rise up with the decrease of salt concentration in weakly overlapped EDLs with $2 < \kappa H < 10$, and become nearly flat in strongly overlapped EDLs with $\kappa H < \sim 2$, as shown in Fig. 5.3a. The plateau behavior occurs because salt solutions are extremely diluted to be almost salt-free water. For instance, the values of $c^*_{H^+,c}$ in 0.001 mM solution are within 0.5% difference away from those for salt-free water in the two studied channels. As a consequence of un-equal enrichment, H^+ becomes the leading contributor to spatial charge density in a strong overlapped EDL as its concentration is comparable to or a few orders of magnitude larger than that of K^+ when $\kappa H > 2$.

The traditional model suggests that K^+ and H^+ are always equally enriched at the midplane in an overlapped EDL such as $c^*_{K^+,c} = c^*_{H^+,c}$, and that the stronger overlap leads to the greater enrichment. Because K^+ is more than H^+ by a few orders of magnitude in the reservoirs, such a domination extends to the space inside the channel. Therefore, it is K^+, instead of H^+ as predicted by the present model, that carry most of spatial charges in an overlapped EDL.

The discrepancy between the predictions is not too surprising because the primary mechanisms of ion transport are completely different in these two models. Diffusion and electromigration are balanced to affect ion distributions at electrostatic equilibrium. In electrokinetic flows, however, the species transport along the streamwise direction is governed mainly by convection and electromigration. When a sudden pressure difference starts the flow, the streaming potential is immediately induced to push all counterions

against the fluid motion. Because the mobility of H^+ is about 4 times larger than that of K^+, it is harder for the bulk flow to carry H^+ downstream, leading to the consistent accumulation of H^+ inside the channel until the steady state is achieved.

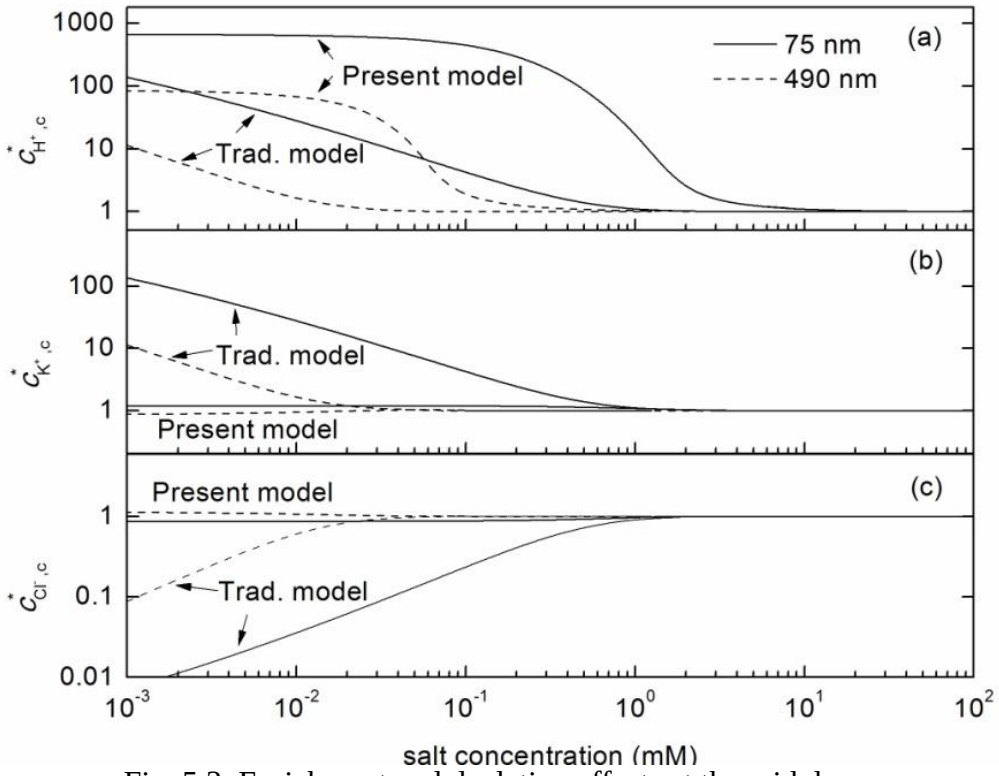

Fig. 5.3. Enrichment and depletion effects at the midplane

The phenomenon of unequal enrichment is related to the mobility of salt counterions. Fig. 5.4 compares the enrichment and depletion effects at the midplane of the 75 nm channel for salt solutions with various mobility of 0.11, 0.21, 0.5, 0.8 and 1 times as large as D_{H^+}. $0.11D_{H^+}$ and $0.21D_{H^+}$ are equal to the mobility of Li^+ and K^+, respectively. The other values belong to no real salt counterions, but are chosen to illustrate the influence of relatively large mobility of salt counterions on the EDL structure. With the increase of mobility of salt counterions, hydronium ions are less enriched as shown in Fig. 5.4a, while

salt counterions are more enriched Fig. 5.4b. When the mobility of salt counterion is sufficiently large, such as being equal to D_{H^+}, salt counterion, instead of H^+, is the one that becomes more enriched.

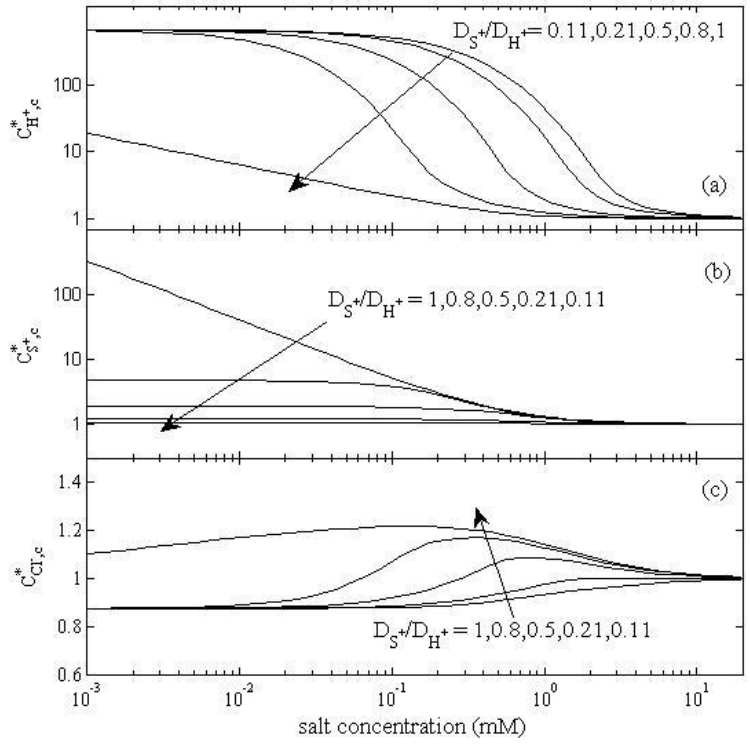

Fig. 5.4. Impact of mobility of salt counterion on the enrichment and depletion effects at the midplane in the 75 nm channel

Surface charge density plays a critical role to quantifying the EDL structure. Net surface charge is equal to the amount of charges carried by all ions along the cross section in magnitude in a long channel, no matter whether fluid is in motion or not. On the other hand, it reflects the magnitude of surface proton activity via the association-dissociation equilibrium of silanol groups. The stronger proton activity make surfaces less charged.

Fig. 5.5 demonstrates that the predictions of surface charge density by two models

are well matched for high salt solutions, similar to the agreement of ion concentrations at the midplane. It implies that ion distributions are identical at electrostatic equilibrium and in the steady flow if the EDLs are not overlapped. Such a non-overlapped EDL has been well understood in past studies. Thus, later discussions are focused on low salt solutions to investigate the structure of an EDL with various overlap.

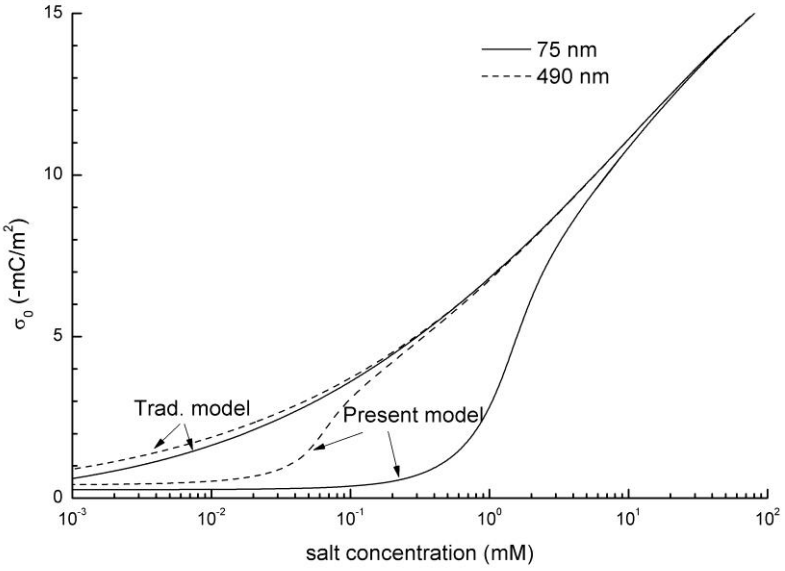

Fig. 5.5. Comparison of the present model and the traditional model in surface charge density

The present model predicts that surfaces are less charged in lower salt solutions with $2 < \kappa H < 10$ and nearly equally charged for $\kappa H < \sim 2$ as shown in Fig. 5.5. Surface charge density predicted by the present model is merely 10~30% of the prediction of the traditional model. The dependence of surface charge density on the EDL overlap, and the discrepancy between two models' predictions are in accordance with the enrichment of H^+ at the midplane as shown in Fig. 5.3b. The stronger enrichment of H^+ shifts surface equilibrium to allow surfaces less charged.

The above discussions lead to a few conclusions about the structure of an overlapped EDL. First, it is strongly dependent on the flow status. An overlapped EDL at the steady flow state is featured by strong enrichment of H^+, weak enrichment of K^+, low surface charge density, and less spatial charges along the cross section, in contrast to those at electrostatic equilibrium. Provided that the steady flow is approaching static state after suddenly turning off the pressure supply, the EDL structure changes when shifting to the new equilibrium in several aspects: a) surfaces release protons so as to be more negatively charged, b) H^+ diffuse out of the channel, c) K^+ are attracted into the channel from the reservoirs, and d) the overall concentration of counterions increases. Therefore, the Boltzmann distribution which describes ion distributions at electrostatic equilibrium is not suitable for the steady flow. Second, H^+ has a considerable contribution to spatial charge in the EDL at the steady flow state. The mechanisms relating to H^+ play an important role to modeling an overlapped EDL. Finally, the EDL structure significantly varies with salt concentration in a weakly overlapped EDL with $2 < \kappa H < 10$, but has little change in a strong overlapped EDL with $\kappa H < \sim 2$. The reason is that H^+ is overwhelming in numbers in extremely low salt solutions. As a result, the slight change of the concentration of K^+ has no significant impact on the EDL structure.

5.4.2 Effects of pH_∞

The EDL structure is likely dependent on the pH of the original salt solution, pH_∞, which affects surface adsorption-desorption equilibriums via surface proton activity. It is well known that adjusting pH_∞ makes the surfaces differently charged, but the experience is mostly based on the Boltzmann equilibrium. It is important to understand whether and

how pH_∞ affects the structure of an overlapped EDL at the steady flow state where the Boltzmann equilibrium is not applicable.

Fig. 5.6 and Fig. 5.7 compare two models in the predictions of the pH at the midplane pH_c, and surface charge density σ_0, respectively, for KCl solutions in the 75 nm channel with various pH_∞ of 6, 7, and 8. The value of pH_∞ is controlled by adding HCl or KOH into original salt solutions. so that no other ions are involved. As a result, either Cl^- or H^+ slightly increases, and the concentration of salt solutions is defined as the minimum of two salt ions. The traditional model shows that both pH_c and the magnitude of σ_0 greatly increase by a larger pH_∞. The results are in accordance with the previous experience.

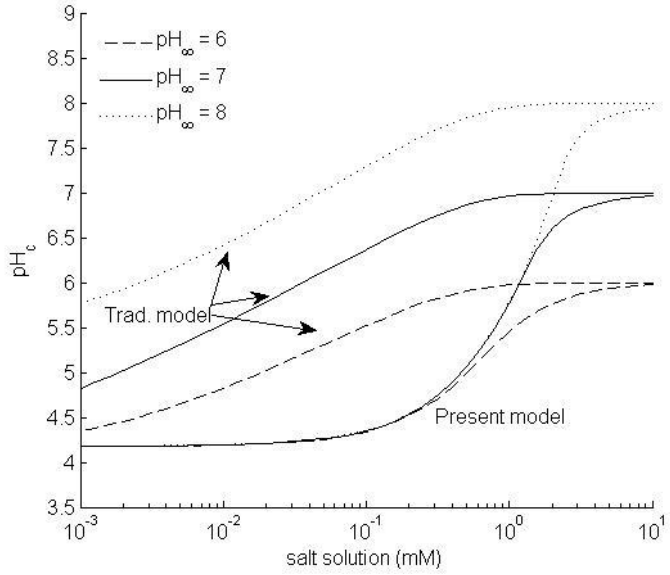

Fig. 5.6. Effects of pH_∞ on pH_c in the 75 nm channel

The present model suggests that the EDL structure is strongly dependent on pH_∞ if the EDLs are not overlapped or weakly overlapped, but becomes independent when the

EDLs are strongly overlapped in low salt solutions. In a non-overlapped EDL, there is no enrichment at the midplane so that pH_c is equal to pH_∞. Any adjustment of pH_∞ is fully transferred into the EDL, exerting the most significant effects on the EDL structure. When the EDLs are overlapped, the pH change in the reservoirs is merely partially transferred into the channel, as the enrichment of H^+ buffers the pH change in the channel. With the increase of the EDL overlap, the stronger enrichment of H^+ makes the pH in the channel less sensitive to the change of pH_∞. In extremely dilute salt solutions with $\kappa H < \sim 2$, the change of pH_∞ has no impact on the EDL structure.

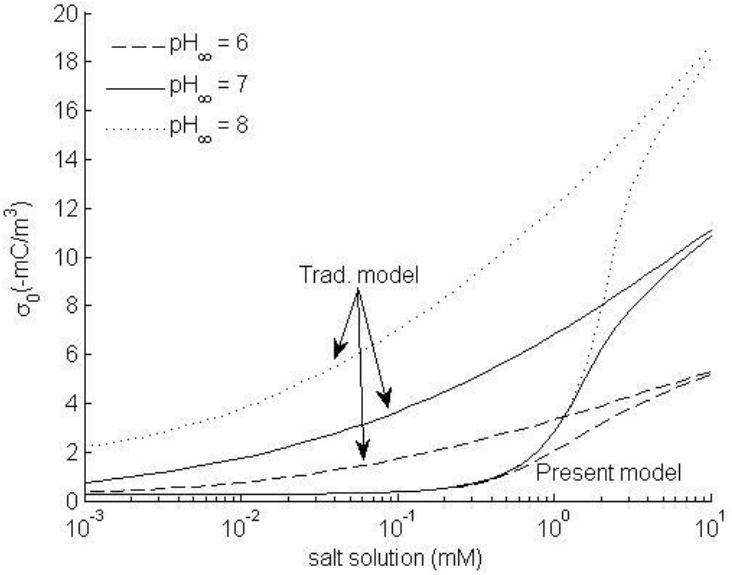

Fig. 5.7. Effects of pH_∞ on σ_0 in the 75 nm channel

5.4.3 Streaming Conductance and Electrical Conductance

The streaming conductance and the electrical conductance of a channel were investigated by measuring the voltage on various external resistors [6]. The streaming conductance is defined as

$$G_{\mathrm{str}} = \frac{2HWF}{P_x L} \int_0^1 u_{\mathrm{p}} \sum z_i c_i \, \mathrm{d}y^* \tag{5-26}$$

which identifies the capability of a nanochannel to allow the transport of spatial charges with the bulk flow. The electrical conductance is defined as

$$G_{\mathrm{elec}} = \frac{2HWF}{E_x L} \int_0^1 \sum \left(u_{\mathrm{e}} + u_{m,i}\right) z_i c_i \, \mathrm{d}y^* \tag{5-27}$$

which measures the capability of a nanochannel to create a conduction current due to the electrophoretic transport of spatial charges. For a specific channel, G_{str} is dependent on local spatial charge density, while G_{elec} is related to ion distributions and ion motilities. They both are measurable variables through which it is possible to experimentally investigate the EDL structure.

Fig. 5.8 compares the predictions of the present and traditional models against experimental data [6] for streaming conductance. The predictions agree well with experimental data in high salt solutions, partially because surface parameters are deliberately chosen in modeling. In low salt solutions, the predictions of the traditional model are in agreement with experimental results, while the present model predicts only about 10% and 30% of the measured values for the 75 nm and 490 nm channel, respectively. However, it was also observed in the experiments that streaming conductance was very low(<0.5 pA/bar) for hours upon initially filling the 75 nm channels with low salt solutions before it crept up to the stable values. Such a low streaming conductance is close to the predictions of the present model.

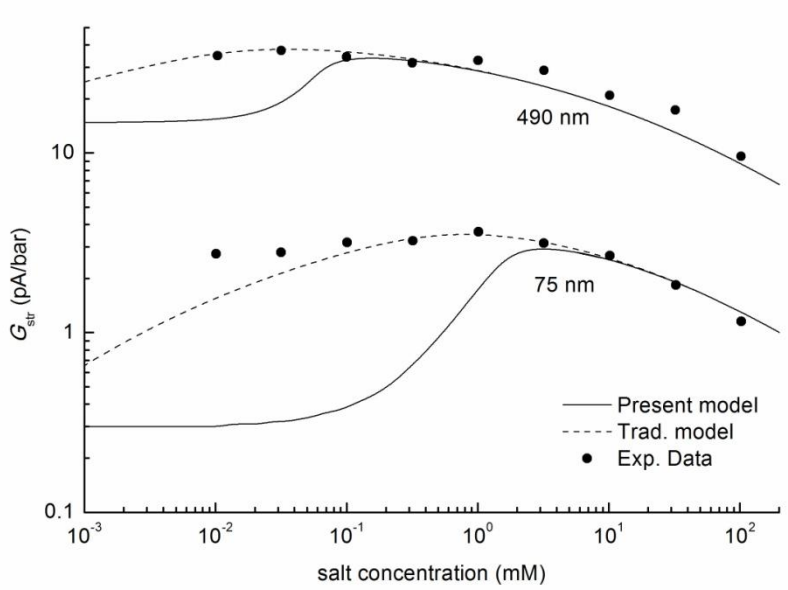

Fig. 5.8. Comparison of the present model, the traditional model and experimental data [6] in the streaming conductance

The initial low streaming conductance is likely caused by strong enrichment of H^+ after initial filling. It was reported that the bulk pH dropped to pH_z in nearly half length of the nanochannel due to the release of protons from silica surfaces during the capillary filling process [33]. If this phenomenon occurred in the studied experiments, the initial EDLs tended to have features like those in the steady flow, including low surface charge density or less counterions across the channel. It explains why the initial streaming conductance is better predicted by the present model, instead of the traditional one.

The better agreement of the traditional model predictions and experimental data in low salt solutions, suggests that the EDL structures were more like the ones at static state when the data were collected a few hours after filling. Approaching electrostatic equilibrium after initial filling is a process similar to the shifting of the EDL structure from the steady state to the static state. The concentration of counterions continuously increases

during the process, leading to an increasing streaming conductance. Nevertheless, the transient may process as long as a few hours, because transport of ions are dominated by the diffusion with time scale of L^2/D_i estimated as a few hours.

The discrepancy between the predictions and experimental data in Fig. 5.8 is likely resulted from the failure to achieve the steady flow in experiments. According to numerical simulation results discussed in next chapter, a few hours may be needed to obtain the steady flow under experimental conditions. Had the pressure supply been intermittently applied with the duration of a few minutes, the EDL structure in the channel would have been closer to electrostatic equilibrium.

The electrical conductance is slightly associated with the type of salt solutions at the steady flow in an overlapped EDL. The electrical conductance is proportional to the mobility of countions. As discussed earlier, salt counterions are dominant at electrostatic equilibrium, causing the strong dependence of G_{elec} on the type of salt solutions. For instance, the replacement of KCl with LiCl may decrease G_{elec} by a factor of 2 due to the great difference of the mobility of $K^+$and Li^+. However, the majority of counterions in the steady flow is hydronium ions whose mobility is commonly a few times larger than other salt ions. As a consequence, G_{elec} is insensitive to the mobility of salt ions.

Fig. 5.9 compares the predictions of two models against and experimental studies [6] for the channel electrical conductance. In consistence with low counterions in an overlapped EDL at the steady flow state, the electrical conductance is generally lower comparing to the EDL at electrostatic equilibrium, but gets closer in extremely low salt solutions. The reason is that H^+, with higher mobility, takes the place of K^+ to be the dominating counterion.

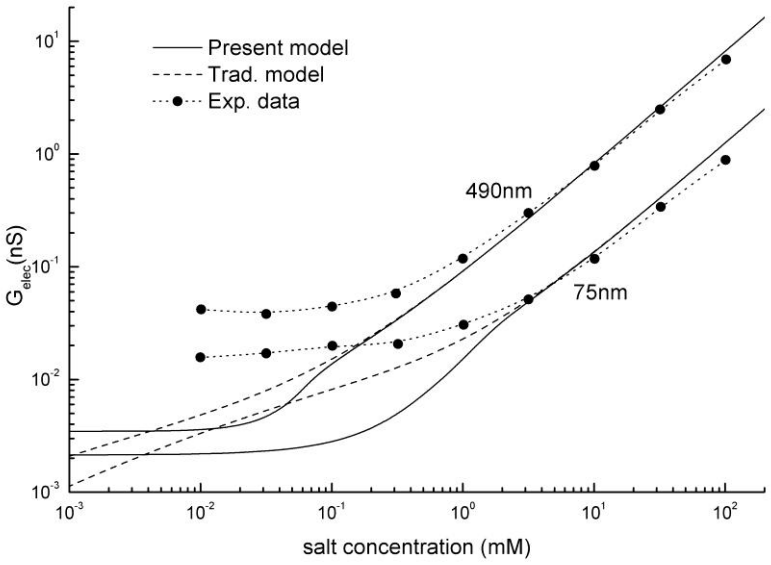

Fig. 5.9. Comparison of the present model, the traditional model and experimental data [6] in the channel conductance

However, both models underestimate the electrical conductance comparing to experimental data. There must be reasons other than the addition of surface-dissociated hydronium ions to account for the unpredicted electrical conductance. A possible reason is to consider the conductance in the Stern layer where protons are assumed to mobile and other counterions immobile [6].

5.4.5 Electroviscous Effect

The flow through a nanochannel induces a streamwise potential difference, called the streaming potential, which exerts a force on charged ions and produces a backflow of fluid. The flow shows an increased apparent viscous drag with respect to the Poiseuille flow. This phenomenon is called the electroviscous effect.

For electrokinetic flows at steady state, the streaming potential gradient is related to

the pressure gradient by combing Eqs. (5-23), (5-26) and (5-27), yielding

$$E_x = -\frac{G_{str}}{G_{elec}} P_x \tag{5-28}$$

Substituting Eqs. (5-5), (5-13) and (5-14) into Eq. (5-19) yields

$$Q = F_p P_x + F_e E_x \tag{5-29}$$

where $F_p = \frac{2H^3 W}{3\mu}$ and $F_e = -\frac{4WH\varepsilon RT}{\mu F}\int_0^1 \ln\frac{\mathrm{cd}(n(y^*=1)|m)}{\mathrm{cd}(n|m)}\mathrm{d}y^*$. The first term of RHS of Eq. (5-29) accounts for the fluid transport due to the pressure gradient, while the second term for the change of the flow rate due to the electroviscous effect.

Substituting Eq. (5-28) into Eq. (5-29) yields

$$P_x = Q\left(F_p - \frac{G_{str}}{G_{elec}} F_e\right)^{-1} \tag{5-30}$$

Regardless of the electroviscous effect, imposing $E_x = 0$ in Eq. (5-29) gives rise to

$$P_{x0} = \frac{Q}{F_p} \tag{5-31}$$

where P_{x0} denotes the pressure gradient required for the Poiseuille flow to deliver the fluid at the flow rate of Q.

The electroviscous effect can be quantified by P_x/P_{x0}, which is always larger than unity. The larger the value of P_x/P_{x0}, the greater the electroviscous effect. Combining Eq. (5-31) and Eq. (5-30) gives

$$\frac{P_x}{P_{x0}} = \left(1 - \frac{F_e}{F_p}\frac{G_{str}}{G_{elec}}\right)^{-1} \tag{5-32}$$

Fig. 5.10 compares the predictions of two models in P_x/P_{x0}. The curves from the present model present a peak value at κH = ~6 where the EDLs are barely overlapped, significantly drop with the increase of the EDL overlap in low salt solutions with κH = 2~6,

and become almost flat in extremely low salt solutions with $\kappa H < \sim 2$. It is noteworthy that the electroviscous effect predicted by the present model is only 5~30% as much as that of the tradition model. The weaker electroviscous effect is in consistence with the lower surface charge density as discussed earlier.

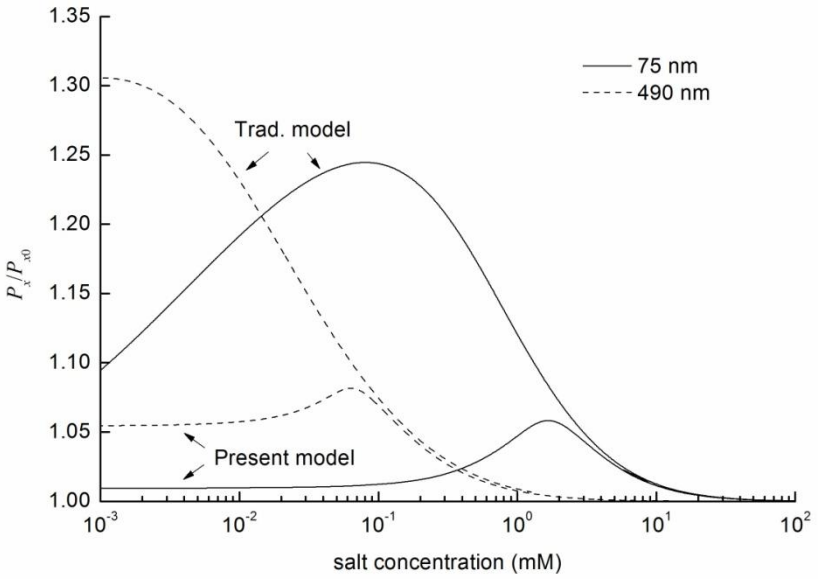

Fig. 5.10. Electroviscous effect

5.5. Conclusions

The steady state pressure driven flow in a nanochannel has been modeled with the consideration of hydronium ions in the calculation of spatial charge density. The ion distributions and the electric field across the channel are solved by the Poisson equation and the NP equation with several constraints: species flux conservation condition, water equilibrium, and surface adsorption-desorption equilibrium. The EDL structure and measureable parameters are calculated for the potassium chloride solution ranged between

0.001mM and 100mM in channels of 75nm and 490nm. The modeling results are compared with the predictions of the traditional model which assumes the Boltzmann distribution to obtain the EDL structure when salt solutions are at rest. The comparison shows that the structure of an overlapped EDL in the steady flow is significantly different from that at electrostatic equilibrium in several aspects.

First, counterions are unequally enriched in an overlapped EDL. Salt counterions are merely weakly enriched as their enrichment at the midplane is negligible, while hydronium ions are strongly enriched because the pH decreases by 2~3 at the midplane and even more near surfaces. The unequal enrichment occurs because hydronium ions have higher mobility and are more likely to be retained in the channel by the streaming potential. As a result, hydronium ions may be dominant over salt counterions in the channel. The omission of hydronium ions in the calculation of spatial charge density is not appropriate for the steady flow within an overlapped EDL.

Second, channel surfaces are less charged, and charge density becomes as low as only 10~30%, corresponding to more enrichment of hydronium ions. As a result, all electrokinetic effects, such as the streaming potential, the streaming conductance, and the electroviscous effect, are significantly depressed.

Finally, the EDL structure is independent of the concentration of hydronium ions and salt ions in extremely low salt solutions with $\kappa H < \sim 2$. In this case, salt solutions are simply treated as pure water, so that the change of the bulk pH and/or salt concentration in the reservoirs has insignificant impact on the EDL structure.

CHAPTER 6

TRANSIENT ELECTROLYTE SOLUTION

6.1 Introduction

It was revealed from the previous studies that the structure of an overlapped EDL at the steady flow state is a way different from that at electrostatic equilibrium. In this chapter, the evolution of the EDL structure is presented. Numerical simulation is performed for the flow of binary salt solution in a nanochannel connecting with a reservoir at each end. The Poison equation, the NP equation and the NS equation are solved using a finite element method. The proton exchange between channel surfaces and salt solution, and water dissociation are particularly considered. After the simulation, the time scale of ion transport in the nanochannel is examined. An approximate solution based on the time scale analysis is proposed to estimate the time required for the flow to get steady state.

6.2 Modeling Transient Pressure-Driven Flow

Mathematical model is proposed for transient electrokinetic flow of KCl solutions, as an example of binary salt solutions, through a slit-like silica channel. All the species considered in modeling include K^+, H^+, Cl^-, OH^-, and H_2O as it is assumed that KCl is fully dissociated and that water is at self-dissociation equilibrium. Other residual components in a real salt solution are ignored.

6.2.1 Governing Equations

To normalize the governing equations and the relevant boundary conditions, the

following dimensionless parameters and scaled variables listed in Table 6.1 are used.

Table 6.1. Dimensionless parameters and scaled variables

Velocity	u^*	u/U
Ion flux density	j_i^*	$j_i/Uc_{i,\infty}$
Electrical potential	ψ^*	$F\psi/RT$
Pressure	p^*	$p/\rho U^2$
Ionic molar concentration	c_i^*	$c_i/c_{i,\infty}$
Spatial charge density	ρ_e^*	$\Sigma z_i c_i / \Sigma c_{i,\infty}$
Outward flux density	N_i^*	$N_i/Uc_{i,\infty}$
Surface charge density	σ_0^*	$\sigma_0 HF/(\varepsilon\varepsilon_0 RT)$
x,y direction coordinate	x^*, y^*	x/H, y/H
Time	t^*	tU/H
Gradient	∇^*	$H\nabla$
Reynolds number	Re	$\rho UH/\mu$
Schmidt number	Sc_i	$\mu/\rho D_i$

Here, U is the characteristic flow velocity, and H half height of the channel. Superscript * represents the dimensionless parameters, subscript i denotes ith species, including K^+, H^+, Cl^- and OH^-, and subscript ∞ denotes the original salt solution.

The governing equations for electrokinetic flows have been discussed in Chapter 3.

Substituting dimensionless parameters and scaled variables in Table 6.1, Eqs. (3-1)-(3-3), (3-18) and (3-19) are rewritten as

$$\nabla^* \cdot u^* = 0 \tag{6-1}$$

$$\frac{\partial u^*}{\partial t^*} + (u^* \cdot \nabla^*)u^* = \frac{1}{\mathrm{Re}} \nabla^* u^* - \nabla^* p^* - \gamma \rho_e^* \nabla^* \psi^* \tag{6-2}$$

$$\frac{\partial c_{\mathrm{K}^+}^*}{\partial t^*} + \nabla^* \cdot j_{\mathrm{K}^+}^* = 0 \tag{6-3}$$

$$\frac{\partial c_{\mathrm{Cl}^-}^*}{\partial t^*} + \nabla^* \cdot j_{\mathrm{Cl}^-}^* = 0 \tag{6-4}$$

$$\frac{\partial c_{\mathrm{H}^+}^*}{\partial t^*} + u^* \cdot \nabla^* c_{\mathrm{H}^+}^* - \frac{1}{\mathrm{ReSc}_{\mathrm{H}^+}(1+\frac{K_{\mathrm{H_2O}}}{c_{\mathrm{H}^+,\infty}^2 c_{\mathrm{H}^+}^{*2}})} \nabla^* \cdot [(1 + \frac{K_{\mathrm{H_2O}}\mathrm{Sc}_{\mathrm{H}^+}}{c_{\mathrm{H}^+,\infty}^2 c_{\mathrm{H}^+}^{*2}\mathrm{Sc}_{\mathrm{OH}^-}})\left(\nabla^* c_{\mathrm{H}^+}^* + c_{\mathrm{H}^+}^* \nabla^* \psi^*\right)] =$$

$$0 \tag{6-5}$$

$$\nabla^* \cdot \nabla^* \psi^* = -(\kappa H)^2 \rho_e^* \tag{6-6}$$

where $\gamma = \frac{\sum c_{i,\infty} RT}{\rho U^2}$, representing the ratio of thermal energy to kinetic energy. j_i^* is the scaled flux density, which is given by substituting scaled variables into Eq. (3-4)

$$j_i^* = -\frac{1}{\mathrm{ReSc}_i} \nabla^* c_i^* + c_i^* u^* - \frac{z_i c_i^*}{\mathrm{ReSc}_i} \nabla^* \psi^* \tag{6-7}$$

It is assumed that dissociation equilibrium of water is established much faster than other physical and chemical processes, and that the dissociation constant is identical throughout salt solution, yielding a relation between H^+ and OH^- as described by Eq. (3-17)

$$c_{\mathrm{H}^+}^* c_{\mathrm{OH}^-}^* = 1 \tag{6-8}$$

6.3.2 Proton Transfer at Channel Surfaces

When silica surfaces are in contact with water or dilute salt solutions, the dissociation of silanol groups shown in Eq. (2-1) is the principal mechanism accounting for the

appearance of net change on surfaces [16, 30]. Other possible chemical reactions associated with silica surfaces are considered inert. The dynamic single site model presented in Chapter 3 is used to treat the coupling effects of the electric potential field and proton activity at the solid-liquid interface. It is further assumed that chemical reaction on channel surfaces is faster by a few orders of magnitude than transport of H^+ in salt solutions. Hence, there is always at chemical equilibrium throughout the transient process. Surface charge density can be described by Eq. (3-31), whose dimensionless form is given by

$$\sigma_0^* = -\frac{F^2 \Gamma_{\text{total}} H}{\varepsilon_0 \varepsilon RT (c_{\text{H}^+,\infty} c^*_{\text{H}^+,0} 10^{\text{pK}} + 1)} \tag{6-9}$$

where $c^*_{\text{H}^+,0}$ is dimensionless proton activity at the surfaces, which is related to $c^*_{\text{H}^+,d}$, the dimensionless concentration of H^+ at the shear plane, by assuming the Boltzmann equilibrium

$$c^*_{\text{H}^+,0} = c^*_{\text{H}^+,d} \exp\left[-\frac{RT}{F}(\psi_0 - \zeta)\right] \tag{6-10}$$

where ζ is Zeta potential and ψ_0 is the potential at the surface.

According to the zeroth-order Stern model, ζ and ψ_0 are related via. Eq. (3-24)

$$C = \frac{\sigma_0}{\psi_0 - \zeta} \tag{6-11}$$

Substituting Eq. (6-11) into Eq. (6-10) gives rise to

$$c^*_{\text{H}^+,0} = c^*_{\text{H}^+,d} \exp\left(-\frac{RT\sigma_0}{FC}\right) \tag{6-12}$$

For electrokinetic flows at room temperature with typical parameters of $\sigma_0 = -1$ mC/m^2 and C = 2.9 F/m^2, the difference between $c^*_{\text{H}^+,0}$ and $c^*_{\text{H}^+,d}$ is as low as less than 2%. Therefore, it is practicable to assume the proton activities at the surface and at the shear plane are identical. Eq. (6-12) is then rewritten as

$$c^*_{\mathrm{H}^+,0} = c^*_{\mathrm{H}^+,d} \tag{6-13}$$

Eq. (6-13) can be actually achieved from the Gouy-Chapman model [15, 30] for the diffuse layer, in which ψ_0 is assumed to be identical with ζ.

Substituting Eq. (6-13) to Eq. (6-9) yields

$$\sigma_0^* = -\frac{F^2 \Gamma_{\mathrm{total}} H}{\varepsilon_0 \varepsilon R T (c_{\mathrm{H}^+,\infty} c^*_{\mathrm{H}^+,\mathrm{d}} 10^{\mathrm{pK}} + 1)} \tag{6-14}$$

The outward flux density, N_i, is defined as the rate of *i*th ion leaving the bulk at the boundary per unit area

$$N_i^* = \vec{n} \cdot j_i^* \qquad \text{for } i = \mathrm{K}^+, \mathrm{Cl}^- \tag{6-15}$$

$$N_i^* = \vec{n} \cdot \left(j_i^* + \frac{c_{\mathrm{H_2O},\infty}}{c_{i,\infty}} j^*_{\mathrm{H_2O}} \right) \qquad \text{for } i = \mathrm{H}^+, \mathrm{OH}^- \tag{6-16}$$

where $\vec{n}$ is the normal unit vector perpendicular to the surface. The outward flux density of water molecules in Eq. (6-16) represents the contribution of water dissociation to the flux density of hydronium and hydroxide ions. Hydronium ions confined in the Stern layer are treated as part of the channel surfaces, instead of the bulk solution.

Because protons are bounded with only SiO^- groups at the channel surfaces, hydronium ions leave the bulk as many as the loss of SiO^- groups, yielding

$$N_{\mathrm{H}^+} = -\frac{\partial \Gamma_{\mathrm{SiO}^-}}{\partial t} \tag{6-17}$$

Substituting Eq. (6-9) into Eq. (6-17) and normalizing, the out flux density of H^+ is related to surface proton activity

$$N^*_{H^+} = \frac{\Gamma_{total} 10^{pK}}{H\left(c^*_{H^+} c_{H^+,\infty} 10^{pK} + 1\right)^2} \frac{\partial c^*_{H^+}}{\partial t^*} \tag{6-18}$$

which suggests that net proton exchange will not occur at the steady state when surface activity of protons becomes stationary.

6.3 Numerical Methodology

The coupled governing equations of Eqs. (6-1)-(6-6) were solved using the commercial software package COMSOL 3.5a Multiphysics. The equation system was specified in the PDE coefficient form application model, and solved by the finite element analysis with a Lagrange multiplier method.

6.4.1 Computation Geometry

The computational domain for a nanochannel connecting to a well at each end is sketched in Fig. 6.1, which is not drawn to scale. Only half of the physical domain was used for computation due to the geometrical symmetry. The channel with length L of 10 μm and half height H of 100 nm is confined between the surface numbered as 4 and the symmetric plane as 8. The upstream and downstream wells are confined between planes 1238 and 5678, respectively, each of which is 50 μm long and 50 μm high. A scaled Cartesian coordinate system is used where the channel mid-section is located at $x^* = 0$, the channel entrance at $x^* = -50$, the channel exit at $x^* = 50$, the channel wall at $y^* = 1$, and the symmetric plane at $y^* = 0$. The reduction of the flow area due to the Stern layer is disregarded since the Stern layer is typically one ionic diameter thick(~0.5 nm), notably less than the channel height.

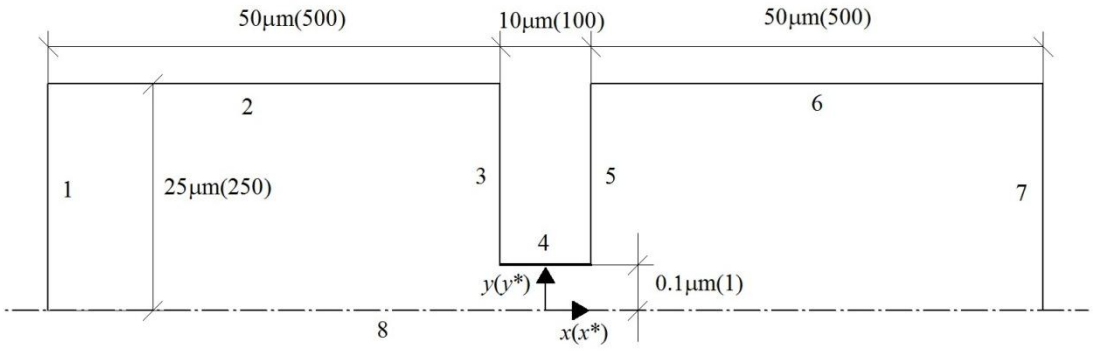

Fig. 6.1. Computational domain for a nanochannel connecting to a well at each end

6.4.2 Boundary and Initial Conditions

The boundary conditions subjected to the governing equations are summarized in Table 6.2.

Table 6.2. Boundary conditions

Plane	u^*	K^+ & Cl^-	H^+	ψ^*
1	$p^* = \frac{3\mu L}{\rho U H^2}$	$c_i^* = 1$	$c_i^* = 1$	$\psi^* = 0$
2,3,5,6	$u^* = 0$	$N_i^* = 0$	Eq. (6-20)	$\vec{n} \cdot \nabla^* \psi^* = 0$
4	$u^* = 0$	$N_i^* = 0$	Eq. (6-19)	$\vec{n} \cdot \nabla^* \psi^* = \sigma_0^*$
7	$p^* = 0$	$c_i^* = 1$	$c_i^* = 1$	$\nabla^* \psi^* = 0$
8	$\vec{n} \cdot u^* = 0$	$N_i^* = 0$	Eq. (6-20)	$\vec{n} \cdot \nabla^* \psi^* = 0$

The flow enters the domain at plane 1 and leaves at plane 2 in response to the suddenly applied external pressure difference. These planes are regarded as reservoirs where ion concentrations are fixed. The electric field is grounded at the inlet and isolated at the outlet. In convenience to investigate the electroviscous effect, the pressure difference is imposed as what is required to achieve an average flow rate of *U* for the Poiseuille flow through a channel of the same height.

Plane 4 represents the channel surface where the impact of the EDL must be considered. The fluid is regarded as motionless below a shear layer which is identical to the inner Helmholtz plane according to the Basic Stern model. The layer is typically one ionic diameter thick (~ 0.4 nm), no more than 1% of the channel height, so that the narrowing is ignored in modeling. When the dissociation-association equilibrium is assumed, the boundary condition subjected to the Poisson equation is imposed as surface charge density described by Eq. (6-9). Salt ions are isolated at plane 4, but the proton exchange that is critical to the electronic flow must be consider for the transport of hydronium ions in the bulk solution. Combining Eqs. (6-7), (6-8), (6-16) and (6-18) yields

$$\frac{1}{\mathrm{ReSc_{H^+}}}\vec{n}\cdot\left[\left(1+\frac{K_{\mathrm{H_2O}}\mathrm{Sc_{H^+}}}{c_{\mathrm{H^+},\infty}^{2}\mathrm{Sc_{OH^-}}}\frac{1}{c_{\mathrm{H^+}}^{*2}}\right)\left(\nabla^{*}c_{\mathrm{H^+}}^{*}+c_{\mathrm{H^+}}^{*}\nabla^{*}\psi^{*}\right)\right]=$$

$$-\frac{\Gamma_{\mathrm{total}}10^{\mathrm{pK}}}{H\left(c_{\mathrm{H^+}}^{*}c_{\mathrm{H^+},\infty}10^{\mathrm{pK}}+1\right)^{2}}\frac{\partial c_{\mathrm{H^+}}^{*}}{\partial t^{*}} \tag{6-19}$$

Planes 2, 3, 5, and 6 are the well walls where no-slip condition for fluid, electric isolation, and no-penetration conditions for all ions are used. At plane 8, all physicals are symmetric. Applying $N_{\mathrm{H^+}}^{*}=N_{\mathrm{OH^-}}^{*}=0$, the boundary condition for the transport of hydronium ions at these planes is written as

$$\frac{1}{\mathrm{ReSc_{H^+}}}\vec{n}\cdot\left[\left(1+\frac{K_{\mathrm{H_2O}}\mathrm{Sc_{H^+}}}{c_{\mathrm{H^+},\infty}^{2}\mathrm{Sc_{OH^-}}}\frac{1}{c_{\mathrm{H^+}}^{*2}}\right)\left(\nabla^{*}c_{\mathrm{H^+}}^{*}+c_{\mathrm{H^+}}^{*}\nabla^{*}\psi^{*}\right)\right]=0 \tag{6-20}$$

The system is initially at electrostatic equilibrium which is obtained by soling the stationary problem in the same computation domain. The boundary conditions listed in Table 6.2 were used, except that p^* was imposed as zero at plane 1 to get rid of the external pressure difference.

6.4.3 Mesh and Time Steps

The computations were performed in a finite element mesh made of 20 × 600 quadrilateral elements in the channel and 44350 triangular elements in the wells as schemed in Fig. 6.2. The mesh was refined near the channel wall and at the interface between the channel and the wells where the potential and concentration gradients are pronounced. The closest grid to the channel wall is in a distance of less than 1.5 nm.

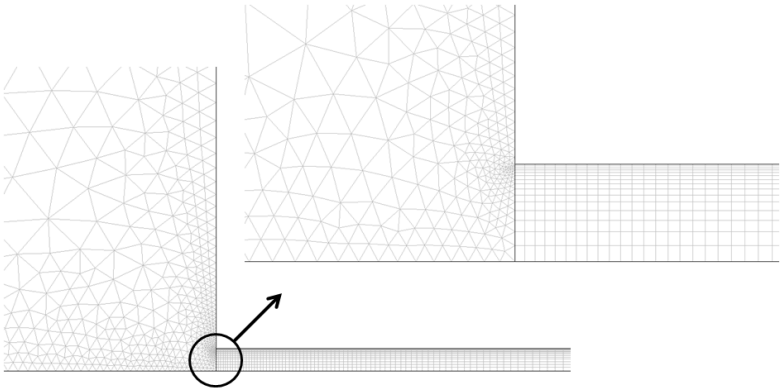

Fig. 6.2. Meshes at the channel entrance

The dimensionless time steps are basically controlled by the built-in time step solver BDF which uses various-orders variable-step-size backward differentiation formulas, but the maximum time step is bounded to 0.05 for $t^* < 1000$ and 3 for $t^* \geq 1000$.

6.4.4 Parameter Range Used in Calculations

The flow of 0.01 mM KCl was simulated with the following physical parameters: T = 25 °C, ρ = 1000 Kg/m^3, μ = 0.8904 × 10^{-3} Pa·s, ε = 78.54, Λ = 5.0 nm^{-2}, pK = 7.5, D_{K^+} = 1.96 × 10^{-9} m^2/s, D_{Cl^-} = 2.03 × 10^{-9} m^2/s, D_{H^+} = 9.31 × 10^{-9} m^2/s, and D_{OH^-} = 5.28 × 10^{-9} m^2/s. The corresponding κH is 1, indicating the existence of EDL overlap in the studied channel.

The characteristic velocity U is chosen as 0.196 m/s to make ReSc_i at the order of unity. The simulated flow meets the condition of $H/L << \mathrm{ReSc}_i << L/H$, just like typical electrokinetic flows. When the flow reaches the steady state, the variation of ionic concentration and electric potential along the streamwise direction is insignificant inside the channel. The entrance effect exists only near the ends of the channel. If the flow is rather slow such as $\mathrm{ReSc}_i \sim H/L$, the entrance effect plays an important role to the flow. A slower flow with $\mathrm{ReSc}_i << H/L$ causes no change of the EDL structure due to the convective transport of ions is negligible. In the case of $\mathrm{ReSc}_i \sim L/H$, the EDL effect is strongly depressed by the extremely strong convective transport of ions, and ion distribution in the channel is close to what is in the upstream well. Therefore, the imposed value of U ensures that this study focus on the electrokinetic flow with negligible entrance effects. More details can be found later in the section of scale analysis of ion transport.

6.5. Validation of Numerical Simulation

Mesh and time stepping method have been validated first. And then the accuracy of the model is examined for the steady state flow and for static solution, two problems whose analytical solutions exist under conditions of EDL overlap.

6.5.1 Mesh Validation

Grid resolution tests were performed for finer grids (20 × 1200 quads + 2 × 18100 triangles, and 25 × 1000 quads + 2 × 16900 triangles) and a coarse grid (15 × 400 quads + 2 × 16400 triangles). Fig. 6.3 plots profiles of hydronium ion concentration along the channel midsection ($x^* = 0$) resulted from different grids at $t^* = 1000$ and 20000. Distribution of hydornium ion is focused here mainly because its distriubtion has the most violent transient feature in comparison with other physical responses, and also because hydronium ions are the key reason accounting for the transient of the EDL structure.

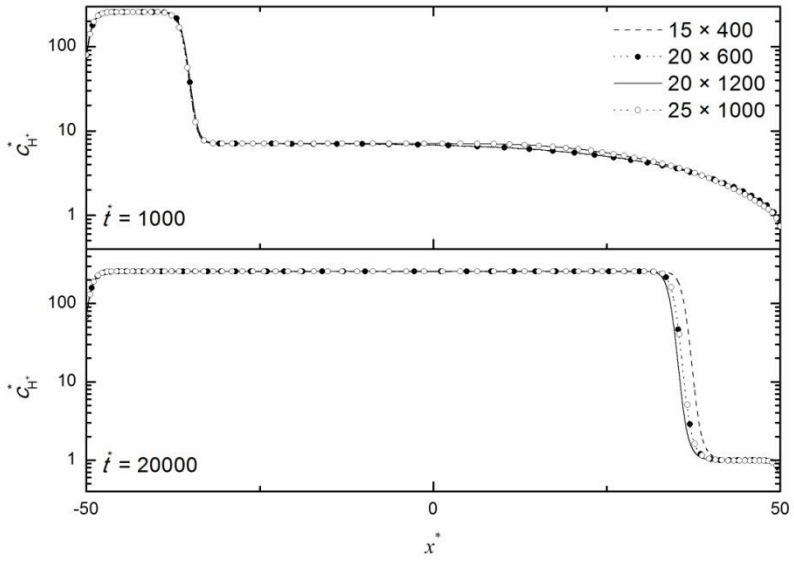

Fig. 6.3. Comparison of profiles of hydronium concentration along the channel midsection ($x^* = 0$) when using different meshes

The comparison shows the results are almost independent of mesh size at $t^* = 1000$, as all curves are nearly overlapped. At $t^* = 20000$, the profiles are slightly different, mainly at the position where the large variation of the concentration occurs. The prediction from the coarse grid is significantly closer to the channel exit, but the other predicitons agree

well with each other. Overall, the influence of mesh size is quite limited, especially at the beginning of the transient.

6.5.1 Validation of Time Steps

Time steps are determined mainly by the built-in time-step solver of 'BDF'. 'BDF' stands for the multi-step backward differentiation formula, meaning that it keeps and uses information from previous steps to calculate the next one. If no other restrictions are considered, time steps solved by the solver are initially below 0.01 at the very beginning, and gradually growing up to a few seconds after t^* = 10 and more than 10 seconds after t^* = 1000.

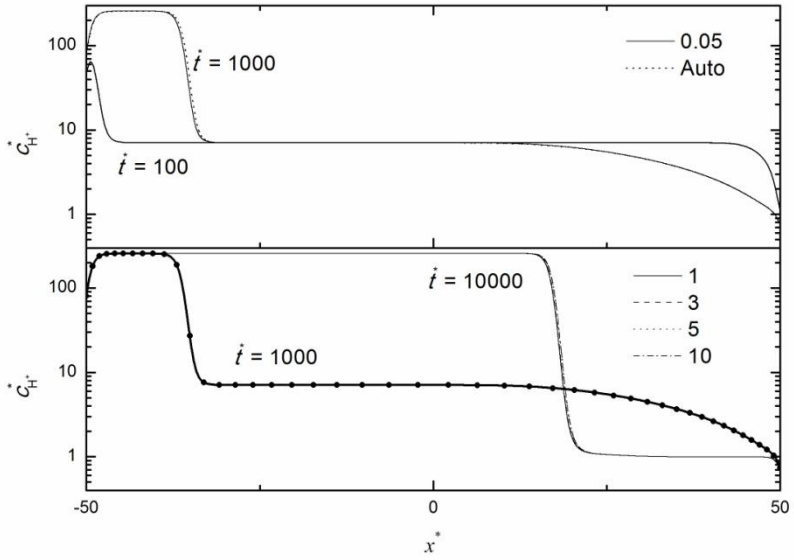

Fig. 6.4. Comparison of profiles of hydronium concentration along the channel midsection when using different maximum time steps

To examine the influence of time stepping on the simulation, the maximum time step is set as 0.05 for $t^* < 1000$, and 1, 3, 5, 10 for $t^* \geq 1000$. These additional restrictions

greatly short time steps, most of which are equal to the maximum time step. The predicted concentration profiles of hydronium ion show a difference below 2%, as shown in Fig. 6.5. Thus, the time stepping method used in the current simulation is validated.

6.5.1 Analytical Model for Static Solution

We now develop an analytical model for motionless KCl solution in a slit-like channel whose ends are connected to reservoirs. In the absence of the convective transport, ions are assumed to follow the Boltzmann distribution. Eq. (3-6) can be rewritten in a dimensionless form

$$c_i^* = \exp(-z_i \psi^*) \tag{6-21}$$

where the electric potential field and ion distribution are referred to the reservoirs where the electroneutrality exists, and then $\psi_\infty^* = 0$ and $c_{i,\infty}^* = 1$. Eq. (6-21) is applicable for static solution regardless of whether the EDLs are overlapped.

If the channel is sufficiently long, we can assume that the electric field is determined by the PB equation. Eq. (3-20) is represented by

$$\frac{\mathrm{d}^2\psi^*}{\mathrm{d}y^{*2}} = (\kappa H)^2 \sinh(\psi^*) \tag{6-22}$$

with the boundary conditions of $\frac{\mathrm{d}\psi^*(y^*=0)}{\mathrm{d}y^*} = 0$, and $\psi^*(y^* = 0) = \psi_c^*$. In an overlapped EDL, ψ_c^* is a non-zero value due to the loss of the electroneutrality at the channel midplane. The analytical solution of the equation above is given by [15]

$$\psi^* = \psi_c^* + 2 \ln \mathrm{cd}(n|m) \tag{6-23}$$

where $n = \kappa H y^* \exp(-\psi_c^*/2)/2$ and $m = \exp(2\psi_c^*)$.

Concentration profiles across the channel are obtained by substituting Eq. (6-23)

into Eq. (6-21)

$$c_{\mathrm{i}}^{*} = \exp\left(-z_{\mathrm{i}}\psi_{c}^{*}\right)\mathrm{cd}^{-2z_{\mathrm{i}}}(n|m) \tag{6-24}$$

Setting y^{*} = 1 in Eq. (6-24), the proton activity at the shear plane is given by

$$c_{\mathrm{H^{+}},\mathrm{d}}^{*} = \exp\left(-\psi_{c}^{*}\right)\mathrm{cd}^{-2}(n(y^{*}=1)|m) \tag{6-25}$$

Surface charge density is obtained from Eq. (6-22)

$$\sigma_{0}^{*} = \left.\frac{\mathrm{d}\psi^{*}}{\mathrm{d}y^{*}}\right|_{y^{*}=1} = \kappa H\left(\mathrm{m}^{\frac{3}{4}} - \mathrm{m}^{-\frac{1}{4}}\right)\frac{\mathrm{sd}(n(y^{*}=1)|m)}{\mathrm{cn}(n(y^{*}=1)|m)} \tag{6-26}$$

Eqs. (6-14), (6-25) and (6-26) were solved simultaneously for ψ_{c}^{*}, σ_{0}^{*} and $c_{\mathrm{H^{+}},d}^{*}$ using Matlab R2009a. Ion profiles given by Eq. (6-24) are finally determined with the substitution of a solved ψ_{c}^{*}.

6.5.2 Analytical Model for Steady State Flow

We presented an analytical model for the steady pressure-driven flow in a slit-like channel in Chapter 5. To be identical with the single site model used in this chapter, the previous analytical model is modified by replacing Eq. (5-6) with Eq. (6-14). More details about the modeling can be found in Chapter 5.

6.5.3 Comparison of Numerical and Analytical Results

The comparison of ion concentrations along the channel midsection(x^{*} = 0) is presented for static solution in Fig. 6.5 and for the steady state flow in Fig. 6.6. The overlap of the curves shows that numerical and analytical results are in excellent agreement for both cases. It validates the accuracy of the simulation model. Meanwhile, the agreement suggests that the assumptions used for the derivation of the analytic solutions are appropriate under conditions of EDL overlap. More specifically, ions follow Boltzmann distri-

bution at electrostatic equilibrium, while the species flux conservation should be obeyed at the steady state flow.

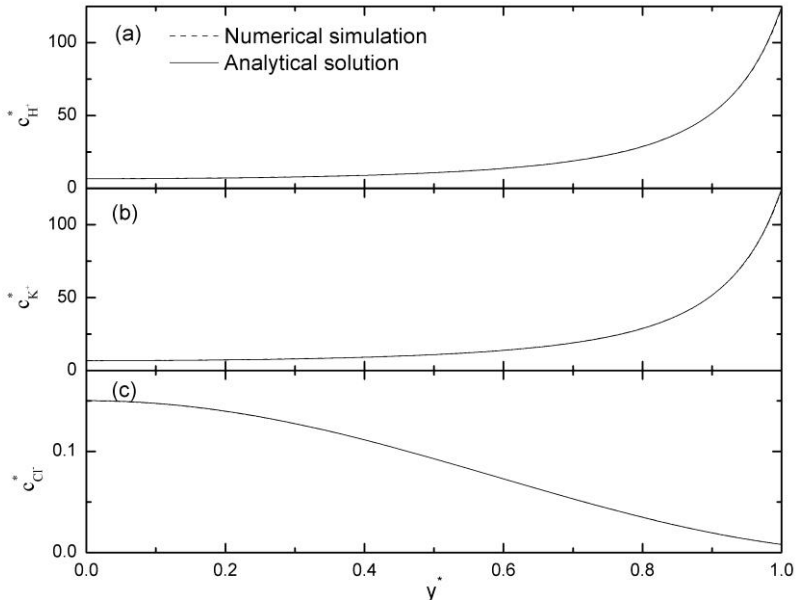

Fig. 6.5. Comparison of numerical simulation and analytic solution in concentration profiles of a) H^+, b) K^+, and c) Cl^- for static fluid at the midsection

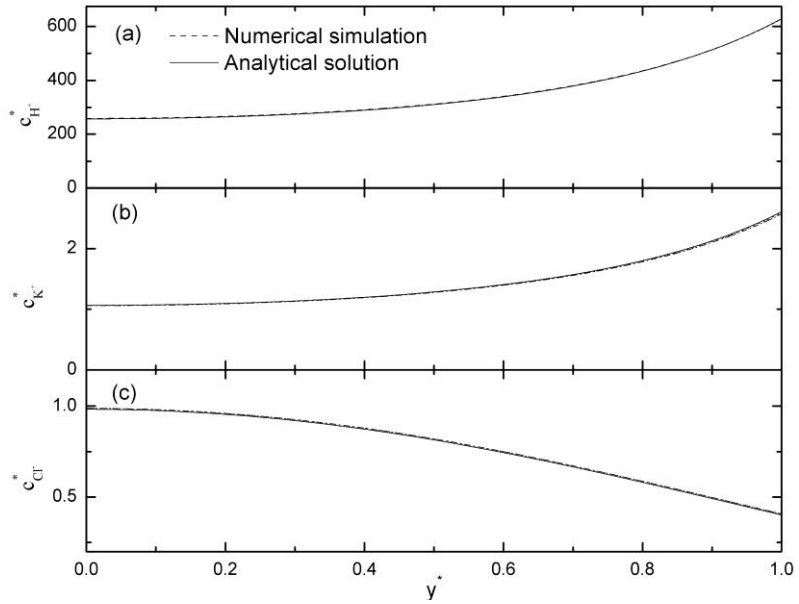

Fig. 6.6. Comparison of numerical simulation and analytic solution in concentration profiles of a) H^+, b) K^+, and c) Cl^- for steady flow at the midsection

6.6. Simulation Results

The transient of the EDL structure is the principle feature of the studied electro-kinetic flow. The flow results in redistribution of ions, and variation of surface charge density and the electric field in the channel. When counterions are enriched at the down-stream end of the channel, the time-dependent enrichment induces and varies the streaming potential, i.e. the potential difference between two wells. According to the characteristics of ionic distribution, surface charge, and the streaming potential during the process starting from initial relax state, the transient flow is divided into three stages: early, middle, and late.

6.6.1 The Early Stage

The early stage is featured by the increasing streaming potential, as well as the in-significant change of the EDL structure inside the channel. Its time range is between 0 and ~10 for the current simulation. Fig. 6.7 and Fig. 6.8 plot the electric potential and ion concentrations along the centerline ($y^* = 0$) in and near the channel at the early stage, re-spectively. The initial electric field is attributed to negative charges on the channel surfaces. The electric potential is slightly smaller in the channel than in the wells, and there is no electric potential difference between the wells. The streaming potential keeps increasing as shown in Fig. 6.7.

At the very beginning, the applied pressure difference drives the salt solution in a way free of influence of mobile ions. The Poiseuille flow has been fully established before the hydrodynamic relaxation time of $\rho H^2/3\mu$, evaluated as 0.007 if scaled by H/U to be consistence with the simulation. In such a short time, the downstream enrichment of

counterions due to the transport of the bulk flow is not sufficient to arise a significant streaming electric field. Hence, the transient process is not much different from the development of the Poiseuille flow.

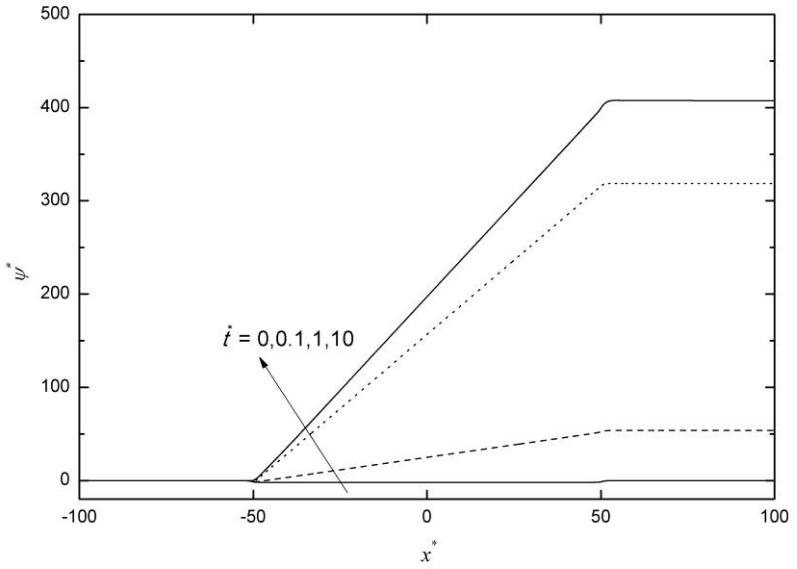

Fig. 6.7. Potential profiles along the centerline($y^* = 0$) at the early stage

The electrokinetic flow starts to deviates from the Poiseuille flow upon the presence of the streaming potential. Fig. 6.8 shows all three ions slightly shift downstream at $t^* = 0.1$. At the same time, the streaming potential slightly but apparently increases, as shown in Fig. 6.7. However, the streamwise electromigration of ions is too small to act against the convection. As a result, the concentration profile of ions shift as a whole without significant distortion from their initial state.

At $t^* = 0.1$~10, the transport of ions is being considerably affected by the streamwise electromigration, which becomes stronger and stronger with the increase of the streaming potential. First of all, H^+ are pushed upstream from the exit where they are en-

riched at $t^* = 0.1$ and become even depleted at $t^* = 10$. Meanwhile, the bulk flow tends to carry more H^+ into the channel. The opposite transports conflict at the entrance, forming a concentration hump. Second, K^+ continue to accumulate near the exit. The concentration profiles of K^+ and H^+, shift along the opposite direction, because H^+ with higher mobility move almost 5 times as fast as K^+ in response to the streaming potential. K^+ which are less affected are able to continuously move downstream with the bulk flow, leading to a higher electrical potential in the downstream well. Finally, Cl^- travel downstream like K^+, but in a more violent way. The streaming potential accelerates coions, so that Cl^- from the upstream well buffer its initial depletion in the channel. Overall, the change of the EDL structure mainly occurs near the ends of the channel during the early stage. If the Boltzmann distribution is assumed for modeling the pressure-driven flow within an overlapped EDL [5, 6, 19-21], the model likely provides the information at the end of the early stage.

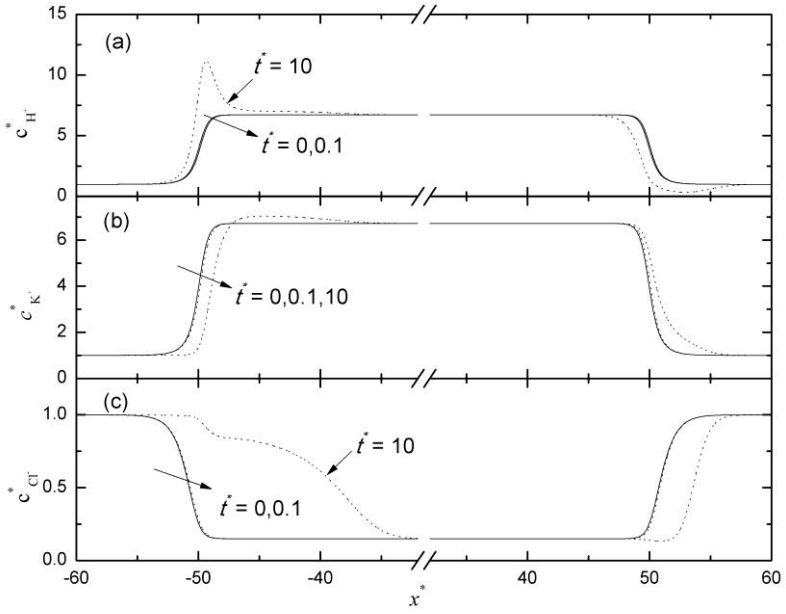

Fig. 6.8. Concentration profiles along the centerline at the early stage

Similar initial transient of concentration and potential profiles has been reported for the flow in a finite capillary of radius 1 or 5 times the Debye length without concerning H^+ and OH^- [44], because H^+ has negligible contribution to electrokinetic flows comparing to K^+ or salt counterions at the early stage.

6.6.2 The Middle and Late Stage

The middle stage following the early one, ends by the hydraulic retention time (HRT), L/U, the time needed for the Poiseuille flow to sweep over the channel once. HRT is equal to 100 if scaled H/U for the current simulation. Fig. 6.9 plots the concentration profiles along the centerline in the channel including the region near its ends for $t^* = 10$, 20, 50 and 100. One of main features of this stage is the significant increase of the concentration of Cl^-. By the end of the middle stage, it rises up to nearly the original salt solution at the centerline. As a consequence, the enrichment of H^+ and K^+ are slightly and equally enhanced to maintain electroneutrality across the channel including the walls. Therefore, all ions become more dense in the channel. The concentration hump of H^+ steadily grows at the entrance. The other important features of the middle stage include the decrease of the streaming potential due to the upstream shift of H^+ and K^+ at the exit, and insignificant change of surface charges. More discussions of these two features are shown later. Some of main features of the early and middle stage are in consistence with the previous simulation for the capillary flow with an overlapped EDL and with the assumption of constant surface charges [44].

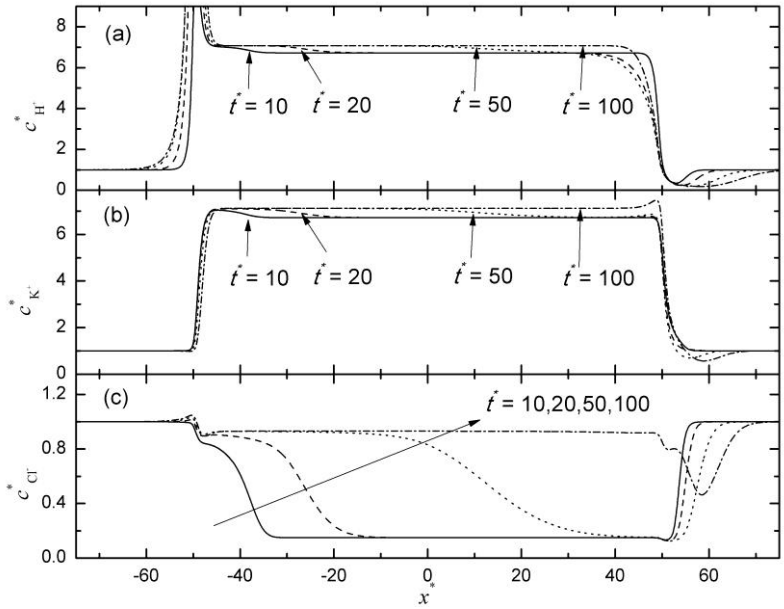

Fig. 6.9. Potential profiles along the centerline at the late stage

The late stage is the last period before final steady state. This stage distinguishes from the first two stage mainly because of large variation of concentrations of counterions as shown in Fig. 6.10. The curves for $t^* = 30000$ in the figure represent ion distributions at steady state.

Fig. 6.10a presents a series of concentration profiles of H^+ at the late stage. The growth of the concentration hump of H^+ continues before $t^* = 500$ when its peak value rises up to as highly as ~250. After then, the uphill side of the concentration hump will not change any longer in position and shape, while the downhill side propagates downstream like a concentration plug. The flat plateau of the concentration humps implies that the enrichment of H^+ is enhanced by about two orders of magnitude and stays stationary after the concentration plug passes. The front side of the plug is a narrow region, so called the transit region, across which there is a sharp variation in concentration. In the other direction, the depletion region of H^+ which is right next to the channel exit at $t^* = 10$, extends upstream

and eventually meets the shock wave near $x^* = 0$ at $t^* = 5000$. The depletion region plays an important role to sucking H^+ into the channel from the downstream well. Thus, H^+ are redistributed through the downstream propagation of the concentration plug and the up-stream expansion of the depletion region. At the places where the propagation/extension has not arrived yet, the concentration is not different from the end of the middle stage. The redistribution of H^+ has profound influence on the distribution of other ions, surface charge and the electric potential field.

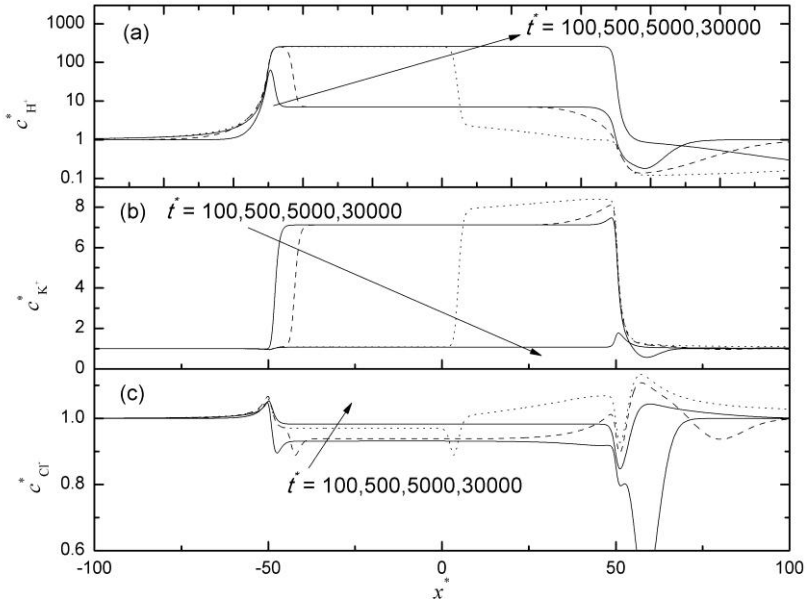

Fig. 6.10. Concentration profiles along the centerline at the late stage

A similar plug-like propagation is shown in Fig. 6.10b for K^+ and in Fig. 6.10c for Cl^-. Unlike H^+, the concentration plug of K^+ initially exists in the channel, and travels out of the channel exit. By the end of the late stage, its initial enrichment is largely reduced. The concentration of K^+ slightly increases at the downstream part before the concentration plug arrives, in a response to the depletion of H^+ which causes surfaces more charged to

attract more K^+. The transient redistribution of Cl^- is dependent on the variation of H^+ as well, but it is negligible comparing to the large variation of counterions. At the steady state, the concentration of Cl^- slightly increases in the channel.

To capture the transient behavior of transverse ion distributions at the late stage, Fig. 6.11 plots the concentration profiles of H^+ and K^+ across the midsection ($x^* = 0$) where the concentration plugs arrive at $t^* = \sim 4500$. The plotted profiles for $t^* = 4000$, 4500, 5000 represent typical transverse ionic distributions before, during, and after the concentration plugs. The transverse distribution of Cl^- is not investigated because of its less significance. The figure shows that the concentrations of both ions radically rise up toward the walls at all times. The curve of H^+ is slightly lower at $t^* = 4000$ when the downstream depletion has a significant influence on ion distribution at the midsection, than the one at $t^* = 100$. Next, it jumps up from $t^* = 4000$ to 4500 and to 5000, implying that H^+ are enriched in the whole channel when experiencing the propagation. The transverse distribution of H^+ behind the concentration plug becomes nearly stationary as the profiles for $t^* = 5000$ and 30000 are almost overlapped. Therefore, it is concluded that the transient feature of H^+ along the centerline is also true for its transverse distribution. The same conclusion for K^+ can be drawn through similar analysis of Fig. 6.11b. In fact, the transverse equilibrium is established at time scale of H/D_i^2, which is faster than the streamwise transport by a few orders of magnitude. The transverse transport of ions can be regarded as at quasi-steady equilibrium except in the transit region.

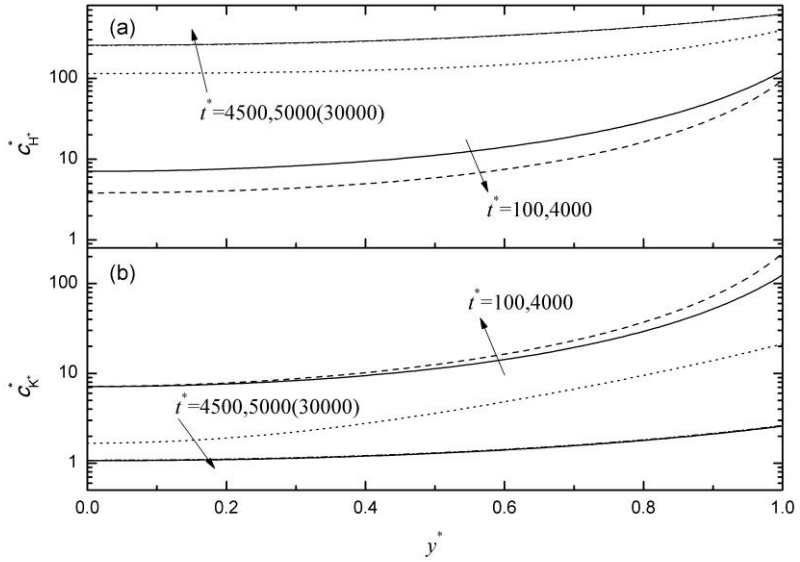

Fig. 6.11. Transverse ionic distribution at the midsection

At the middle and late stage, the streaming potential keeps dropping. Fig. 6.12 plots the electric potential along the centerline for t^* = 10, 100, 500, 5000, and 30000. The streaming potential monotonically decreases with respect to time by more than half. The curve for t^* = 5000 consists of two linear segments, the flatter one at x^* = -50~5 and the steeper one at x^* = 5~50. The turn point corresponds to the position of the shock wave. It suggests that the streamwise electric field in the channel separates two regions. The one in the upstream part is weaker, while the other one is stronger. Accompanying with the propagation of the concentration plugs, the weaker electric field replaces the stronger one in the channel.

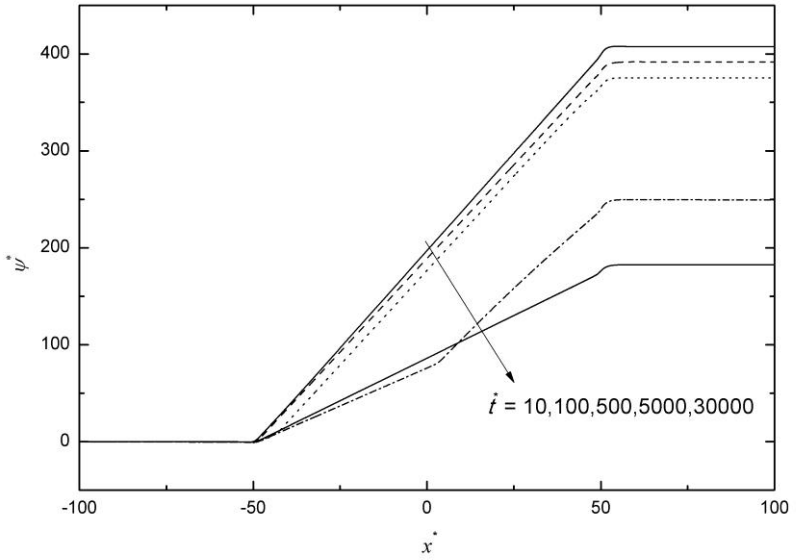

Fig. 6.12. Potential profiles along the centerline at the middle and late stage

6.6.3 Surface Charge Density

Surface charge density is plotted in Fig. 6.13 for typical moments in the early, middle and late stage. The surfaces are equally charged in the channel except near its ends at $t^* = 0$ and $t^* = 100$. Local charge density varies in a difference of less than 0.1% before the late stage, corresponding to the insignificant variation of ion concentrations. During the late stage, however, surface charge significantly varies via the proton exchange with the bulk solution. It variation is strongly related to the transient redistribution of H^+. There is a transit region presenting a large variation of surface charge, in consistence with the concentration plug propagation of H^+. The transit region propagates downstream, leaving an equal but less charge density behind. For the current simulation, charge density drops to only one fifth of its initial value after the concentration plugs sweep. In response to the depletion region of H^+, a more-charged region is initially formed at the channel exit and

extends upstream. After $t^* = 15000$, surface charge density doubles at the downstream part of the channel. Large variation of surface charge is the unique feature of the late stage. Furthermore, it reflects local proton exchange with the bulk solution. The channel surfaces release protons at the downstream part, absorb protons at the transit region, and barely exchange at the upstream part.

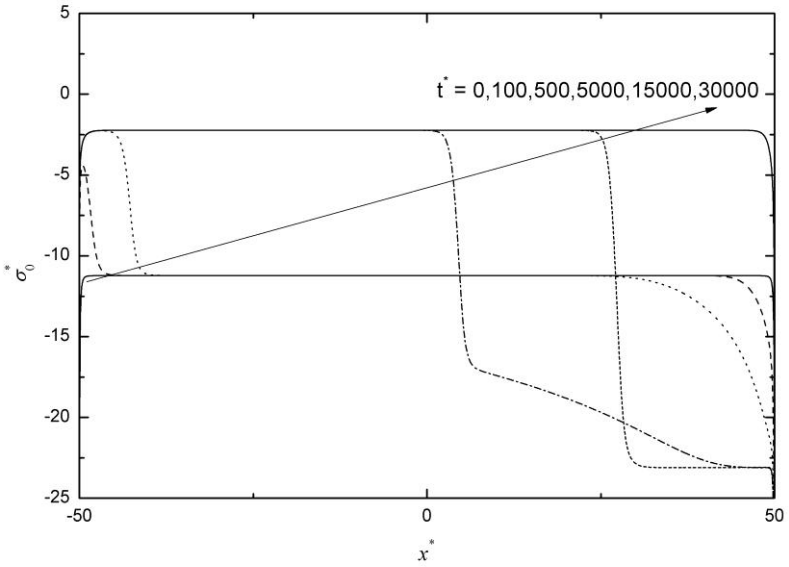

Fig. 6.13. Net charge density on the channel surfaces

6.6.4 Ion Transport at the Late Stage

To further understand the role that ion transport plays to the redistribution of ions during the late stage, the flux density of H^+ and K^+ in the channel at $t^* = 4500$ are investigated.

Fig. 6.14a demonstrates the direction of the flux of H^+ around the midsection where the transit region locates. The figure is not scaled to reflect the magnitude. It is shown that H^+ are moving upstream in the downstream part of the channel ($x^* > 2$) where the

streamwise electric field is sufficiently strong to overcome the convective transport. H^+ are circulating in the upstream part ($x^* < -1$) and in the transit region ($-1 < x^* < 2$) because the dominant transport component is the convection in the neighborhood of the channel center but the electromigration near the walls.

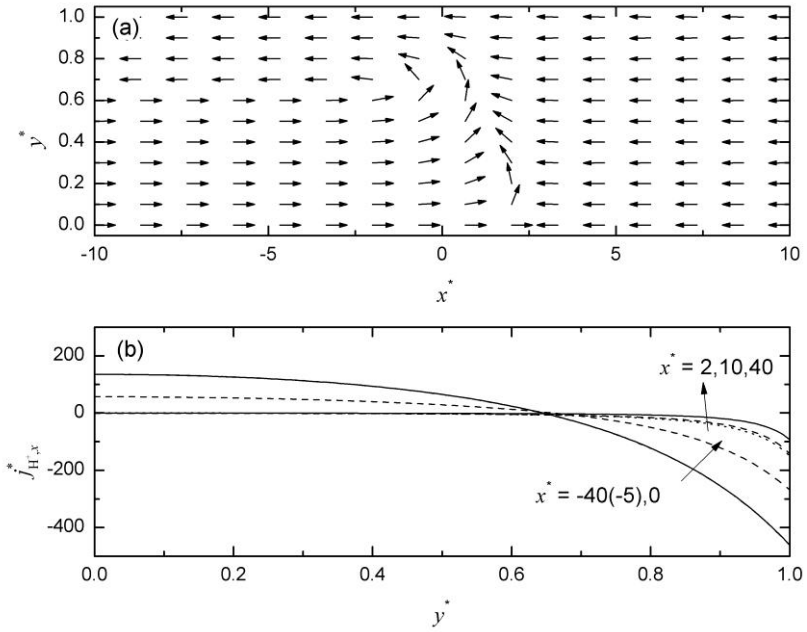

Fig. 6.14. Flux density of H^+ at $t^* = 4500$. a) normalized flux density near the midsection, and b) streamwise flux density along cross sections.

Fig. 6.14b plots the streamwise flux density of H^+ along various cross sections at $t^* = 4500$. In the upstream part except at the very end ($x^* < -45$) where the end effect is strong, the profiles are identical. The overlapped profiles at $x^* = -5$ and -40 is shown in the figure as an example. The flux density is relative large due to the strong enrichment of H^+, but the total streamwise flux across the channel, i.e. the integration of the flux density along the cross section, is as small as $-0.07UHc_{H^+,\infty}$. In the downstream part, all profiles are entirely below zero, and the closer to the shock wave, the lower the profiles. The total streamwise

flux varies from $-6.5UHc_{H^+,\infty}$ at $x^* = 40$ to $-14.0UHc_{H^+,\infty}$ at $x^* = 2$. Its value is not a constant because the surfaces are releasing protons into the bulk solution. When the total streamwise fluxes from the downstream and upstream parts are compared, it can be concluded that H^+ circulating inside the upstream part nearly enter the transit region, while H^+ sucked from the downstream well and released by the surfaces in the downstream part are stored in the transit region. The storage is either in the bulk solution as free ions, or on the surfaces as components bounded with silanol groups. Once local storage is completed, the concentration plug propagates forward.

Fig. 6.15 demonstrates the transport of K^+ with the same configuration as Fig. 6.14. There are two separate circulations, one in the upstream part, and the other in the downstream part including the transit region. In the upstream part, K^+ are mostly moving downstream except near the walls. Profiles of the streamwise flux density are overlapped in the upstream part, such as those at $x^* = -5$ and at $x^* = -40$ as shown in Fig. 6.15b. The corresponding streamwise flux is evaluated as $0.85UHc_{K^+,\infty}$. Recalling that the flow with average flow rate of $0.84U$ at this moment brings K^+ into the channel at the rate of $0.84UHc_{K^+,\infty}$, no K^+ are left in the upstream part as the fluxes are equal within a small calculation error. In the downstream part, K^+ are circulating with a larger magnitude. Its streamwise flux decreases along the flow direction from $0.99UHc_{K^+,\infty}$ at $x^* = 2$ to $0.91UHc_{K^+,\infty}$ at $x^* = 40$, but apparently larger than the coming flux. It implies that the coming flux is unable to compensate all the loss in the transit region where K^+ will be less enriched. And a number of K^+ are retained in the downstream part where the surfaces with more charges present stronger attraction to K^+.

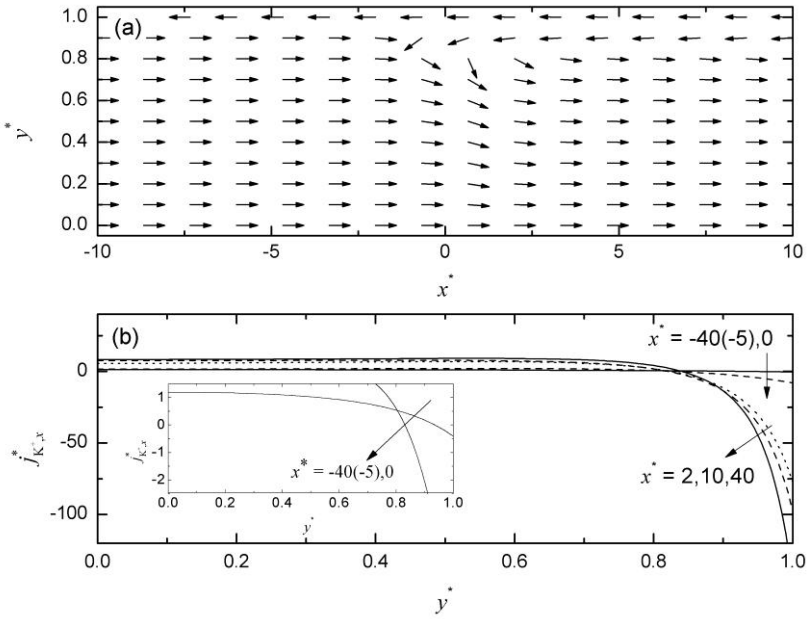

Fig. 6.15. Flux density of K^+ at t^* = 4500. a) normalized flux density near the midsection, and b) streamwise flux density along cross sections.

6.6.5 Positions of Concentration Plugs

Fig. 6.16 plots the location of the concentration plugs of H^+ and K^+. The location is referred to as somewhere along the downhill/uphill side of H^+/K^+ so that $\frac{\partial^2 c_i^*}{\partial x^{*2}} = 0$. The slight difference of the curves is attributed to the definition of the location, but generally, the concentration plugs should always be at the same position since their propagation is at the same pace. It is shown from the figure that it takes as long as about 275HRT for the concentration plugs to travel through the channel. The reason for such a long time is that the feed of H^+ from the downstream well is quite slow comparing to the storage capacity of protons in the channel. It is also noted that the propagation rate, i.e. the slope of the curves, is relatively large in the upstream half channel and drops to only one sixth or so in the

downstream half channel. The difference is mainly related to the transient of surface charges. Because the surfaces at the downstream part are releasing protons to provide additional supply of H^+, the transit region absorbs H^+ with a larger flux while locating at the upstream half channel. When the concentration plugs arrive at the downstream half part where the surfaces are more charged, extra H^+ are needed to neutralize surface charges.

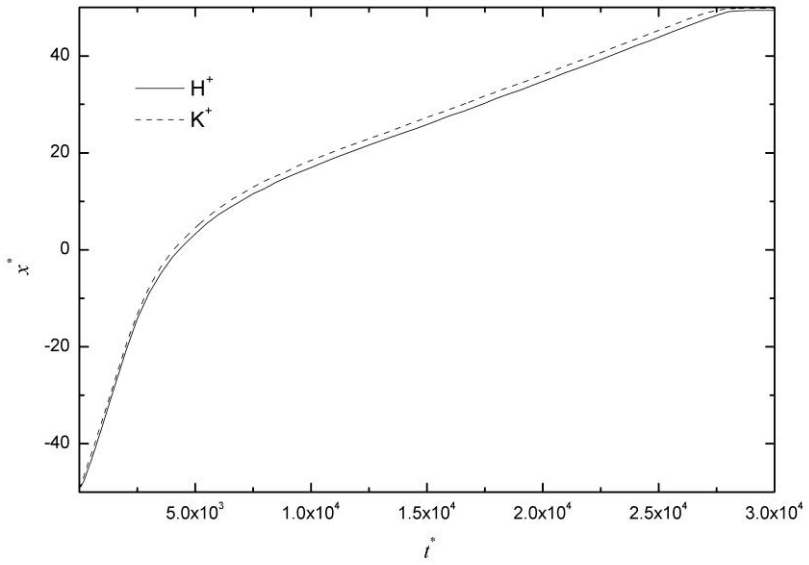

Fig. 6.16. Location of concentration plugs

As far as we know, such a long time to establish the steady state flow within an overlapped EDL has never been reported before. This conclusion has profound impact on real applications of the electrokinetic flow with overlapped EDLs. For instance, dilute KCl solution was driven through a channel of 75 nm high and 4.5 mm long under the pressure bias of 0.4 MPa in the past experiments [6]. Such a flow has HRT of 98 seconds, the transient process can maintain a few hours if the same time of 275 HRT is assumed to achieve its steady state.

6.6.5 Electroviscous Effect

The electroviscous effect results from the streaming potential which drives counterions against the bulk flow, causing additional flow friction. To evaluate the transient of electroviscous effect, Fig. 6.17 presents the scaled flow rate of the electrokinetic flow with the consideration of the EDL effects with respect to time, against the Poiseuille flow with no EDL effects in the same computation domain. The Poiseuille flow was simulated by solving only the NS equation. Under the pressure difference of $3\mu LU/H^2$, the steady Poiseuille plate flow has the flow rate of UH or $Q^* = 1$. The simulation results show the Poiseuille flow has $Q^* = 0.984$ at steady state, which is slightly less than 1 because minor pressure loss at the channel ends.

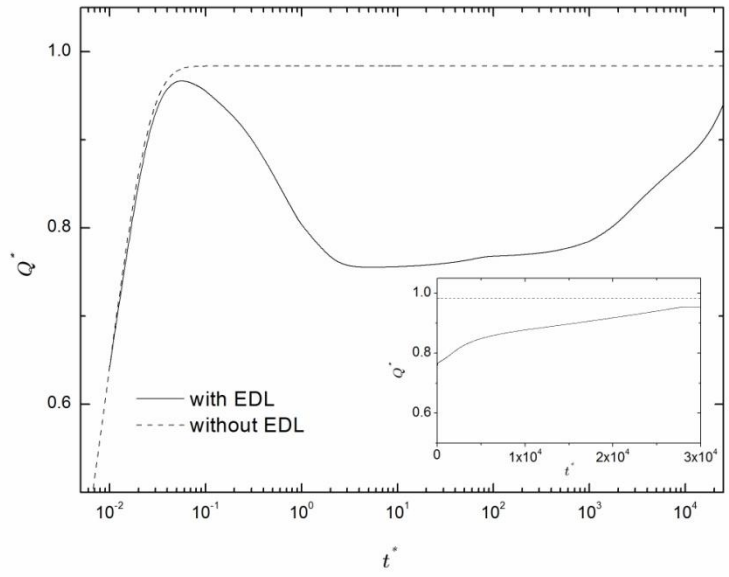

Fig. 6.17. Variation of the flow rate through the channel

The transient of the flow rate of the electrokinetic flow can be divided into three stages. First, the flow rate rapidly increases as $t^* < 0.05$. The transient behavior agrees well with what is for the Poiseuille flow, because the streaming potential is not sufficiently

strong to cause an significant friction increase. Second, Q^* rapidly decreases to its minimum value of 0.76 in the period of $0.05 < t^* < 11$. At the same time, the Poiseuille flow has already achieved its steady state. The flow friction quickly increases accompanying the establishment of the steaming potential. At $t^* = 11$ when the streaming potential reaches its maximum, the electroviscous effect is the strongest and the flow rate is reduced by 23%. Finally, the flow rate is slowly back up for $11 < t^* < 27500$. The electrokinetic flow is only 3% slower than the Poiseuille flow at the steady state when the electroviscous effect becomes negligible.

It should be stressed that the increase of flow rate in $11 < t^* < 27500$ is quite slow. The inset of Fig. 6.17 demonstrates that the change of the flow rate in the last period has the similar tendency as the propagation of concentration plugs plotted in Fig. 6.16. The similarity is mainly because the steady state distribution of ions replaces the initial Boltzmann distribution step by step, accompanying with the plug-like concentration propagation. As a consequence, the flow friction decreases in the region that the replacement completes, as the streamwise electrical body force is significantly reduced due to the decrease of spatial charge density and the streamwise potential gradient. The overall flow friction consists of the ones before and behind the concentration plugs, and decreases in proportion to the propagation. Therefore, the change of the flow rate is strongly dependent on the location of the concentration plugs.

6.7 Time Scale Analysis

Numerical results in the last section show that the time to achieve steady state is as long as 275HRT, and that the EDL structure becomes quite different from Boltzmann distribution. The transient is mainly featured by the downstream propagation and the upstream extension. However, the transient features can be apparently different under some special cases, such as an extremely slow flow in which the EDL structure should approach Boltzmann distribution as the influence of the flow is negligible. In this section, we perform time scale analysis of ion transport to classify the transient behavior of electrokinetic flows.

6.7.1 Time Scale of the NP Equation

In a two-dimensional channel with *x* direction parallel to the walls and *y* direction normal to the walls, the salt solution flows along *x* direction. Ion transport is govern by the NP equation. Substituting the continuity equation of Eq. (3-1) into the NP equation of Eq. (3-4), yields

$$\frac{\partial c_i}{\partial t} + u\frac{\partial c_i}{\partial x} = D_{\mathrm{i}}\left(\frac{\partial^2 c_i}{\partial x^2} + \frac{\partial^2 c_i}{\partial y^2}\right) + \frac{z_i F D_i}{RT}\left[\frac{\partial}{\partial x}\left(c_{\mathrm{i}}\frac{\partial \psi}{\partial x}\right) + \frac{\partial}{\partial y}\left(c_{\mathrm{i}}\frac{\partial \psi}{\partial y}\right)\right] \tag{6-27}$$

The electric potential can be treated as the combination of its two components

$$\psi(x,y) = \varphi(x,y) + \phi(x) \tag{6-28}$$

where φ is the transverse component referenced to the channel center, i.e. $\varphi(x,0) = 0$, and $\phi(x)$ is the streamwise component, which is constant along every cross section.

Substituting Eq. (6-28) into Eq. (6-27) yields

$$\frac{\partial c_i}{\partial t} + u\frac{\partial c_i}{\partial x} = D_{\mathrm{i}}\left(\frac{\partial^2 c_i}{\partial x^2} + \frac{\partial^2 c_i}{\partial y^2}\right) + \frac{z_i F D_i}{RT}\left[\frac{\partial}{\partial x}\left(c_{\mathrm{i}}\frac{\partial \phi}{\partial x}\right) + \frac{\partial}{\partial x}\left(c_{\mathrm{i}}\frac{\partial \varphi}{\partial x}\right) + \frac{\partial}{\partial y}\left(c_{\mathrm{i}}\frac{\partial \varphi}{\partial y}\right)\right] \tag{6-29}$$

To normalize Eq. (6-29), we use the following parameters, which are of order unity,

$$\overline{t} = \frac{t}{t_0}, \overline{u} = \frac{u}{U}, \overline{c_i} = \frac{c_i}{c_{i,\infty}}, \overline{x} = \frac{x}{L}, \overline{y} = \frac{y}{H}, \overline{\phi} = \frac{\phi}{\phi_0}, \overline{\varphi} = \frac{\varphi}{\zeta} \tag{6-30}$$

where t_0 is the characteristic time scale, U the characteristic velocity, ϕ_0 the potential difference between channel ends. With the substitution of Eq. (6-30), Eq. (6-29) is rewritten as

$$\alpha \frac{\partial \overline{c_i}}{\partial \overline{t}} + \mathrm{ReSc}_i \xi \overline{u} \frac{\partial \overline{c_i}}{\partial \overline{x}} =$$

$$\xi^2 \frac{\partial^2 \overline{c_i}}{\partial \overline{x}^2} + \frac{\partial^2 \overline{c_i}}{\partial \overline{y}^2} + \beta\gamma\xi \frac{\partial}{\partial \overline{x}}\left(\overline{c_i} \frac{\partial \overline{\phi}}{\partial \overline{x}}\right) + \beta\xi^2 \frac{\partial}{\partial \overline{x}}\left(\overline{c_i} \frac{\partial \overline{\varphi}}{\partial \overline{x}}\right) + \beta \frac{\partial}{\partial \overline{y}}\left(\overline{c_i} \frac{\partial \overline{\varphi}}{\partial \overline{y}}\right) \tag{6-31}$$

Here, $\xi = H/L$, $\alpha = H^2/t_0 D_i$, $\beta = z_i F\zeta/RT$, and $\gamma = \phi_0 H/\zeta L$. β is mainly related to surface properties. γ represents the ratio of the streamwise electric field strength to the transverse one, which is related to the flow rate and the EDL structure. Time scale of each transport component is given by comparing their coefficients with α. For example, the convection (the second term in the LHS) has a time scale of L/U using $\alpha \sim \mathrm{ReSc}_i\xi$. The terms in the RHS represent streamwise diffusion, transverse diffusion, major streamwise electromigration, minor streamwise electromigration and transverse electromigration with time scales of $\frac{L^2}{D_i}$, $\frac{H^2}{D_i}$, $\frac{RTL^2}{z_i F \phi_0 D_i}$, $\frac{RTL^2}{z_i F \zeta D_i}$, and $\frac{RTH^2}{z_i F \zeta D_i}$, respectively.

All the derivatives in Eq. (6-31) are basically no more than unity in the majority of the channel. Particularly, $\frac{\partial}{\partial \overline{y}}\left(\overline{c_i} \frac{\partial \overline{\varphi}}{\partial \overline{y}}\right)$ is of unity order in the EDL, or throughout the channel in which the EDLs are overlapping. The only exceptions are $\frac{\partial^2 \overline{c_i}}{\partial \overline{x}^2}$ and $\frac{\partial}{\partial \overline{x}}\left(\overline{c_i} \frac{\partial \overline{\phi}}{\partial \overline{x}}\right)$ in the transit region where they could be much larger than unity as discussed later.

The orders of the coefficients in Eq. (6-31) vary among $\mathrm{ReSc}_i\xi$, ξ^2 and 1. In typi-

cal electrokinetic flows in an approximately infinitely long nanochannel, $\beta \sim 1$[9], $\xi << 1$, $Sc_i = 400 \sim 1000$, $Re = 10^{-5} \sim 10^{-3}$, and $\xi << ReSc_i << 1/\xi$. $\beta\gamma\xi$ must be at the same order as $ReSc_i\xi$, because the major electromigration is the one to balance the convection along the flow direction. The order of α depends on the characteristic time on which the transport is investigated. Hence, the coefficients comply with $\xi^2 \sim \beta\xi^2 << ReSc_i\xi \sim \beta\gamma\xi << \beta \sim 1$ under the condition of $\xi << ReSc_i << 1/\xi$.

6.7.2 Transverse Equilibrium

If only taking the terms with highest orders of 1, Eq. (6-31) is reduced to

$$\alpha \frac{\partial \overline{c}_i}{\partial \overline{t}} = \frac{\partial^2 \overline{c}_i}{\partial \overline{y}^2} + \beta \frac{\partial}{\partial \overline{y}} \left(\overline{c}_i \frac{\partial \overline{\varphi}}{\partial \overline{y}} \right) \tag{6-32}$$

which indicates that ion distribution along the transverse direction is mainly governed by electromigration and diffusion, and the equilibrium is established at the time scale of H^2/D_i, which is 5 μs for the previous numerical simulation. If ion transport is examined at a much larger time scale such that $\alpha << 1$, Eq. (6-32) can be expressed as

$$0 \cong D_i \frac{\partial^2 c_i}{\partial y^2} + \frac{z_i F D_i}{RT} \frac{\partial}{\partial y} \left(c_i \frac{\partial \varphi(x,y)}{\partial y} \right) \tag{6-33}$$

The transverse equilibrium is at quasi-steady. The solution of Eq. (6-33) with the boundary conditions $\varphi(x,0) = 0$ and $c_i(x, y, t) = c_{i,c}(x, t)$ is given by Eq. (3-9)

$$c_i(x, y, t) = c_{i,c}(x, t) \exp\left[-\frac{z_i F}{RT} \varphi(x, y) \right] \tag{6-34}$$

$c_{i,c}(x, t)$ is the concentration of ith ion at the channel center, accounting for the contribution of other transport components. Eq.(6-34) has been widely used to model concentration profiles as we did for steady state flow in an infinitely long channel in Chapter 4 and also surveyed in Chapter 2.

6.7.3 Streamwise Transport

Electrokinetic flows of salt solutions may lead to a large change of ion distribution as suggested by the simulation results. Although all streamwise transport terms are not as strong as the transverse terms at the steady state, they play an critical role to the transient behavior.

According to the analysis of Eq. (6-31), the convection and major electromigration has the second highest order of $\mathrm{ReSc}_i\xi$, but still larger than the lowest order of ξ^2. Thus, the streamwise transport is mainly governed by the convection and major electromigration with the time scale of L/U, which is equal to 50 μs for the previous numerical simulation. The balance of the two major streamwise transports are simply guaranteed by $\frac{\partial c_\mathrm{i}}{\partial x} \cong 0$ and $\frac{\partial^2 \phi}{\partial x^2} \cong 0$. Thus, ion distribution and the electric field maintain uniform along the streamwise direction in the channel, except in the transit region.

The transit region is a narrow region, similar to a shock in which large variation of ion concentrations occurs. To illustrate ion transport in the transit region with a width of ΔL, Eq. (6-31) is rescaled as

$$\alpha \frac{\partial \overline{c}_i}{\partial \overline{t}} + \mathrm{ReSc}_\mathrm{i}\xi'\overline{u}\frac{\partial \overline{c}_i}{\partial \overline{x}'} =$$

$$\xi'^2 \frac{\partial^2 \overline{c}_i}{\partial \overline{x}'^2} + \frac{\partial^2 \overline{c}_i}{\partial \overline{y}^2} + \beta\gamma'\xi' \frac{\partial}{\partial \overline{x}'}\left(\overline{c}_i \frac{\partial \overline{\phi}'}{\partial \overline{x}'}\right) + \beta\xi'^2 \frac{\partial}{\partial \overline{x}'}\left(\overline{c}_i \frac{\partial \overline{\varphi}}{\partial \overline{x}'}\right) + \beta \frac{\partial}{\partial \overline{y}}\left(\overline{c}_i \frac{\partial \overline{\varphi}}{\partial \overline{y}}\right) \quad (6\text{-}35)$$

where $\xi' = H/\Delta L$, $\overline{x}' = x/\Delta L$, $\gamma' = \phi_0' H/\zeta \Delta L$, and $\overline{\phi}' = \phi/\phi_0'$. ϕ_0' is the streamwise potential difference across the transit region. Other dimensionless parameters are defined in Section 6.7.1. This treatment makes all the derivatives are at the same order, so that the terms can be compared by focusing on the coefficients.

Diffusion and convection along the streamwise direction are two of the leading transport terms in the transit region. They must be at the same order because convection triggers the change of ion distribution, while the streamwise diffusion is the one to balance the convection in this region. It yields $\mathrm{ReSc}_i \xi' \sim \xi'^2$, further leading to $\Delta L \sim H/\mathrm{ReSc}_i << L$ if recalling the assumption of $\mathrm{ReSc}_i >> \xi$. It should be noted that Eq.(6-34) is no longer a description for ion distributions in the transit region because the transverse terms are not the only major contributions. Ion distributions must be modeled in a 2-D space instead.

As a summary of the analysis of the streamwise transport, Ions are almost uniformly distributed along the streamwise direction in the majority of the channel, but abruptly vary in a narrow region under the condition of $H/L << \mathrm{ReSc}_i << L/H$. The analysis is in accordance with the presence of concentration plugs in the previous simulation. Moreover, ion distributions are at quasi-steady state in the channel, including the transit region, if the transient is considered at a time scale as large as the hydraulic retention time of L/U.

6.7.4 Other Types of Electrokinetic Flows

The above scale analysis is applied for electrokinetic flows under the condition of $H/L << \mathrm{ReSc}_i << L/H$. The key feature is the presence of the transit region, and the quasi-steady state in the channel. Next, we qualitatively examine ion distributions of other electrokinetic flows that the condition of $H/L << \mathrm{ReSc}_i << L/H$ is not satisfied.

When ReSc_i is less than H/L by orders, convection is too small to induce a considerable streaming potential field. Ion distributions are not able to significantly deviate from Boltzmann distribution in this case. Salt solutions can be treated as being at rest,

without the influence of trivial convection.

If the flow is rather slow, or the channel is relatively short such that $\mathrm{ReSc}_i \sim H/L$, the streamwise diffusion is at the same level as the convection and the major electromigration. It seems that the transit region fully extends to cover the whole channel, or the end effects has strong influence on the channel. Hence, ion concentrations significantly vary along the flow direction ($\frac{\partial c_i}{\partial x} \neq 0$), and the streamwise electric field is no longer uniform ($\frac{\partial^2 \varphi}{\partial x^2} \neq 0$ and $\frac{\partial^2 \phi}{\partial x^2} \neq 0$). This is a quite different scenario from the previous simulation, as the concentration plugs likely disappear.

When $\mathrm{ReSc}_i >> L/H$, convection and electromigration along the streamwise direction become the dominating terms. This situation may exist when the flow flushes over short nanopores. When the sudden flow is added, counterions start to circulate in the channel. The circulation is so strong as to completely mix ions which will quickly achieve uniform distribution. When the flow is at steady state, the EDL effects are negligible as the internal electric field due to surface charges is too small to have significant influence on the flow as well as ion distribution in the channel.

For electrokinetic flows with $\mathrm{ReSc}_i \sim L/H$, the convection is at the same order as the transverse diffusion, and the streaming potential field is as strong as the internal electric field. The electroneutrality condition along the cross section is not valid due to the influence of the strong streaming potential field. There is no transverse quasi-steady state during the transient. The mixing behavior seems to have strong influences on the transient, but is left to the future study.

6.8 Approximate Solution for Concentration Plug Propagation

6.8.1 Basic Concept

It is of importance to estimate how long the steady state will be reached for a specific system. It is anticipatable that the time to achieve the steady state is dependent on a number of factors, including the channel geometry, salt concentration, the bulk pH, surface chemical properties, and the flow conditions. The complete change of the EDL structure due to the added electrokinetic flow may finish in a wide range from a few seconds to as long as a few hours.

A straightforward model is proposed here to quantify the propagation rate, so called the concentration plug transport model. According to the above time scale analysis, there is a narrow transit region in the channel under the condition of $H/L << \mathrm{ReSc}_i << L/H$. The propagation of the concentration plug is the process that the transit region travels downstream. The whole domain is enclosed between two cross sections located at $x = a$ and $x = b$, the channel wall at $y = H$, and the symmetric plane at $y = 0$. The upstream region, the transit region, and the downstream region are sketched in sequence in Fig. 6.18, and separated by dash lines.

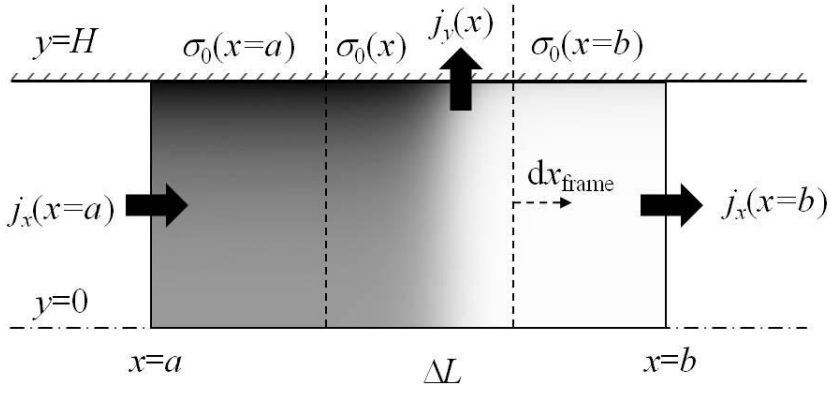

Fig. 6.18. Sketch of concentration plug transport model

In the upstream and downstream regions, we assume (i) negligible streamwise concentration variation such that $\frac{\partial c_i}{\partial x} = 0$, (ii) uniform streamwise electrical field such that $\frac{\partial}{\partial x}\left(\frac{\partial \phi}{\partial x}\right) = 0$ and $\frac{\partial \varphi}{\partial x} = 0$, (iii) no proton exchange through the surface such that $N_{\mathrm{H}^+} = 0$, and (iv) constant surface charge density along the streamwise direction, i.e. $\frac{\partial \sigma_0}{\partial x} = 0$. These assumptions are in accordance with the time scale analysis and also the previous simulation. They extremely simplify the NP equation, the Poison equation and the relevant boundary conditions at surfaces, making it possible to obtain an analytical solution. In contrast, the electric field and concentration profiles sharply change in both the streamwise and the transverse directions in the transit region. It is formidable to obtain an analytical solution there.

When the transit region travels downstream in a finite channel, the upstream region extends, while the downstream region shrinks. Because the propagation is very slow comparing to transverse equilibrium in the bulk and proton exchange on surfaces, the EDL structure is at quasi state, which is treated as stationary in each region.

The concentration plug transport model quantifies the propagation rate through modeling the transport phenomena in the upstream and downstream region. According to the species conservation law, the species that enters the transit region from the neighbored regions is stored in the transit region including in the fluid and on the surface.

6.8.2 Approximate Solution

The propagation rate of concentration plugs is mainly restricted by the limited supply rate of protons comparing to the relative large storage capacity of protons in the

channel. Transport and storage of hydronium ions are focused in this subsection to determine the propagation rate.

In a nanochannel with an overlapped EDL, the generation rate of H^+ due to water dissociation is much smaller than its transport so that the source term in Eq. (3-14) can be ignored, and the integral of Eq. (3-14) within the domain sketched in Fig. 6.18 is given by

$$H\left[\frac{\mathrm{d}\int_a^b \langle c_{H^+}\rangle dx}{\mathrm{d}t} + \langle N_{H^+}\rangle|_{x=a} + \langle N_{H^+}\rangle|_{x=b}\right] + \int_a^b N_{H^+}\mathrm{d}x\Big|_{y=0} + \int_a^b N_{H^+}\mathrm{d}x\Big|_{y=H} = 0 \quad (6\text{-}36)$$

where $\langle \quad \rangle = \int_0^1 \mathrm{d}y^*$, denotes the average quantity along the cross section. All terms in Eq.(6-36) are evaluated for the propagation through an infinitesmal distance of $\mathrm{d}x_{\mathrm{plug}}$ over a time span of dt. With the assumption that the transit region is unchanged in geometry, the upstream one extends by $\mathrm{d}x_{\mathrm{plug}}$ and the downstream one contracts by the same length.

If the EDL structure of each region is stationary**,** the change of H^+ numbers in the domain is associated with the change of the geometry of the upstream and downstream regions, yielding

$$\mathrm{d}\int_a^b \langle c_{H^+}\rangle \mathrm{d}x = -\mathrm{d}x_{\mathrm{plug}}\langle c_{H^+}\rangle|_{x=a}^{x=b} \quad (6\text{-}37)$$

If the potential field is defined by Eq.(6-28), the outward flux density at $x = a$ is obtained by the combination of Eq. (6-7) and Eq. (6-15) as

$$N_{H^+}|_{x=a} = -uc_{H^+} + D_{H^+}\frac{\partial c_{H^+}}{\partial x} + \frac{FD_{H^+}c_{H^+}}{RT}\left(\frac{\partial \phi}{\partial x} + \frac{\partial \varphi}{\partial x}\right) \quad (6\text{-}38)$$

With the assumption of $\frac{\partial c_{H^+}}{\partial x} = 0$ and $\frac{\partial \varphi}{\partial x} = 0$ in the upstream region, Eq. (6-38) can be integrated along $x = a$ to yield the average outward flux at the entrance of the domain,

$$\langle N_{\mathrm{H}^+}\rangle|_{x=a} = -J_{\mathrm{H}^+}|_{x=a} \tag{6-39}$$

where $J_{\mathrm{H}^+} = \langle u c_{\mathrm{H}^+} - \frac{F D_{H^+} c_{H^+}}{RT}\frac{\partial \phi}{\partial x}\rangle$ is the flux of H^+ across the channel.

The average outward flux at $x = b$ is derived in a similar way, yielding

$$\langle N_{\mathrm{H}^+}\rangle|_{x=b} = J_{\mathrm{H}^+}|_{x=b} \tag{6-40}$$

The different signs of the bracketed terms in Eq. (6-39) and (6-40) are because two surfaces at $x = a$ and at $x = b$ are in the opposite direction.

Due to the symmetric condition, there is no proton exchange at $y = 0$, yielding

$$\int_a^b N_{\mathrm{H}^+}\mathrm{d}x\Big|_{y=0} = 0 \tag{6-41}$$

The outward flux through the wall at $y = H$ is related to the change rate of surface charge density via. Eq. (6-16)

$$\int_a^b N_{\mathrm{H}^+}\mathrm{d}x\Big|_{y=\mathrm{H}} = \frac{\mathrm{d}\int_a^b \sigma_0 \mathrm{d}x}{F\mathrm{dt}} \tag{6-42}$$

Because surface charge density is assumed to be constant in the upstream and downstream regions, the change of total surface charge is caused by the change of the geometry of the upstream and downstream regions, yielding

$$\mathrm{d}\int_a^b \sigma_0 \mathrm{d}x = -\mathrm{d}x_{\mathrm{plug}}\,\sigma_0|_{x=a}^{x=b} \tag{6-43}$$

Combining with Eqs. (6-37) and (6-39)-(6-43), Eq.(6-36) can be rewritten as,

$$-\frac{\mathrm{d}x_{\mathrm{plug}}}{\mathrm{d}t}\left(\langle c_{\mathrm{H}^+}\rangle + \frac{\sigma_0}{HF}\right)\Big|_{x=a}^{x=b} + J_{\mathrm{H}^+}|_{x=a}^{x=b} = 0 \tag{6-44}$$

where the second term represents proton exchange with the environment, and the first term is the storage of protons in the channel, either as free ions in the bulk solution or as components bounded with silanol groups.

Rearranging Eq. (6-44) yields the propagation rate u_{plug} as

$$u_{\mathrm{plug}} = \frac{\mathrm{d}x_{\mathrm{plug}}}{\mathrm{d}t} = \frac{\Delta J^*_{\mathrm{H}+}}{\Delta\langle c^*_{\mathrm{H}+}\rangle + \frac{\varepsilon_0 \varepsilon RT}{F^2 H^2 c_{\mathrm{H}+,\infty}} \Delta\sigma^*_0} U \tag{6-45}$$

where $\Delta J^*_{\mathrm{H}+} = J^*_{\mathrm{H}+}\big|^{x=b}_{x=a}$, $\Delta\langle c^*_{\mathrm{H}+}\rangle = \langle c^*_{\mathrm{H}+}\rangle\big|^{x=b}_{x=a}$ and $\Delta\sigma^*_0 = \sigma^*_0|^{x=b}_{x=a}$. The propagation rate is estimated without knowing the structure of the transit region. In order to evaluate u_{plug}, the quantities of Eq. (6-45) should be determined with some assumptions.

First, we assume the EDL structure in the upstream region is the same to that at the steady flow state, which has already been modeled in Chapter 5, and the corresponding analytical solutions of these quantities are listed in Table 6.3. This assumption is in good agreement with the previous simulation results. The total flux of H^+ across $x = a$ is also ignored. or there is no proton exchange between the transit and upstream regions.

Table 6.3. Determination of quantities in the approximate solution

Quantity	$x = a$	$x = b$
$c^*_{\mathrm{H}^+}$	Eq. (5-2)	Eq. (6-24)
φ^*	Eq. (5-5)	Eq. (6-23)
σ^*_0	Eq. (5-9)	Eq. (6-26)
$u^*(u = u_p + u_e)$	/	Eqs. (5-13) and (5-14)
$\frac{\partial \phi^*}{\partial x^*}$	/	Eq. (5-20)
$J^*_{\mathrm{H}^+}$	0	Eq. (5-12)

Second, it is assumed that the EDL structure in the downstream region is at electrostatic equilibrium. The transient of surface charge and ion distributions in the downstream region are ignored. According to the simulation results, the assumption is valid only at the early/middle stage. At the late stage, ion distributions gradually deviate from Boltzmann distribution, leading to a significant modeling error.

Finally, the streamwise potential field in the downstream region is assumed to be constant throughout the late stage, and its value is given by assuming the species flux conservation of K^+. The streaming potential is obtained by solving Eq. (5-20) based on Boltzmann distribution. The bulk velocity is next solved by substituting the streaming potential into Eqs. (5-13) and (5-14). The total flux of H^+ across $x = b$ is estimated by substituting u^* and $\frac{\partial \phi^*}{\partial x^*}$ into Eq. (5-12) with the assumption of Boltzmann distribution of H^+.

With the above assumptions, all quantities in Eq.(6-45) are independent of time so that the concentration plug of H^+ propagates at a constant rate. The flow reaches its steady state once the concentration plug arrives at the exit of the channel. Thus, the time required for reaching the steady flow is given by

$$t_s = \frac{L}{u_{\text{plug}}} = \frac{\Delta\langle c^*_{\text{H}+}\rangle + \frac{\varepsilon_0 \varepsilon RT}{F^2 H^2 c_{\text{H}^+,\infty}} \Delta\sigma^*_0}{\Delta J^*_{\text{H}+}} \frac{L}{U} \tag{6-46}$$

where t_s is proportional to the HRT.

6.8.3 Estimation for the Propagation Rate

Electrokinetic flows of various salt solutions though a channel with H of 10 nm and of 100 nm were calculated. The calculations used the same parameters as the previous

simulation. Fig. 6.19 plots t_s/HRT for salt solutions of 10^{-4} ~ 1mM with the pH at 7. t_s/HRT is almost linearly dependent on salt concentration for a given channel under conditions of EDL overlap. t_s could be larger than the HRT by a few order of magnitude. Such a large time scale has never been reported in the literature. The time scale was usually suggested as the HRT or a few times the HRT [25, 44].

t_s varies in a wide range in real applications. For example, in the experiment reported in [6], KCl solution flows through a channel of 75 nm high and 4.5 mm long under the pressure bias of 0.4 MPa. Though the HRT is only 97.7 seconds, t_s estimated from the approximate solution are as long as 0.75 and 7.9 hours for 0.01 mM and 0.1 mM solutions, respectively. Had the channel been shortened to 45 μm with the corresponding HRT of 0.0977 seconds, such as in nanopores, the steady state flow will be achieved in less than a few seconds.

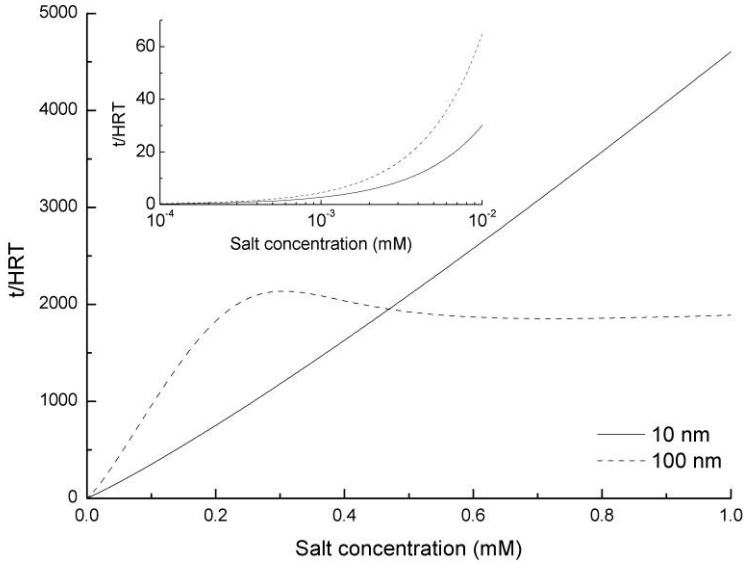

Fig. 6.19. t_s^* as a function of salt concentration.

t_s is mainly related to the flux of protons absorbed from the downstream reservoir, as well as the storage capacity of protons in the channel. The dimensionless flux is evaluated by $-\Delta J^*_{\mathrm{H}^+}$, while the dimensionless storage of protons in the solution and on the surface is characterized by $-\Delta\langle c^*_{\mathrm{H}^+}\rangle$ and $-\frac{\varepsilon_0 \varepsilon RT}{F^2 H^2 c_{\mathrm{H}^+,\infty}}\Delta\sigma_0^*$, respectively. These quantities are plotted in Fig. 6.20 and Fig. 6.21 for electrokinetic flows of various salt solutions in the channel with *H* of 100 nm.

Fig. 6.20 demonstrates that the dimensionless flux of H^+ increases in lower salt solutions, because H^+ is more enriched with a more overlapped EDL at static equilibrium. It should be noted that the flux of H^+ from the downstream reservoir is mainly affected by the end effects. Information at the interface between the channel and the reservoir, including distribution of hydronium ions, the bulk flow field, and the electric field, determines the flux of H^+. Generally, the flux of H^+ slightly increases with respect to time during the late stage. Constant flux of H^+ assumed in the model is not a precise description, but the assumption make it possible to roughly estimate the flux by avoiding the complex exit effects.

Fig. 6.21 suggests that most newly added protons are adsorbed to the surfaces except on extremely dilute salt solution. For instance, for 0.01 mM KCl solution, 83% of protons are bound to the surfaces and only 17% are left in fluid. The store capacity could be larger than net flux of proton by a few orders of magnitude for salt solutions of around 0.1mM, leading to the corresponding t_s/HRT as large as thousands. It means that the feed of protons is so slow that the concentration plug propagates at a small rate.

The storage capacity of a nanochannel results from the difference of the EDL

structure at static equilibrium and at steady flow equilibrium. In an extremely dilute solution, no additional protons can be stored in the channel when the fluid changes from static state to steady state flow. It is in consistence with the analysis of salt-free water in Chapter 3 that the EDL structure is not dependent on the flow status. When the EDL overlap effects is lack in a salt regime of higher than 1mM(κH > 10), the storage capacity decreases to nearly zero as well, because the EDL structure is unchanged by the flow in this case as we described in Chapter 5.

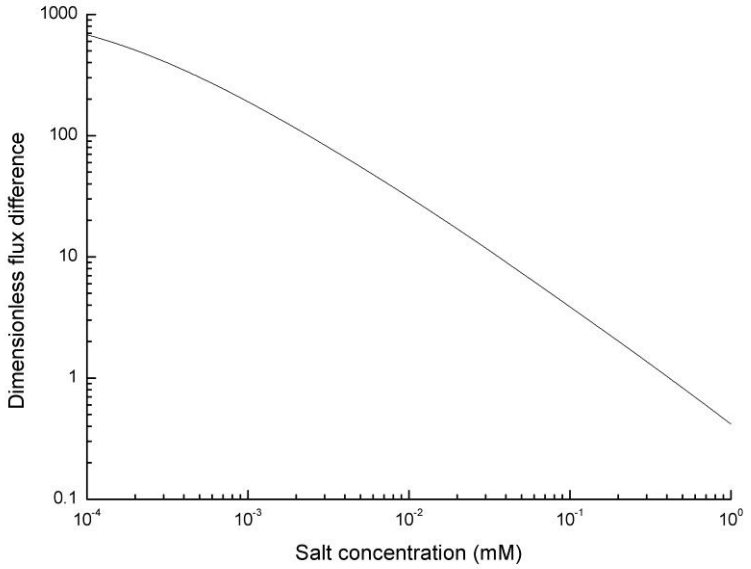

Fig. 6.20. Net flux of H^+ across the transit region in the channel of H = 100 nm.

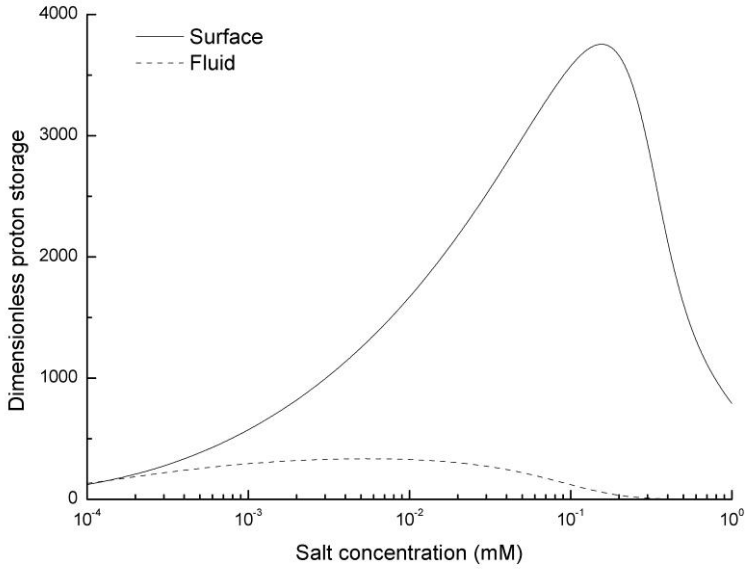

Fig. 6.21. Storage of protons in the channel of H = 100 nm.

6.8.4 Comparison between Estimation and Simulation Results

The approximate solution for the time to reach steady state is only a rough estimation. Under the condition of the previous simulation that 0.01 mM KCl solution flow through a nanochannel of H = 100 nm, t_s is estimated as 64 HRT, or t^* = 6400, which is about one fourth of the simulation prediction t^* = 25000. Recalling fast propagation in the upstream half channel as shown in Fig. 6.16, the prediction of the approximate solution has a difference of less than 10%. But in the downstream half channel, the propagation becomes much slower and the approximate solution overestimates the propagation rate by a few times.

The overestimation of the propagation rate in the downstream half channel is caused by two reasons. The first reason is that channel surfaces are more charged in the downstream region. The charge density where the concentration plug meets the downstream region, increases in magnitude since t^* = 2000 and finally doubles its initial value as

shown in Fig. 6.12. With the assumption of constant $\Delta\sigma_0^*$, the approximate solution underestimates the storage capacity of protons on surfaces. It is also because the concentration of H^+ is significantly reduced in the downstream region. The approximate solution further overestimates the upstream electromigration of H^+, or the flux of H^+ entering the transit region. Overall, the assumption of the unchanged EDL structure in the downstream region leads to a great error in the prediction of the propagation rate in the downstream half channel.

6.9 Summary

The research investigates the transient behavior of the pressure-driven flow within an overlapped EDL, particularly with the consideration of proton exchange between silica surfaces and the bulk flow. A flow of 0.01mM KCl solution through a nanochannel with half height H of 100 nm and length L of 10 μm between two large wells was simulated. A deliberate pressure difference was chosen to satisfy the condition of $H/L \ll \mathrm{ReSc}_i \ll L/H$ with which typical electrokinetic flows comply. The Poisson equation, the Nernst-Planck equations, and the Navier-Stokes equations were solved by COMSOL 3.5a using a finite element method. Hydronium, hydroxide, potassium, and chloride ions were involved in the model. The simulation assumed water dissociation equilibrium in the solution and used the single site model for the proton exchange on the channel surfaces. Before applying the pressure difference, the salt solution is at rest and ions follow Boltzmann equilibrium. The simulation results of electrical field, ion concentrations, surface charge density, flux density, and flow rate were presented and discussed.

The flow is divided into three stage, early, middle, and late. In the early stage which lasts about $10H/U$, the streaming potential keeps increasing mainly due to the accumulation of potassium ions at the channel exit, while the EDL structure is unchanged except at the very ends of the channel. The middle stage ends by about $100H/U$. In this stage, chloride ions accompanying with the bulk flow accumulate in the channel. As a result, the concentrations of hydronium, potassium, and chloride ions slightly increase.

The late stage is as long as about $25000H/U$, or 250 times of hydraulic retention time. The EDL structure experiences a large variation from two directions. First, there is a transit region that propagates downstream. The transit region is a narrow region across which there is a large variation of ion concentrations, surface charges, and streamwise electric field. Hydronium ions are sucked into the channel from the downstream reservoir and potassium ions are driven out of the channel exit. A concentration hump of hydronium ions is initially formed near the channel entrance, and then extends downstream like a concentration plug moving forward. Once the transit region passes by, the EDL structure becomes nearly stationary and close to its final steady state, while hydronium ions circulate in the channel. Second, hydronium ions are depleted in the downstream part, and the depletion region extends upstream until meeting with the concentration plug. Accompanying the depletion of hydronium ions, the channel surfaces are firstly releasing protons, and absorb protons in the transit region, and unchanged after the concentration plugs sweep over.

Time scales of ion transport in electrokinetic flows are finally examined. It is concluded that the concentration plug-like propagation exists under the condition of $H/L << \mathrm{ReSc}_i << L/H$. An analytical model is developed to estimate the time required to achieve

steady state, which could be thousands of times larger than the hydraulic retention time in a channel with a half height of 10 nm or 100 nm due to the EDL overlap effects. The analytic model prediction qualitatively agrees with the simulation results.

CHAPTER 7

CONCLUSIONS AND CONTRIBUTIONS

The dissertation investigated that the pressure driven flow through a slit-like silica nanochannel with an overlapped EDL, particularly with the consideration of the coupling effects of surface proton exchange and transport of hydronium ions in the bulk. Comprehensive analytical models have been established for the first time for salt-free water, and for electrolyte solutions with the pressure-driven flow. Numerical simulations were performed to examine the transient behavior of the flow starting from its electrostatic state. Main conclusions and contributions of this dissertation study are summarized as below:

(i) The EDL structure in pure water is self-consistent. Hydronium ions and hydroxide ions follow Boltzmann distribution in the fully-developed steady-state pressure flow and at electrostatic equilibrium, regardless of the EDL overlap. The knowledge provides an ideal reference for studying the EDL structure of dilute salt solutions.

(ii) Counterions are unequally enriched in the steady flow within an overlapped EDL. Hydronium ions are much more enriched than other counterions because hydronium ions with larger mobility are more retained in the channel by the streaming potential. As a consequence of unequal enrichment of counterions, the electrokinetic effects, such as electroviscous effects, streaming potential, surface charges, electrical conductance and so on, are greatly depressed.

In spite of the profound influence of unequal enrichment on the electrokinetic effects, this phenomenon has never drawn attention in the previous studies. This phenomenon clarifies the application of Boltzmann distribution under conditions of EDL overlap.

Boltzmann distribution exists in an electrostatic salt solution, no matter whether the EDLs are overlapped or not, but generally not in the steady flow. It also suggests that the coupling effects of surface dynamic equilibrium and transport of hydronium ions plays a critical role to affecting the EDL structure in the steady flow. It is of importance to consider the coupling effects in modeling for the flows with an overlapped EDL.

(iii) In a strongly overlapped EDL with $\kappa H < \sim 2$, the EDL structure is independent on the change of salt concentration and the pH.

(iv) There is a late stage during the transient electrokinetic flow with an overlapped EDL, at which a concentration hump of hydronium ions initially formed at the channel entrance propagates downstream and a depletion region of hydronium ions extends upstream. The behavior of hydronium ion concentration deeply affects the transient of the EDL structure, such as surface charge and potassium ion concentration. Thus, the Boltzmann distribution is only the intermediate stage shortly after the applied pressure difference, and the EDL structure becomes completely different once experiencing the late stage.

(v) The time required for the electrokinetic flow to reach the steady state might be as long as thousands of times of the hydraulic retention time, dependent on the degree of the EDL overlap, because the feed of hydronium ions from the downstream reservoir is relatively small comparing to the large storage capacity of protons in the channel, either as free ions in the bulk or as part of components on the surfaces. Such slow transient has never been reported before. It partially explains the omission of the transient of the electrokinetic flow within an overlapped EDL in previous studies.

REFERENCES

[1] Eijkel, J. C. T., and van den Berg, A., 2005, "Nanofluidics: What Is It and What Can We Expect from It?," Microfluid. Nanofluid., **1**, pp. 249-267.

[2] Yuan, Z., Garcia, A. L., Lopez, G. P., and Petsev, D. N., 2007, "Electrokinetic Transport and Separations in Fluidic Nanochannels," Electrophoresis, **28**, pp. 595-610.

[3] Baldessari, F., and Santiago, J. G., 2006, "Electrophoresis in Nanochannels: Brief Review and Speculation," J. Nanobiotechnology, **4**(1), p. 12.

[4] Sparreboom, W., van den Berg, A., and Eijkel, J., 2010, "Transport in Nanofluidic Systems: A Review of Theory and Applications," New J. Phys., **12**, p. 015004.

[5] van der Heyden, F. H. J., Bonthuis, D. J., Stein, D., Meyer, C., and Dekker, C., 2006, "Electrokinetic Energy Conversion Efficiency in Nanofluidic Channels," Nano Lett., **6**(10), pp. 2232-2237.

[6] van der Heyden, F. H. J., Bonthuis, D. J., Stein, D., Meyer, C., and Dekker, C., 2007, "Power Generation by Pressure-Driven Transport of Ions in Nanofluidic Channels," Nano Lett., **7**(4), pp. 1022-1025.

[7] Schoch, R. B., Han, J., and Renaud, P., 2008, "Transport Phenomena in Nanofluidics," Rev. Mod. Phys., **80**(3), pp. 839-883.

[8] Park, H. M., Lee, J. S., and Kim, T. W., 2007, "Comparison of the Nernst-Planck Model and the Poisson-Boltzmann Model for Electroosmotic Flows in Microchannels," J. Colloid Interface Sci., **315**, pp. 731-739.

[9] Hunter, R. J., 1981, *Zeta Potential in Colloid Science: Principles and Applications*, Academic Press, New York.

[10] Plecis, A., Schoch, R. B., and Renaud, P., 2005, "Ionic Transport Phenomena in Nanofluidics: Expermimental and Theoretical Study of the Exclusion-Enrichment Effect on a Chip," Nano Lett., **5**(6), pp. 1147-1155.

[11] Berli, C. L. A., 2010, "Output Pressure and Efficiency of Electrokinetic Pumping of Non-Newtonian Fluids," Microfluid. Nanofluid., **8**(2), pp. 197-207.

[12] Conlisk, A. T., 2005, "The Debye-Huckel Approximation: Its Use in Describing Electroosmotic Flow in Micro- and Nanochannels," Electrophoresis, **26**, pp. 1896-1912.

[13] Burgreen, D., and Nakache, F. R., 1964, "Electrokinetic Flow in Ultrafine Capillary Slits," J. Phys. Chem., **68**, pp. 1084-1091.

[14] Behrens, S. H., and Borkovec, M., 1999, "Exact Poisson-Boltzmann Solution for the

Interaction of Dissimilar Charge-Regulating Surfaces," Phys. Rev. E, **60**(6), pp. 7040-7048.

[15] Behrens, S. H., and Borkovec, M., 1999, "Electrostatic Interaction of Colloidal Surfaces with Variable Charge," J. Phys. Chem. B, **103**, pp. 2918-2928.

[16] Behrens, S. H., and Grier, D. G., 2001, "The Charge of Glass and Silica Surfaces," J. Chem. Phys., **115**(14), pp. 6716-6721.

[17] Dutta, P., and Beskok, A., 2001, "Analytical Solution of Combined Electroosmotic/Pressure Driven Flows in Two-Dimensional Straight Channels: Finte Debye Layer Effects," Anal. Chem., **73**, pp. 1979-1986.

[18] Petsev, D. N., 2005, "Theory of Transport in Nanofluidic Channels with Moderately Thin Electrical Double Layers: Effect of the Wall Potential Modulation on Solutions of Symmetric and Asymmetric Electrolytes," J. Chem. Phys., **123**, p. 244907.

[19] van der Heyden, F. H. J., Stein, D., and Dekker, C., 2005, "Streaming Currents in a Single Nanofluidic Channel," Phys. Rev. Lett., **95**, p. 116104.

[20] Stein, D., Kruithof, M., and Dekker, C., 2004, "Surface-Charge-Governed Ion Transport in Nanofluidic Channels," Phys. Rev. Lett., **93**(3), p. 035901.

[21] Ren, Y., and Stein, D., 2008, "Slip-Enhanced Electrokinetic Energy Conversion in Nanofluidic Channels," Nanotechnology, **19**(19), pp. 195707-195707.

[22] Baldessari, F., and Santiago, J. G., 2008, "Electrokinetics in Nanochannels Part I. Electric Double Layer Overlap and Channel-to-Well Equilibrium," J. Colloid Interface Sci., **325**, pp. 526-538.

[23] Wang, M., Chang, C., and Yang, R., 2010, "Electroviscous Effects in Nanofluidic Channels," The Journal of Chemical Physics, **132**, p. 024701.

[24] Wang, M., Kang, Q., and Ben-Naim, E., 2010, "Modeling of Electrokinetic Transport in Silica Nanofluidic Channels," Anal. Chim. Acta, **664**, pp. 158-164.

[25] Kwak, H. S., and Hasselbrink, E. F. J., 2005, "Timescales for Relaxation to Boltzmann Equiblirium in Nanopores," J. Colloid Interface Sci., **284**, pp. 753-758.

[26] Qu, W., and Li, D., 2000, "A Model for Overlapped Edl Fields," J. Colloid Interface Sci., **224**, pp. 397-407.

[27] Ren, C., and Li, D., 2005, "Improved Understanding of the Effect of Electrical Double Layer on Pressure-Driven Flow in Microchannels," Anal. Chim. Acta, **531**, pp. 15-23.

[28] Ren, C. L., and Li, D., 2004, "Electroviscous Effects on Pressure-Driven Flow of Dilute Electrolyte Solutions in Small Microchannels," J. Colloid Interface Sci., **274**, pp.

319-330.

[29] Tessier, F., and Slater, G. W., 2006, "Effective Debye Length in Closed Nanoscopic Systems: A Competition between Two Length Scales," Electrophoresis, **27**, pp. 686-693.

[30] Healy, T. W., and White, L. R., 1978, "Ionizable Surface Group Models of Aqueous Interfaces," Adv. Colloid Interface Sci., **9**, pp. 303-345.

[31] Hiemstra, T., De Wit, J., and Van Riemsdijk, W., 1989, "Multisite Proton Adsorption Modeling at the Solid/Solution Interface of (Hydr) Oxides: A New Approach:: Ii. Application to Various Important (Hydr) Oxides," J. Colloid Interface Sci., **133**(1), pp. 105-117.

[32] Wang, M., and Revil, A., 2010, "Electrochemical Charge of Silica Surfaces at High Ionic Strength in Narrow Channels," J. Colloid Interface Sci., **343**(1), pp. 381-386.

[33] Janssen, K., Hoang, H., Floris, J., De Vries, J., Tas, N., Eijkel, J., and Hankemeier, T., 2008, "Solution Titration by Wall Deprotonation During Capillary Filling of Silicon Oxide Nanochannels," Anal. Chem., **80**(21), pp. 8095-8101.

[34] Schoch, R. B., Bertsch, A., and Renaud, P., 2006, "Ph-Controlled Diffusion of Proteins with Different Pi Values across a Nanochannel on a Chip," Nano Lett., **6**(3), pp. 543-547.

[35] Huang, K.-D., and Yang, R.-J., 2007, "Electrokinetic Behaviour of Overlapped Electric Double Layers in Nanofluidic Channels," Nanotechnology, **18**, p. 115701.

[36] Hughes, B. T., Berg, J. M., James, D. L., Ibraguimov, A., Liu, S., and Temkin, H., 2008, "One-Dimensional Axial Simulation of Electric Double Layer Overlap Effects in Devices Combining Micro- and Nanochannels," Microfluid. Nanofluid., **5**, pp. 761-774.

[37] Wang, M., Chang, C., and Yang, R., 2010, "Electroviscous Effects in Nanofluidic Channels," J. Chem. Phys., **132**, p. 024701.

[38] Choi, Y., and Kim, S., 2009, "Electrokinetic Flow-Induced Currents in Silica Nanofluidic Channels," J. Colloid Interface Sci., **333**(2), pp. 672-678.

[39] Qiao, R., and Aluru, N., 2003, "Ion Concentrations and Velocity Profiles in Nanochannel Electroosmotic Flows," J. Chem. Phys., **118**, p. 4692.

[40] Westall, J., and Hohl, H., 1980, "A Comparison of Electrostatic Models for the Oxide/Solution Interface," Adv. Colloid Interface Sci., **12**(4), pp. 265-294.

[41] Piasecki, W., Zarzycki, P., and Charmas, R., 2010, "Adsorption of Alkali Metal Cations and Halide Anions on Metal Oxides: Prediction of Hofmeister Series Using 1-Pk Triple Layer Model," Adsorption, **16**, pp. 1-9.

[42] Daiguji, H., Yang, P., Szeri, A. J., and Majumdar, A., 2004, "Electrochemomechanical Energy Conversion in Nanofluidic Channels," Nano Lett., **4**(12), pp. 2315-2321.

[43] Davidson, M., and Harvie, D., 2007, "Electroviscous Effects in Low Reynolds Number Liquid Flow through a Slit-Like Microfluidic Contraction," Chem. Eng. Sci., **62**(16), pp. 4229-4240.

[44] Mansouri, A., Scheuerman, C., Bhattacharjee, S., Kwok, D., and Kostiuk, L., 2005, "Transient Streaming Potential in a Finite Length Microchannel," J. Colloid Interface Sci., **292**(2), pp. 567-580.

APPENDICES

APPENDIX A

COMSOL Multiphysics is used as a numerical solver for partial differential equations in Chapter 6. Comsol Multiphysics is an integrated environment for modeling and simulating the problems described by time dependent or stationary second order partial differential equations in one, two, and three dimensions. These equations may be coupled in an almost arbitrary way. In the current simulation, most of the PDEs were modeled by the application model called 'PED, coefficient form'. One advantage of using the coefficient form PDE is to get an arbitrary second order PDE. Steps of setting up COMSOL to model the physics in Chapter 6 are presented in this appendix in order that the beginners of COMSOL are able to repeat the simulation.

A.1 Geometry and Meshing

The 2D geometry was firstly created as sketched in Fig. A.1 after opening a new COMSOL file. The geometry is simply a union of three rectangles. One can easily create such a geometry following the manual, so that the drawing is not presented in details.

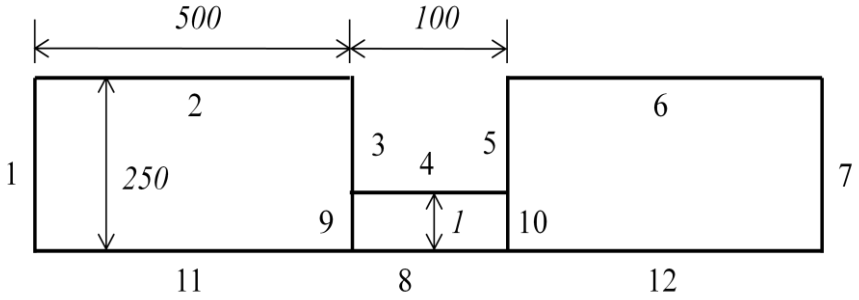

Fig. A.1. Drawing of Geometry

Quadrilateral meshes were first created for the channel, i.e. the subdomain confined

between planes 4, 9, 8 and 10. In the menu of 'Mesh', select 'Mapped Mesh Parameters' to pop up a mesh-setting window. In the window, click 'Boundary', highlight planes 4 and 8 in 'Boundary selection', and click 'constrained edge element distribution' to open up more options. Then input 600 for 'Number of edge elements', 5 for 'Element ratio', Exponential for 'Distribution method', and active 'symmetric'. Next, highlight planes 9 and 10, and input 20 for 'Number of edge elements', 0.1 for 'Element ratio', and Exponential for 'Distribution method'. Finally, click 'Mesh Selected' at the bottom of the window to create quadrilateral meshes which are finer at the surface and ends of the channel, and click 'OK' to close the pop-up window.

Next, unstructured triangular meshes were created for the wells/reservoirs. In the menu of 'Mesh', select 'Free Mesh Parameters' to pop up a window. In the window, first select 'Subdomain', highlight the subdomains that the wells belong to, input 5 for 'Maximum element size', and select 'Triangle (Advancing front)'. Then click 'Mesh Selected' to mesh the wells, and click 'OK' to close the pop-up window.

Total elements include 12000 quadrilateral ones in the channel, as well as 44350 triangular ones in the wells. If the grid needs change, open 'Mapped Mesh Parameters' to remesh quadrilateral meshes and 'Free Mesh Parameters' to remesh triangular meshes.

A.2 Physics Setting

After creating the geometry and meshes, the following steps lead to set up the governing equations and the corresponding boundary and initial conditions in order to solve the problem described in Chapter 6.

A.2.1 Constants and Scalar Expressions

Constants and scalar expressions are first set in COMSOL. They are readable by other types of expressions.

Surface properties, fluid properties, and other physics constants are treated as constants when setting COMSOL. Summarizing them in a single table makes it easier to adjust the values of physical properties. In the menu of 'Options', click 'Constants' to open a window where constants listed in Table A.1 are inputted.

Table A.1. Constants

Name	Expression	Name	Expression
F	96485.3415[C/mol]	CH0	0.0001[mol/m^3]
R	8.431[J/mol·K]	CK0	0.01[mol/m^3]
Av	6.022e23[1/mol]	CCl0	cK0
K	1e-8[mol^2/m^6]	C0	cK0+cH0
e	1.6e-19[C]	DH	9.31e-9[m^2/s]
T	298[K]	DOH	5.28e-9[m^2/s]
rho	1e3[kg/m^3]	DK	1.957e-9[m^2/s]
mu	0.8904e-3[Pa·s]	DCl	2.032e-9[m^2/s]
tau	5e18[1/m^2]	epsilon	78.54*8.854e-12[C/(V*m)]
C	2.9[F/m^2]	H	1e-7[m]
pK	7.5	U	0.1957[m/s]

Scalar Expressions are related to constants. In the menu of 'Options', select 'Expressions/Scalar Expressions' to open a window where scalar expressions listed in Table

A.2 are inputted.

Table A.2. Scalar expressions

Name	Expression	Name	Expression
ScK	mu/(rho·DK)	Re	rho·U·H/mu
ScCl	mu/(rho·DCl)	kappa	F·sqrt(2·C0/(epsilon·R·T))
ScH	mu/(rho·DH)	alpha	C0·R·T/(rho·U^2)
ScOH	mu/(rho·DOH)		

A.2.2 Models

Several variables are about to be solved, including phi standing for electric potential, CH, CK, CCl, and COH for concentrations of H^+, K^+, Cl^-, and OH^- respectively, u and v for velocity components along the *x* and *y* directions, as well as p for pressure.

Before adding models, select 'Expressions/Subdomain Expressions' in the menu of 'Options' to input the expressions listed in Table A.3 for all the subdomains. Expressions presented in Table A.3 are related to local values of variables to be solved. All parameters and variables in those expressions are defined in Table A.1 and Table A.2, except phix and phiy which are self-defined variables by COMSOL, representing the derivative of phi along the *x* and *y* directions.

Some variables are defined for boundary 4 in the similar way. Select 'Expressions/Boundary Expressions' in the menu of 'Options' to open up a new window. And then select boundary 4, input the expressions listed in Table A.4, and click 'OK' to close the window.

The steps below set up the governing equations and the boundary and initial con-

ditions using defined parameters and variables. When adding a model, click 'Multiphysics' to open 'Model Navigator' window. Then select a model and input dependent variables, and click 'Add' to add the model into the geometry.

Table A.3. Subdomain expressions

Name	Expression	Name	Expression
COH	K/CH0^2/CH	rhoe	CK0·(CK-CCl)/C0+(1-CK0/C0)·(cH-cOH)
Fdiff	1+COH·ScH/(CH·ScOH)	Ftime	1+ cOH/cH
Fx	-phix·rhoe·alpha	Fy	-phiy·rhoe·alpha
EMKx	phix /(Re·ScK)	EMKy	phiy /(Re·ScK)
EMClx	phix /(Re·ScCl)	EMCly	phiy /(Re·ScCl)
EMHx	phix·Fdiff/(Re·ScH)	EMHy	phiy·Fdiff/(Re·ScH)

Table A.4. Boundary expressions

Name	Expression
sigma	-e·tau/(1+ CH·CH0·10^(pK -3))
sigma_norm	sigma·H·F/(epsilon·R·T)
proton_exchange	tau/Av·10^(pK-3)·CHt/(H·(1+CH·CH0·10^(pK-3))^2)

1) Poisson equation

In the 'Model Navigator' window, select Poisson equation by clicking 'Application Modes/COMSOL Multiphysics/PDE Models/Classical PDEs/Poisson's Equation', and input 'phi' as its dependent variable.

In the Model Builder ('Model Tree' window at the left on the COMSOL GUI), right-click on 'Poisson's Equation (poeq)' and select 'Subdomain Settings' to set Poisson equation. In the 'Subdomain Settings - Poisson's Equation (poeq)' window, the equation is

expressed as

$$-\nabla \cdot (c\nabla \mathrm{phi}) = f \qquad \text{(A-1)}$$

The coefficients in Eq. (A-1) are set as below: c = 1 and f = (kappa·H)^2·rhoe, and initial values are imposed as phi(t_0) = 0.

In the Model Builder, right-click on 'Poisson equation' again and select 'Boundary Conditions' to set up boundary conditions for Poisson equation. In the pop-up window, click 'Groups', and then 'New' to create a new group. Change the name of the group to 'Reservoir walls', click the symbol of 'Neumann boundary condition', and leave the coefficients of q and g to be their default values 0. Click 'Apply' to set up Neumann condition for this group, meaning electric insulations at the reservoir walls. Repeat the process to create several groups, namely 'Inlet', 'Outlet', 'Channel wall', 'Symmetric', 'Interior'. Among them, the groups of 'Outlet', 'Symmetric', and 'Interior' use Neumann condition with default settings again, while 'Inlet' uses Dirichlet boundary condition with coefficients of q = g = r = 0 and h =1, implying there is grounded at the inlet. Dirichlet boundary condition is also used at 'Channel wall', but with q = 0 and g = sigma_norm to relate local surface charge density to surface proton activity. All elements use the default setting, i.e. Lagrange-Quadratic elements for all governing equations.

In the 'Boundary Conditions' window, select 'Plane 1' in the list of options below 'Boundaries', and then select 'Inlet' from the drop-down menu after clicking 'Group', so that plane 1 is classified as 'Inlet'. In a similar way, let planes 2, 3, 5 and 6 belong in the group of 'Reservoir walls', plane 7 in 'Outlet', Planes 8, 11 and 12 in 'Symmetric', plane 4 in 'Channel wall', Planes 9 and 10 in 'Interior'. The same classification of planes is also applied to the setting of boundary conditions of the remaining models.

2) Momentum equations

In the 'Model Navigator' window, select 'Application Modes/COMSOL Multiphysics/PDE Models/PDE, Coefficient Form', input 'u v p' as its dependent variables, and change the application model name to 'Momentum'. Click 'Add' to add a PDE within Coefficient Form into the geometry, and then click 'OK'.

The governing equation and its initial conditions of the momentum equations can be set in a way similar to the Poisson equation. The coefficient-form PDE is expressed by

$$e_a \frac{\partial^2 \mathbf{u}}{\partial t^2} + d_a \frac{\partial \mathbf{u}}{\partial t} + \nabla \cdot (-c\nabla \mathbf{u} - a\mathbf{u} + \gamma) + \alpha \mathbf{u} + \beta \cdot \nabla \mathbf{u} = f \qquad \text{(A-2)}$$

where, **u** is the variables to be solved. such as [u, v, p] for the momentum equations, and the coefficients are set as below

$$c = \begin{bmatrix} 1/\mathrm{Re} & 0 & 0 \\ 0 & 1/\mathrm{Re} & 0 \\ 0 & 0 & 0 \end{bmatrix},\ a = e_a = \begin{bmatrix} 0 & 0 & 0 \\ 0 & 0 & 0 \\ 0 & 0 & 0 \end{bmatrix},\ d_a = \begin{bmatrix} 1 & 0 & 0 \\ 0 & 1 & 0 \\ 0 & 0 & 0 \end{bmatrix}, f = \begin{bmatrix} Fx \\ Fy \\ 0 \end{bmatrix},$$

$$\alpha = \begin{bmatrix} (0,0) & (0,0) & (-1,0) \\ (0,0) & (0,0) & (0,-1) \\ (1,0) & (0,1) & (0,0) \end{bmatrix},\ \beta = \begin{bmatrix} (u,v) & (0,0) & (0,0) \\ (0,0) & (u,v) & (0,0) \\ (0,0) & (0,0) & (0,0) \end{bmatrix},\ \gamma = \begin{bmatrix} -ux/\mathrm{Re} & -vx/\mathrm{Re} \\ -uy/\mathrm{Re} & -vy/\mathrm{Re} \\ 0 & 0 \end{bmatrix}.$$

All parameters in 'Init' are imposed as zero. If the time-dependent terms are not in existence in Eq. (A-2), select 'Solve /Solver Parameter' to open a 'Solver Parameters' window where the solver changes from 'Stationary' to 'Time dependent'. The time-dependent terms will appear in the window of 'Subdomain Settings'.

In the Model Builder, right-click on 'PDE, Coefficient Form(Momentum)' and select 'Boundary Conditions' to set up boundary conditions for the momentum equations. For the group of 'Reservoir walls' and 'Channel wall', select Dirichlet boundary condition and let q = g = h = r = 0, but impose '-u -v 0' for 'constr' below 'Weak' to adapt the no-slip

boundary conditions. For the group of 'Inlet', set Dirichlet boundary condition with q = 0, g = (-nx·p, -ny·p, 0), h = (0, 0, 0; 0, 0, 0; 0, 0, 1), r = (0, 0, 300·mu/(rho·U·H)). For the group of 'Outlet', set Dirichlet boundary condition with q = 0, g = (-nx·p, -ny·p, 0), h = (0, 0, 0; 0, 0, 0; 0, 0, 1), r = (0, 0, 0). For the groups of 'Interior' and 'Symmetric', select Neumann boundary condition with default settings.

3) Nernst-Planck equation of K^+ and Cl^-

Add another PDE within coefficients form, named as NPKCl into the geometry, and its two dependent variables are set as CK and CCl. Its coefficients are given by

$$c = \begin{bmatrix} 1/(\mathrm{ReScK}) & 0 \\ 0 & 1/(\mathrm{ReScCl}) \end{bmatrix},\ a = e_a = \begin{bmatrix} 0 & 0 \\ 0 & 0 \end{bmatrix},\ d_a = \begin{bmatrix} 1 & 0 \\ 0 & 1 \end{bmatrix},\ f = \begin{bmatrix} 0 \\ 0 \end{bmatrix}$$

$$\alpha = \begin{bmatrix} (\mathrm{EMKx}, \mathrm{EMKy}) & (0,0) \\ (0,0) & (\mathrm{EMClx}, \mathrm{EMCly}) \end{bmatrix},\ \beta = \begin{bmatrix} (u, v) & (0,0) \\ (0,0) & (u, v) \end{bmatrix},\ \gamma = \begin{bmatrix} 0 & 0 \\ 0 & 0 \end{bmatrix}.$$

All parameters in 'Init' are imposed as 1.

Next, select Neumann boundary condition with default settings for the groups of 'Reservoir walls', 'Channel wall', and 'Symmetric', representing no-penetration condition at these planes. For the groups of 'Inlet' and 'Outlet', set Dirichlet boundary conditions with q = 0, g = (0, 0), h = (1, 0; 0, 1), and r = (1 ; 1) to fix the concentrations of K^+ and Cl^- at these planes. It is no need to manually set the boundary conditions for 'Interior'. Click 'Boundaries' in the window of 'Boundary settings', select plane 9, and mark 'Select by group' and 'Interior boundaries' to automatically set interior boundaries by COMSOL.

4) Nernst-Planck equation of H^+

Add the final PDE with coefficients form, named as NPH, into the geometry, and the coefficients are given by $c = \begin{bmatrix} \mathrm{Fdiff}/(\mathrm{ReScH}) & 0 \\ 0 & \mathrm{Fdiff}/(\mathrm{ReScH}) \end{bmatrix}$, $a = e_a = f = 0$, da =

Ftime, α = (EMHx, EMHy), β = (Ftime, Ftime), γ = (0,0). All initial values are set as 1.

The setting of most boundary conditions for H^+ are the same to those for K^+. The only difference is the setting for 'Channel wall' which uses Neumann boundary condition with q = 0; g = (u·nx + v·ny) ·CH - proton_exchange.

A.2.3 Solver Settings

Finally, the parameters used by the solver were set. Click 'Solver/Solver parameters' to open the window of 'Solver parameters'. Check whether the solver uses 'Time dependent', if not, highlight 'Time dependent'. The computation was performed in the ranges of $t^* < 1000$ and $t^* \geq 1000$ separately.

In the page of 'General', input 'range(0, 0.1, 1); range(11, 1, 20); range(25, 5, 100); range(200, 100, 1000)' for 'Times' when the simulation results will be stored for data analysis. In the page of 'Time Stepping', use the default time stepping method of 'BDF', change 'Time steps taken by solver' to 'Strict', and then click 'Manual tuning of nonlinear solver' to set 'Maximum time step' by '0.05'. Click 'Apply' to complete the settings of the solver for solving the problem within $t^* < 1000$.

Once the computation for $t^* < 1000$ is completed, change the setting of 'Times' to 'range(1500; 500; 35000)', and 'Maximum time step' to '3'.

A.3 Computation

The physics setting above were used to solve the transient problem which starts from an initial static state. In order to obtain the EDL structure at electrostatic equilibrium, the stationary problem was solved. Change the solver to 'Stationary'. And then select

'Solve/Solver Manager' to open up a window of 'Solver Manager'. In the page of 'Initial Value', click on 'Initial value expression' for 'Initial value' and 'Zero' for 'Values of variables not solved for and linearization point'. In the page of 'Solve For', highlight all models except 'PDE, Coefficient Form(Momentum)' so that only the Poisson equation and the Nernst equations are solved. Click 'Apply' to apply the changes. Click 'Solve' to start the computation.

After the computation solving for the EDL at electrostatic state, change the solver back to 'Time dependent', and select 'Solve/Solver Manager' again. In the page of 'Initial Value', click on 'Current solution' for 'Initial value' and for 'Values of variables not solved for and linearization point', or click 'Store Solution' to save the results and click on 'Stored solution' for both items. In the page of 'Solve For', highlight all models. Click 'Apply' and then 'Solve' to start the computation for the transient problem.

VITA

Zhuorui Song

Education

May 2015	**PhD, Mechanical Engineering,** Utah State Univ., Logan, UT
May 2007	**MS, Mechanical Engineering,** Univ. of Alabama at Birmingham, Birmingham, AL
Jul 2003	**MS, Thermal Engineering,** South China Univ. of Tech., China
Jul 1998	**BS, HVAC Engineering**, Hunan Univ., China

Professional Experience

May 2007–Present **Research Assistant,** Utah State Univ., Logan, UT

- Theoretical study of fluid transport in a nanochannel, which is governed by various physical mechanisms including flow dynamics, ionic transport, and electrical equilibrium.
- Theoretical and experimental studies of Electromagnetically-driven oscillating cup viscometer which is a newly-developed device used to measure electrical conductance and viscosity of high temperature fluids

Sept 2004–May 2007 **Research Assistant,** Univ. of Alabama at Birmingham, Birmingham, AL

- Experimental study of fluid flow through a micropipette

Jul 2003–Jul 2004 **Project Manager,** GMETC, Guangzhou, China

- Organized the purchase activities for mechanical equipments via tendering and bidding
- Completed purchases amounted to 10 million US dollars

Jul 1998–Sept 2000 **Mechanical Engineer,** Wuyang-Honda Motor, Guangzhou, China

- In charge of daily maintenance of an HVAC system for a 2000-person factory

Awards

Vice President for Research Fellowship of USU for 2008-2009

Professional Organizations

American Society of Mechanical Engineers (ASME)

Publications

[1] Ban, H., Lin, B. and Song, Z., 2010, "Effect of Electrical Double Layer on Electric Conductivity and Pressure Drop in a Pressure-Driven Microchannel Flow," Biomicrofluidics, 4, 014104

[2] Song Z., and Ban H., "Effects of Surface-Dissociated Hydronium Ions on Electrokinetic Flow in Nanofluidic Silica Channels." Targeted journal - Langmuir

[3] Song Z., and Ban H., "Transient Electrokinetic Flow in a Nanofluidic Silica Nanochannel." Targeted journal - Langmuir

[4] Song Z., and Ban H., " Theoretical Study of Electromagnetically-Driven Oscillating Cup Viscometer." Targeted journal - Physics of Liquids

Conference Presentations and Abstracts

[1] Song Z., and Ban H., 2009, "Electrical Double Layer in Nano-Flows", Proceedings of the Inaugural US-EU-China Thermophysics Conference, 0431.

[2] Song Z., and Ban H., 2008, "Capillary Flow with Overlapping Electrical Double Layer", Proceedings of the International Mechanical Engineering Congress and Exhibition, 68272.

[3] Song Z., Lin B., Ban H. and Liu S., 2006, "Experimental Study of Flow in Micropipette", Proceedings of the ASME International Mechanical Engineering Congress & Exposition, pp. 150041-8